**Time-frequency sonar detection of elastic wave reradiation**

by

Matthew Thompson

A dissertation submitted to the Graduate Faculty of
Auburn University
in partial fulfillment of the
requirements for the Degree of
Doctor of Philosophy

Auburn, Alabama
December 9, 2023

Keywords: signal processing, time-frequency, sonar, elastic wave



Approved by

Lloyd Riggs, Chair, Professor Emeritus of Electrical and Computer Engineering
Myoung An, Associate Research Professor of Computer Science and Software Engineering
Stanley Reeves, Professor Emeritus of Electrical and Computer Engineering
Thaddeus Roppel, Associate Professor Emeritus of Electrical and Computer Engineering
Bertram Zinner, Associate Professor Emeritus of Mathematics and Statistics

Abstract

This work examines the effectiveness of quadratic time-frequency methods in exposing the presence of elastic wave reradiation in active sonar returns. Elastic wave reradiation here means the coupling of elastic surface waves from an object under sonar interrogation into the surrounding water, where it is recorded in the sonar return—reradiation, because the original excitation generating the elastic surface waves is assumed to be the active sonar transmission. A brief survey of quadratic time-frequency representations and their underlying theory is provided, and a novel representation is proposed. The suitability and performance of the novel and existing representations are analyzed and compared in view of this application. The analysis is supported by simulation and by processing of data collected in a sonar experiment. In this experiment, air-filled cylinders of steel, aluminum, and PVC with similar geometries were interrogated in a controlled acoustic tank by a series of sonar waveforms which together span 5 kHz to 150 kHz in frequency at a variety of incident angles. A summary of current acoustic literature guides the simulation design and informs conclusions. The accumulation of evidence and observations identifies two distributions with strong advantages in relation to the elastic wave reradiation application: the Born-Jordan and the proposed distributions. These demonstrably facilitate acoustic discrimination based on elastic surface waves.

Acknowledgments

First, I would like to thank the Naval Undersea Warfare Center (NUWC) in Newport, Rhode Island for the use of acoustic data collected at its Acoustics Test Facility (ATF) in 2012.

Many thanks are due to my committee, Dr. Riggs, Dr. An, Dr. Reeves, Dr. Roppel, and Dr. Zinner, for valuable feedback, instruction, and guidance. Thanks also to Dr. Scott Martin for serving in the role of University Reader. In particular, I wish to recognize the contribution of Dr. Riggs, his good advice and patience in helping me see this work through to completion. I especially want to thank Dr. An for the joy of working on fascinating problems and for expanding my appreciation of mathematics. She has been integral in ensuring support for my studies and in passing on a great deal of valuable engineering and mathematical knowledge over the years.

I offer thanks to my lifelong friend, Gage Plott, for challenging and enlightening discussions of my derivations and subject matter.

I would not be writing these words without the support of my wonderful parents, who have instilled in me a pursuit of excellence in all I do and who have played a primary role in my education.

Finally, my deepest appreciation is owed to my extraordinary wife, Rebekah, whose love and unfailing encouragement have truly brought this effort to fruition.

Table of Contents

List of Figures

List of Tables

# Chapter 1

# Introduction

The purpose of this study is to identify effective time-frequency (TF) signal processing approaches for the active sonar-based detection of elastic surface wave reradiation. Discrimination strategies are important in any detection and classification scheme, and man-made objects of interest present to active sonar this underutilized discriminator as a result of their geometries and material compositions. Recent papers, largely from *The Journal of the Acoustical Society of America*, study the radiation of elastic waves from the surfaces of canonically-shaped shells—spheres and cylinders [1, 4, 5, 12, 13, 15, 17–19, 21–23, 25–29, 31–33, 37, 39, 40, 43]. A variety of physical experiments (though not at practical sonar scale) and simulations are contained in this collection of papers, and the consensus is that acoustic returns resulting from these elastic surface waves are distinguishable from the specular, or direct path, echo from active sonar. The elastic response is delayed from the specular return in time and is generally altered in its spectral composition compared to the specular return.

While there has been much research on the physical acoustics of elastic waves, there has been little systematic examination of the methods by which these phenomena may be quantified and leveraged. In light of the informational interest in both the time and frequency domains, time-frequency representations are useful in the isolation and identification of these elastic responses. Several different time-frequency methods are used in the acoustic literature on elastic waves, but often there is little rationale provided for the one chosen. In time-frequency analysis, the choice of method should depend on the nature of the signal in question. This work informs that decision, with an eye

toward practical application in sonar problems—both military and civilian. Naval applications include anti-submarine warfare and mine-countermeasure, but commercial and humanitarian possibilities abound. Both simulated and in-water test data is examined to provide a foundation for conclusions. This dissertation contributes a theoretical and practical evaluation of various time-frequency methods (both existing and original) for the purpose of elastic response identification, with special consideration given for future automated classification.

Simplifying assumptions are made:

1. Acoustic behavior is linear.

2. Observations are in the far field.

3. Only underwater acoustics is considered.

# Chapter 2

## Matched filter and deconvolution

One important methodological choice concerns the application of pulse compression before any time-frequency method is applied.

### 2.1 Matched filter

Traditional sonar processing involves matched filtering to concentrate the echo energy in the return for detection and classification. A matched filter is so-called since in signal detection problems like sonar, the transmitted waveform serves as an optimal template for exposing time-delayed versions of itself in a noisy signal, while maximizing the signal-to-noise ratio (SNR) . To calculate the matched filter, it is necessary simply to convolve a recorded signal $y(t)$ with the time-reversed complex conjugate of the transmitted waveform $x(t)$:

$$\mathrm{MF}_x[y(t)] = \int_{-\infty}^{\infty} y(t-\tau)\,\overline{x(-\tau)}d\tau. \tag{2.1}$$

Two important points should be made concerning the observability of elastic wave reradiation (EWR) after matched-filter processing. First, the matched filter significantly compresses typical sonar signals in time, a useful property since the reradiated waves can follow closely on the heels of the specular return and thus need to be resolved in time. Second, the spectral characteristics of the elastic wave reradiation are not spoiled by the filtering operation. Assume that the returning signal $y(t)$ is modeled as a convolution between a transmitted waveform $x(t)$ and a target response $h(t)$. By the convolution theorem $Y(\omega) = X(\omega)H(\omega)$, where $H(\omega)$ contains the spectral information of interest.

The matched filter adds a convolution to the equation:

$$\mathrm{MF}_x\left[y\left(t\right)\right] = y\left(t\right) * \overline{x\left(-t\right)} = \left[x\left(t\right) * h\left(t\right)\right] * \overline{x\left(-t\right)}, \tag{2.2}$$

which in the frequency domain becomes

$$\mathcal{F}\{\mathrm{MF}_x\left[y\left(t\right)\right]\} = X\left(\omega\right)\overline{X\left(\omega\right)}H\left(\omega\right) = \left|X\left(\omega\right)\right|^2 H\left(\omega\right), \tag{2.3}$$

since $x\left(-t\right) \leftrightarrow X\left(-\omega\right)$ and since $\overline{x\left(t\right)} \leftrightarrow \overline{X\left(-\omega\right)}$. This demonstrates that the spectral information of the target response remains after the process of matched filtering, meaning one can do time-frequency analysis just as well on the matched-filtered signal, taking advantage of the pulse compression, as on the target response convolution.

## 2.2 Deconvolution

Deconvolution is another approach to pulse compression and sonar scene estimation which attempts directly to undo the model of convolution between the transmitted waveform and the scene. In the ideal, no-noise situation, deconvolving the transmitted signal from the return perfectly resolves each reflector in the scene down to a delta function, assuming the scene is treated as a collection of point reflectors. In the presence of noise, the perfect reproduction of the scene is not possible, and the process will amplify noise, especially outside the bandwidth of the transmitted signal. This is due to the fact that undoing the convolution of the sonar scene and the transmitted signal involves dividing the spectrum of the recorded return by that of the transmitted signal. Thus, any region of the transmitted spectrum which is at or near zero-amplitude will result in disproportionate weight being given to the scene response estimate when noise is present in that region.

One method suitable for sonar is Wiener deconvolution, which seeks to counteract this noise amplification by scaling the deconvolution divisor by the signal-to-noise ratio

$\mathrm{SNR}(\omega)$ (or an estimate thereof). The Wiener filter equation takes the form

$$G(\omega) = \frac{1}{X(\omega)} \left[ \frac{1}{1 + \frac{1}{|X(\omega)|^2 \mathrm{SNR}(\omega)}} \right], \tag{2.4}$$

where $X(\omega)$ represents the Fourier transform of the transmitted waveform. It is assumed to be convolved with the time series representing the scene and so will be deconvolved to estimate the scene. Since $\mathrm{SNR}(\omega)$ is a function of $\omega$, it is possible to avoid noise amplification in portions of the sampled spectrum that are outside the support of $X(\omega)$. In this application SNR will be given by

$$\mathrm{SNR}(\omega) = \frac{|X(\omega)|^2}{\alpha}, \tag{2.5}$$

yielding

$$G(\omega) = \frac{\overline{X(\omega)}}{|X(\omega)|^2 + \frac{\alpha}{|X(\omega)|^2}}. \tag{2.6}$$

## 2.3 Comparison and conclusions

Since the SNR term in the Wiener deconvolution is adjustable, it is possible to tailor the effect of the operation to the data at hand. The span of this adjustment is considerable, allowing at one extreme identical performance to that of the matched filter, and at the other the simple deconvolution which makes no attempt to prevent noise amplification at all. Figures 2.1 through 2.4 provide a visual comparison of the matched filter and the deconvolution for a linear frequency-modulated (LFM) chirp in the presence of noise. This chirp has a pulse period $T = 1\,\mathrm{s}$, a bandwidth of 40 Hz, a center frequency of 50 Hz, and is sampled at a rate of 200 Hz. Complex noise is added with a normal distribution and a variance of 0.3.

Since the matched filter is designed for the express purpose of maximizing the signal-to-noise ratio, the reliance upon that method for the purpose of measuring sonar elastic wave reradiation will be advisable to the degree that SNR is of primary concern. It

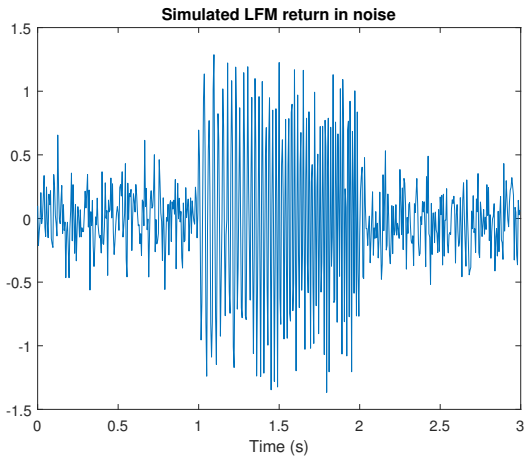


Figure 2.1: Real part of LFM echo in the presence of noise

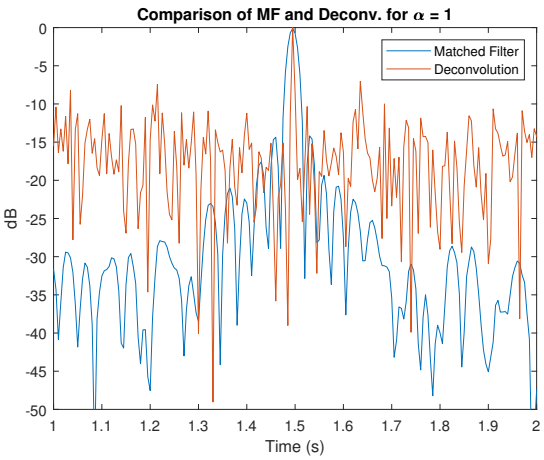


Figure 2.2: Comparison of matched filter and deconvolution for $\alpha = 1$

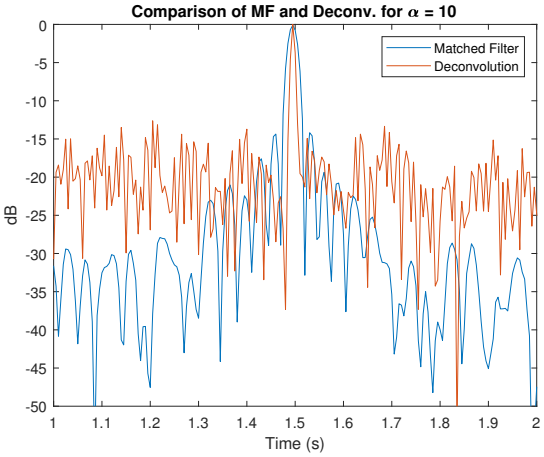


Figure 2.3: Comparison of matched filter and deconvolution for $\alpha = 10$

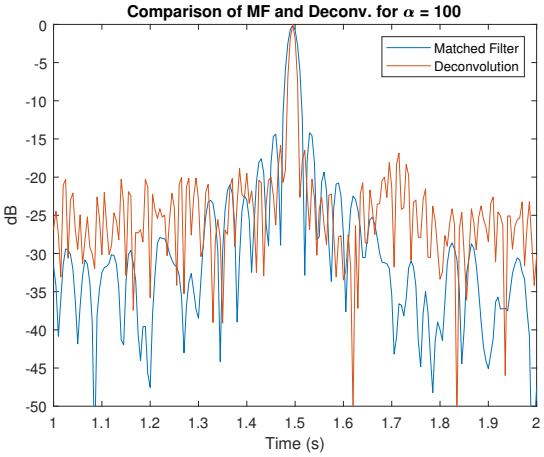


Figure 2.4: Comparison of matched filter and deconvolution for $\alpha = 100$

happens, however, that (at least for the data from the controlled tank environment considered in this study) SNR is not a chief barrier in the success of the processing. Rather it is the ability to differentiate portions of the sonar return into components associated with the physical theory of underwater acoustic interactions. The main dimension along which this separation is achieved is that of time, since it is a central assumption that the specular return arrives first at the sonar receiver and elastic surface wave reradiations are subsequent. Depending on the transmitted waveform and the size and structure of the ensonified object, the time separation between these acoustic components may be quite brief, creating a concern about sidelobe contamination between components. It is for this

reason that the deconvolution begins to demonstrate its attractiveness—providing the capacity to control the sidelobe levels and main lobe width and thus reducing ambiguity in closely-spaced signals. Additionally, there is the simple flexibility afforded by the deconvolution filter, permitting by tuning the achievement of a proper balance between the interests of SNR and of sidelobe levels. Note that the deconvolution becomes increasingly like the matched filter when $\alpha$ becomes large, as in Figure 2.4. The above considerations lead this investigation to use primarily the deconvolution to analyze elastic wave reradiation, and the tank-collected data in view contains very little noise, allowing for a small $\alpha$.

# Chapter 3

## Time-frequency methods

Time-frequency methods are preferable when faced with identifying elastic wave reradiation in active sonar because the information of interest varies simultaneously across frequency and time. Additionally, the two-dimensional nature of these methods provides a couple of advantages. The desired phenomena may be more easily recognized in an image, and the many tools of image processing would be available for quantifying subtle information and eventually for automated classification algorithms.

One way to frame the question at hand is: how does the frequency content of this signal vary over time? Before confronting the practical aspects of this, it is worthwhile to consider the fundamentals of this question, as it hides some assumptions. In common understanding, frequency refers to the periodic repetition of a particular event. In Fourier analysis, an additional mathematical stricture is applied such that a pure signal of a single frequency is infinite in duration. Using the Fourier transform to examine a signal in the frequency domain involves an infinite integral or summation. Practical signals are not infinite, however, so assumptions must be made in Fourier analysis. In the example of a known mono-component yet finite sinusoid, the question is asked: what is the frequency? Strictly speaking, the signal, since finite, cannot be comprised of a single frequency, but the question has practical significance as the mono-component nature is known *a priori*, and one could suggest that what is actually referred to in the query is extrapolation of a finite cyclic event into infinity.

There is a very similar point to be made concerning the seemingly paradoxical concept of instantaneous frequency, which is connected to a basic question in time-frequency

analysis: What is the frequency of this signal at a particular moment in time? This magnifies the assumption in the previous question. When one reduces the finitude to an infinitesimal, there is a fair concern to be raised about whether the question even makes sense. Can frequency be defined in the absence of duration?

It seems the answer to this question is yes, provided certain conceptual *a priori* information. Consider frequency-sweeping waveforms and in particular the linear chirp. If $x\left(t\right)$ is a linear chirp, it takes the form:

$$x\left(t\right) = a\left(t\right) e^{j2\pi\phi(t)} = a\left(t\right) e^{j\pi\left(\frac{f_e - f_s}{T}\right)t^2 + j2\pi f_s t}, \tag{3.1}$$

where $a(t)$ is the amplitude, typically a window function of width $T$; $f_s$ and $f_e$ are the starting and ending frequencies, respectively; and $T$ is the duration of the chirp. Taking the derivative of the phase term $\phi\left(t\right)$ yields:

$$\frac{d\phi\left(t\right)}{dt} = \left(\frac{f_e - f_s}{T}\right) t + f_s. \tag{3.2}$$

This is commonly referred to as the instantaneous frequency of the chirp, and intuitively so. The linear chirp is conceived with a constant linear frequency shift in mind, and indeed the rate of change of the phase takes on the form of a linear equation. Evaluating $\frac{d\phi(t)}{dt}$ at a given time $t$ provides the instantaneous frequency at $t$. This calculation, however, since it derives from the definition of the linear chirp, is dependent on that prior knowledge. One could work backward from a measured signal to estimate the instantaneous frequency at a moment in time, but it would require assumptions about the nature of the signal—such as there being a single frequency component and there being an identifiable frequency sweep pattern and rate. If a signal is composed of multiple simultaneous frequencies, for instance, could an instantaneous frequency be measured? Depending on the application, it is likely that the most meaningful approach would be to isolate the multiple component sinusoids or chirps and determine the corresponding instantaneous frequency for each.

In other words, because of the assumptions inherent in the concept of instantaneous frequency, one must use application-specific knowledge which can inform the time-frequency approach and best answer the relevant questions. Signals convey information, to be sure, but the importance of the conceptual frameworks which undergird the understanding of the signals cannot be underestimated. Following is an overview of the time-frequency methods to be considered in this dissertation to demonstrate their variety and the importance of choosing the appropriate method for the given signal processing problem. It should be noted that, because of the practical nature of this dissertation, digital (or discrete) signals will be primarily considered.

## 3.1 Short-time Fourier transform

The short-time Fourier transform (STFT) is perhaps the most intuitive because it requires only the discrete Fourier transform (DFT) and a sliding window function. The idea is simply to divide a signal into small durations and calculate a DFT on each of them, thus providing the change in the spectrum over time. It can be tuned by varying the window size, window shape, and successive window overlap. A continuous-time representation of the STFT is

$$\mathcal{F}_s^w(t,f) = \int_{-\infty}^{\infty} z(\tau)\, w(\tau - t)\, e^{-j2\pi f\tau} d\tau, \tag{3.3}$$

where $z(\tau)$ is the complex signal and $w(\tau)$ is the window.

## 3.2 Time-frequency distributions

The following time-frequency distributions differ from the preceding representations in that they are quadratic (or bilinear) and suffer from cross-terms that appear as artifacts in the time-frequency image, or apparent components of the signal that are not really present. In this section, $z(t)$ represents a complex signal, $w(t)$ a window function, $\overline{z(t)}$ represents the complex conjugate of $z(t)$, and $\alpha$ and $\sigma$ are real and positive parameters.

These representations can be usefully characterized in four different domains, one of which would be called the time-frequency $(t, f)$ domain. The others are the time-lag $(t, \tau)$, the Doppler-frequency $(\nu, f)$, and the Doppler-lag $(\nu, \tau)$ domains. They are separated from each other by a Fourier transform along one or both of the axes. The Fourier transform along the lag $\tau$ axis yields frequency $f$, and the Fourier transform along the time $t$ axis yields Doppler $\nu$.

The basic form of the quadratic class of time frequency representations is:

$$\rho_z(t, f) = \underset{\tau \to f}{\mathcal{F}}\{R(t, \tau)\} = \underset{\tau \to f}{\mathcal{F}}\{G(t, \tau) \underset{t}{*} K_z(t, \tau)\}, \tag{3.4}$$

where $\rho_z(t, f)$ is the time-frequency distribution, $R(t, \tau)$ the smoothed instantaneous autocorrelation function, $G(t, \tau)$ the time-lag kernel, and $K_z(t, \tau)$ the instantaneous autocorrelation function. $K_z(t, \tau)$ is defined as

$$K_z(t, \tau) = z\left(t + \frac{\tau}{2}\right)\overline{z\left(t - \frac{\tau}{2}\right)}. \tag{3.5}$$

Each of the three elements of Eq. 3.4 ($R(t, \tau)$, $G(t, \tau)$, and $K_z(t, \tau)$) has its own representation in the four domains described above, and together they provide an illustration of the functionality of the quadratic class. $K_z(t, \tau)$, simply a function of the signal itself, becomes the Wigner-Ville distribution $W_z(t, f)$ in the time-frequency domain (after time-convolution with the Wigner-Ville time-lag kernel, $\delta(t)$), the symmetrical ambiguity function $A_z(\nu, \tau)$ in the Doppler-lag domain, and the spectral autocorrelation function $k_z(\nu, f)$ in the Doppler-frequency domain.

Figures depicting an example signal for a visual comparison of the various time-frequency methods will be included here and in the following subsections. (The signals proposed for analysis in later chapters are much more complex, but this example will serve for a simple demonstration.) The example signal consists of two frequency-modulated chirps, one linear and one hyperbolic, of equal duration, overlapping but offset in time. Each chirp spans the frequency range $50\,\text{Hz} - 250\,\text{Hz}$, and the signal is sampled at $600\,\text{Hz}$.

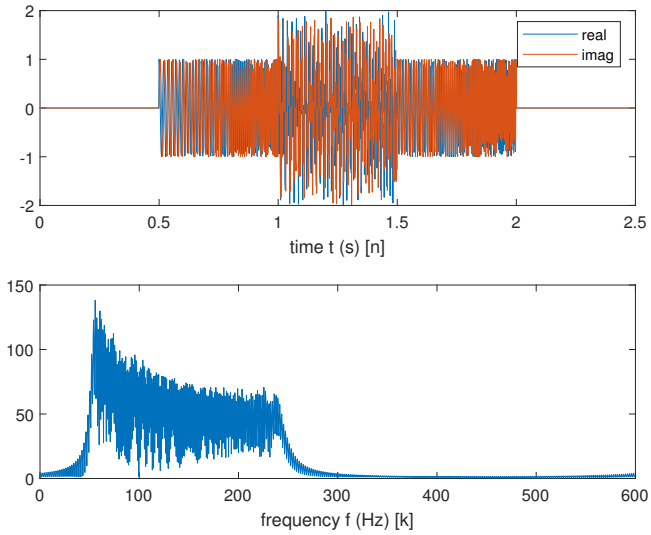


Figure 3.1: Time domain (top) and frequency domain (bottom) plots of example signal

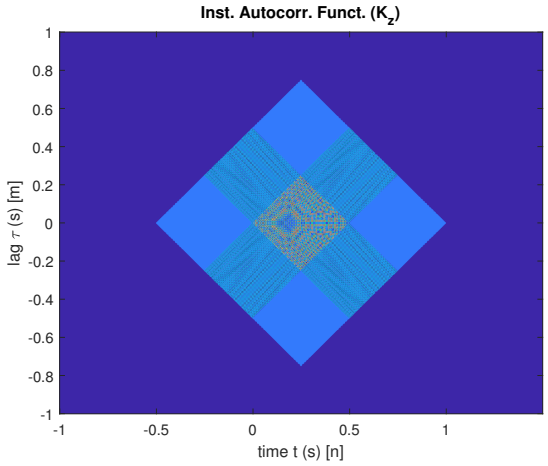


Figure 3.2: Instantaneous autocorrelation function of example signal

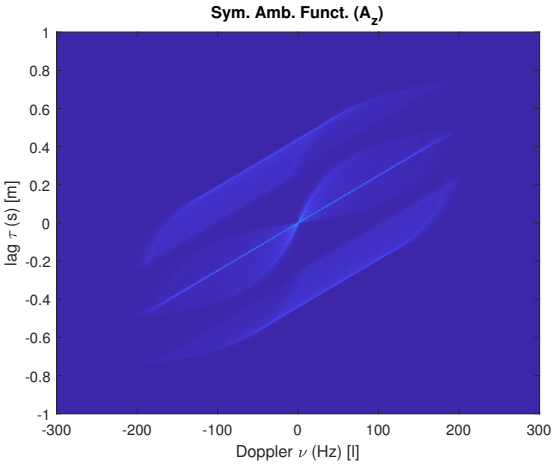


Figure 3.3: Symmetrical ambiguity function of example signal

Refer to Figure 3.1 for the time-series and frequency domain representations of this example signal. These representations demonstrate the need for the time-frequency approaches in question, as the nature of the signal is not easily discerned in either the time or in the frequency domain. For distributions making use of a windowing function, a Hann window with a duration of 0.1 s (or 60 samples) has been applied.

For the described signal $K_z(t, \tau)$, $A_z(\nu, \tau)$, and $k_z(\nu, f)$ are shown in Figures 3.2, 3.3, and 3.4, respectively.

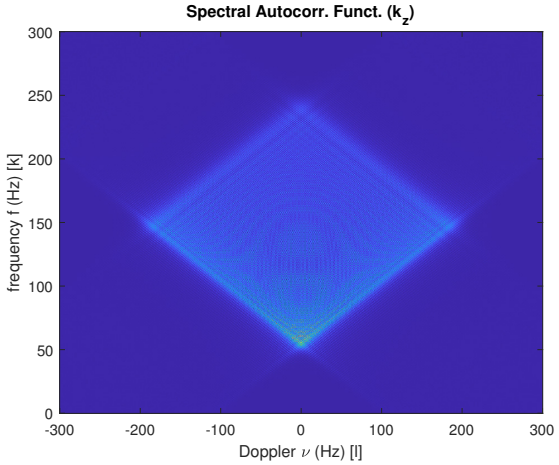


Figure 3.4: Spectral autocorrelation function of example signal

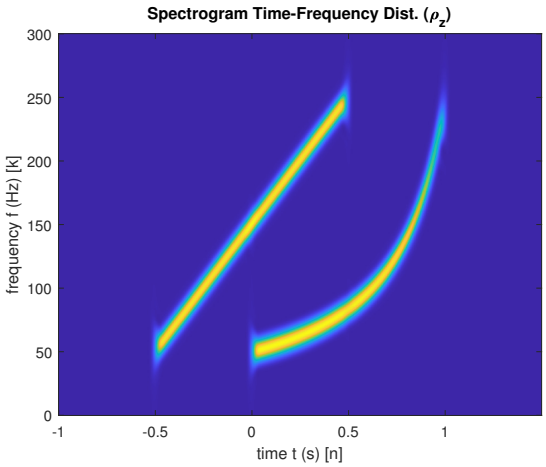


Figure 3.5: Spectrogram of example signal

### 3.2.1 Spectrogram

The Spectrogram is simply the squared magnitude of the short-time Fourier transform,

$$\rho_z(t,f) = \left| \int_{-\infty}^{\infty} z(\tau)\, w(\tau - t)\, e^{-j2\pi f\tau} d\tau \right|^2, \tag{3.6}$$

but is in fact also a quadratic time-frequency distribution with the time-lag kernel $G(t,\tau) = w\left(t+\frac{\tau}{2}\right) w\left(t-\frac{\tau}{2}\right)$. It functions very similarly to the STFT and without the drawback of cross terms. The disadvantage is the fact that the resolution is much reduced compared with other options like, say, the Wigner-Ville distribution. Figure 3.5 shows how well the spectrogram performs on the above example signal using a window size of 0.1 s; the two frequency-modulated components are clearly visible.

### 3.2.2 Wigner-Ville distribution

The Wigner-Ville distribution of a signal can be found using

$$\rho_z(t,f) = \int_{-\infty}^{\infty} z\left(t+\frac{\tau}{2}\right) \overline{z\left(t-\frac{\tau}{2}\right)} e^{-j2\pi f\tau} d\tau. \tag{3.7}$$

Its time-lag kernel is merely $G(t,\tau) = \delta(t)$.

In 1932, Wigner [41] developed a distribution in his work on quantum mechanics. This was built upon by Ville [42] in 1948, who improved its usefulness in signal processing by incorporating the analytic signal, significantly reducing artifacts. Note in Figure 3.6 that because of its formulation, this distribution is optimal for linear frequency-modulated (LFM) chirps, resulting in a high-resolution image of the chirp in the time-frequency plane. For time-frequency components which do not have the structure of the linear chirp, considerable artifacts result, such as inside the arc of the hyperbolic chirp shown. When compared with the spectrogram (Figure 3.5), the cross term situated between the two chirp components is obvious. It is useful also to observe that the effect of the Wigner-Ville distribution on the linear chirp itself can be thought of as producing internal cross terms, it is just that this artifact lies along the line of the linear chirp component anyway, and so does not obscure interpretation of linear chirps.

### 3.2.3 Windowed Wigner-Ville distribution

If instead a window is applied to the time-lag kernel such that $G(t,\tau) = \delta(\tau)\, w(\tau)$, the resulting distribution is given by

$$\rho_z(t,f) = \int_{-\infty}^{\infty} w(\tau)\, z\left(t+\frac{\tau}{2}\right)\overline{z\left(t-\frac{\tau}{2}\right)} e^{-j2\pi f\tau} d\tau. \tag{3.8}$$

Time-limiting the Wigner-Ville distribution can help reduce cross-terms occurring along the time axis. This is known as the windowed or pseudo-Wigner-Ville distribution. In Figure 3.7 the sharp and defined edge of the linear chirp in Figure 3.6 is sacrificed to reduce cross-term interference; however, this is time-limiting, and only reduces that interference for components widely separated in time. When the linear chirp and the hyperbolic chirp overlap, cross-terms remain.

### 3.2.4 Rihaczek distribution

Rihaczek derived a complex energy density [36] which has become known as the Rihaczek distribution. It also takes the form of a quadratic time-frequency representation with time-lag kernel $G(t,\tau) = \delta\left(t-\frac{\tau}{2}\right)$ (Figure 3.8), resulting in an expression of the

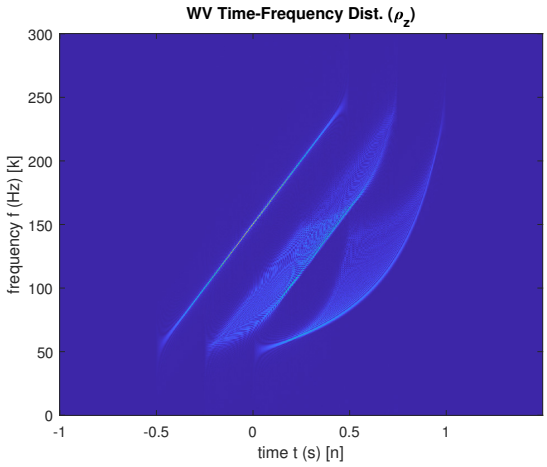


Figure 3.6: Wigner-Ville distribution of example signal

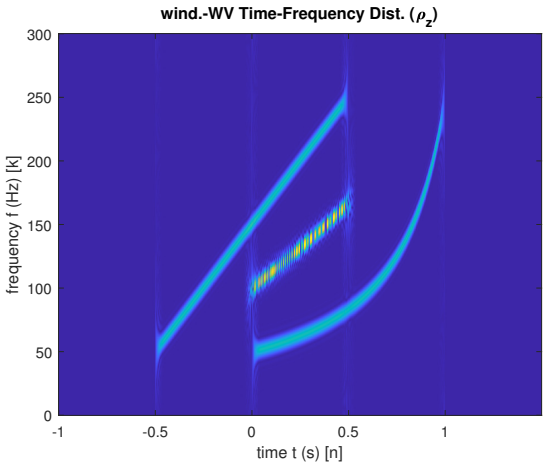


Figure 3.7: Windowed Wigner-Ville distribution of example signal

distribution

$$\rho_z(t,f) = \int_{-\infty}^{\infty} z(t)\,\overline{z(t-\tau)}e^{-j2\pi f\tau}d\tau. \tag{3.9}$$

Figure 3.9 shows how markedly differently the Rihaczek distribution performs on the example signal. Significant artifacts complicate the use of the distribution in many practical applications. The reason for this is that, while it may separate components well in time alone or in frequency alone, it has difficulty in separating in both dimensions at once. This makes the distribution suitable only for a narrow range of applications, but interestingly, distributions in this family (of which two more will be introduced in following subsections) are potentially useful for signals which have been pulse-compressed, such as sonar signals. This relevance will be discussed in later chapters.

### 3.2.5 Levin distribution

Taking only the real part of the Rihaczek distribution

$$\rho_z(t,f) = \mathrm{Re}\left[\int_{-\infty}^{\infty} z(t)\,\overline{z(t-\tau)}e^{-j2\pi f\tau}d\tau\right], \tag{3.10}$$

one is left with Levin distribution [24], which corresponds to a time-lag kernel of $G(t,\tau) = \frac{1}{2}\left[\delta\left(t+\frac{\tau}{2}\right)+\delta\left(t-\frac{\tau}{2}\right)\right]$ (Figure 3.10). Figure 3.11 is substantially the same as Figure 3.9, since one is obliged when representing the Rihaczek in a visually meaningful way

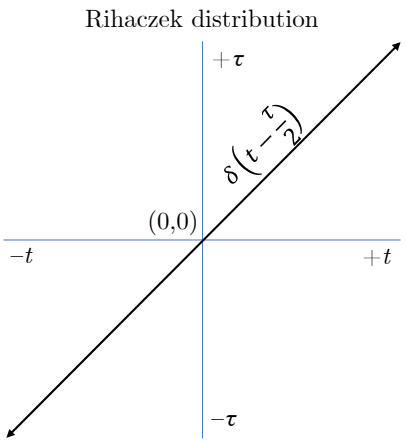


Figure 3.8: Graphical representation of the Rihaczek time-lag kernel

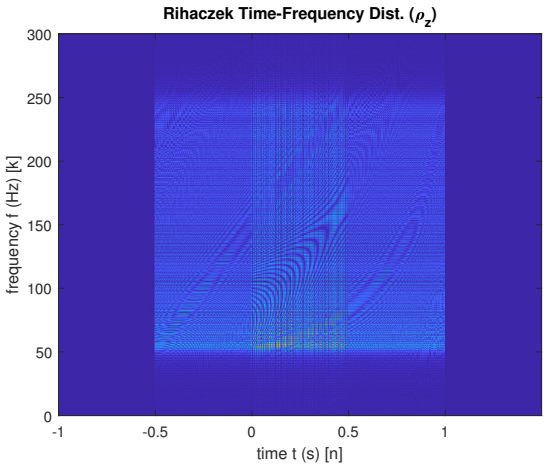


Figure 3.9: Magnitude of real part of Rihaczek distribution of example signal

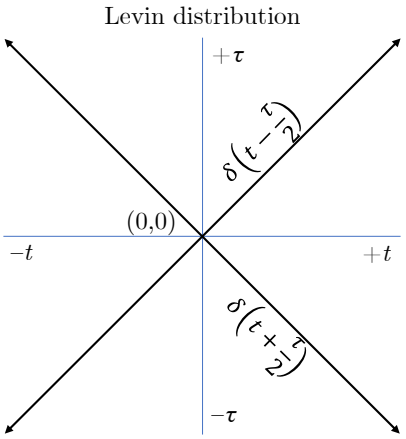


Figure 3.10: Graphical representation of the Levin time-lag kernel

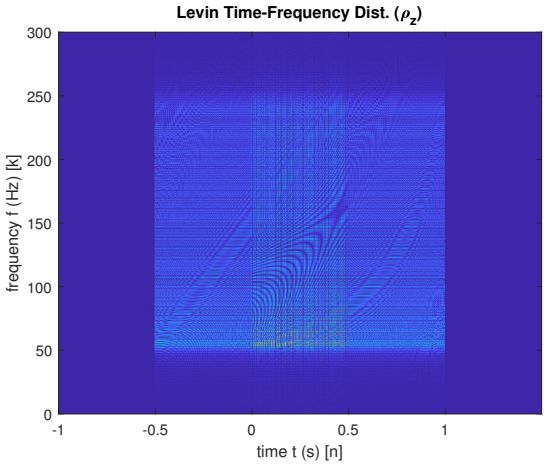


Figure 3.11: Levin distribution of example signal

to use only the real part, as the magnitude alone (how most plots in this chapter are produced) reveals little useful information about the nature of the components in the example signal.

### 3.2.6 Page distribution

The Page distribution is similar in kind to both the Rihaczek and the Levin, and historically was the first to be developed [34]. It can be expressed as

$$\rho_z(t,f) = 2\,\mathrm{Re}\left[\int_0^\infty \overline{z(t)}z(t-\tau)\,e^{j2\pi f\tau}d\tau\right], \tag{3.11}$$

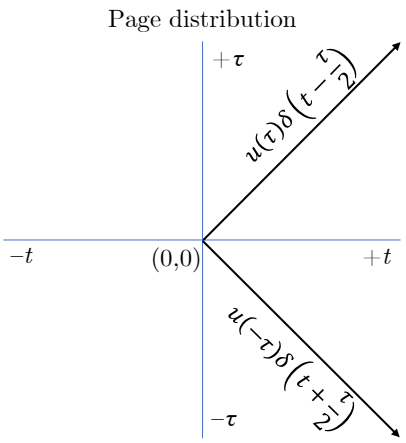


Figure 3.12: Graphical representation of the Page time-lag kernel

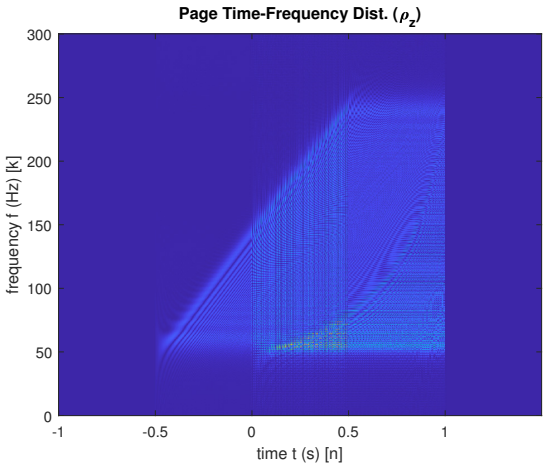


Figure 3.13: Page distribution of example signal

with its time-lag kernel being $G(t,\tau) = \delta\left(t + \left|\frac{\tau}{2}\right|\right)$ (Figure 3.12). Figure 3.13 shows the result of the Page distribution performed on the example signal; it is worth noticing that the one-sided kernel produces artifacts on only one side of distribution image.

### 3.2.7 Windowed Rihaczek, Levin, and Page distributions

Each of the Rihaczek, Levin, and Page distributions can be windowed to reduce the impact of the cross term artifacts and make them more immediately useful for general signals. Mathematically, these would be rendered thus:

1. Windowed Rihaczek distribution (Figure 3.14)

$$\rho_z(t,f) = \int_{-\infty}^{\infty} w(\tau)\, z(t)\, \overline{z(t-\tau)} e^{-j2\pi f\tau} d\tau \tag{3.12}$$

$$G(t,\tau) = w(\tau)\,\delta\left(t - \frac{\tau}{2}\right) \tag{3.13}$$

2. Windowed Levin distribution (Figure 3.15)

$$\rho_z(t,f) = \mathrm{Re}\left[\int_{-\infty}^{\infty} w(\tau)\, z(t)\, \overline{z(t-\tau)} e^{-j2\pi f\tau} d\tau\right] \tag{3.14}$$

$$G(t,\tau) = \frac{w(\tau)}{2}\left[\delta\left(t + \frac{\tau}{2}\right) + \delta\left(t - \frac{\tau}{2}\right)\right] \tag{3.15}$$

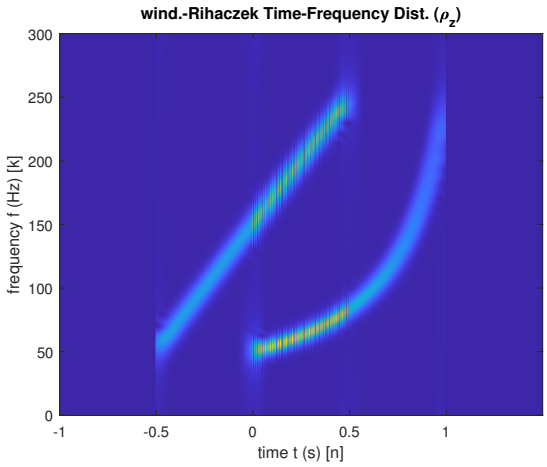


Figure 3.14: Windowed Rihaczek distribution of example signal

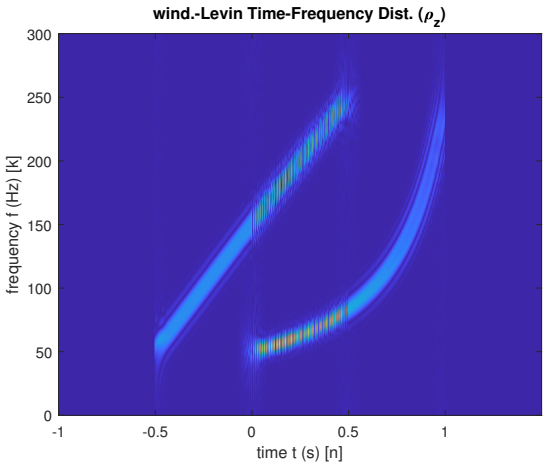


Figure 3.15: Windowed Levin distribution of example signal

3. Windowed Page distribution (Figure 3.16)

$$\rho_z(t,f) = 2\,\mathrm{Re}\left[\int_0^\infty w(\tau)\,\overline{z(t)}z(t-\tau)\,e^{j2\pi f\tau}d\tau\right] \tag{3.16}$$

$$G(t,\tau) = w(\tau)\,\delta\left(t+\left|\frac{\tau}{2}\right|\right) \tag{3.17}$$

### 3.2.8 B distribution

The B distribution is a newer distribution developed by Barkat and Boashash [3] with an aim toward high time-frequency resolution and cross term reduction. Its time-lag kernel $G(t,\tau) = |\tau|^\beta \cosh^{-2\beta} t$ is chosen for its narrow Doppler main lobe (Figure 3.17) to aid frequency resolution and is also nearly constant in the lag dimension, excepting a small notch at $\tau = 0$. This kernel is separable, meaning that it can be treated as two one-dimensional filters rather than one two-dimensional filter. This typically simplifies the kernel design process. The authors note that the positive real parameter $\beta$, which controls the amount of smoothing, is generally best chosen between 0 and 1, and they recommend in particular a $\beta$ of about 0.01. The distribution shown in Figure 3.18 (and the kernel in Figure 3.17) uses $\beta = 0.1$ since smaller values appeared to sacrifice too much in the way of resolution for this example signal. Noteworthy is the significant reduction in artifacts just inside the arc of the hyperbolic chirp as compared to the Wigner-Ville

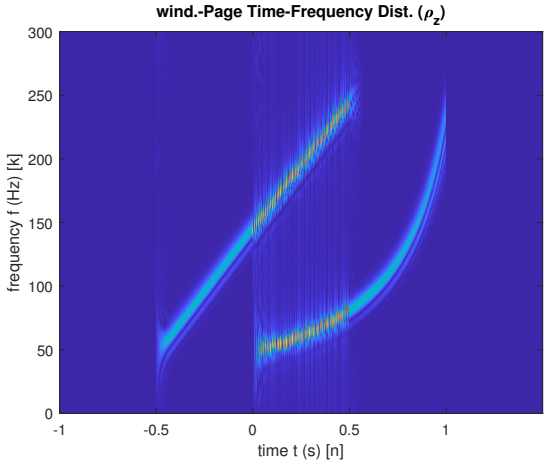


Figure 3.16: Windowed Page distribution of example signal

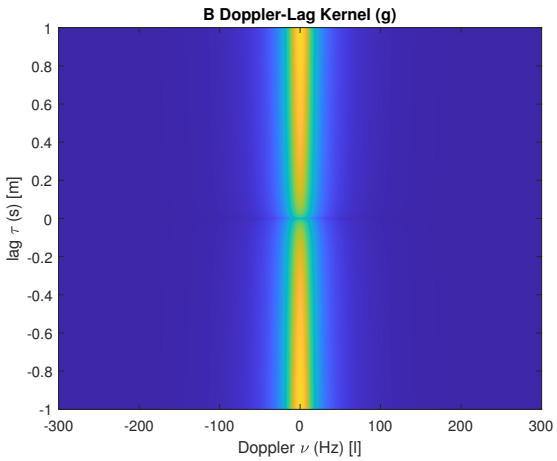


Figure 3.17: B distribution Doppler-lag kernel

distribution—while still retaining much of the achieved narrowness or resolution in the time-frequency peak. The kernel results in the following expression for the time-frequency distribution:

$$\rho_z(t,f) = \iint \frac{|\tau|^\beta}{\cosh^{2\beta}(t-u)} z\left(u+\frac{\tau}{2}\right)\overline{z\left(u-\frac{\tau}{2}\right)}e^{-j2\pi f\tau}du\ d\tau. \tag{3.18}$$

### 3.2.9 Modified-B distribution

The B distribution in the previous subsection was modified [20] to have a truly lag-independent kernel (meaning the kernel has no dependence on $\tau$), as it already was nearly so,

$$G(t,\tau) = \frac{\cosh^{-2\beta} t}{\int_{-\infty}^{\infty}\cosh^{-2\beta}(\xi)\,d\xi}. \tag{3.19}$$

Boashash notes this modified-B distribution has optimal energy concentrations around the components when the signal is a sum of tones. The example signal rendered with it (Figure 3.19), also with $\beta = 0.1$, is very similar to the original B distribution, again since the kernels are comparable. A full expression for the modified-B is

$$\rho_z(t,f) = \iint \frac{\cosh^{-2\beta}(t-u)}{\int_{-\infty}^{\infty}\cosh^{-2\beta}(\xi)\,d\xi} z\left(u+\frac{\tau}{2}\right)\overline{z\left(u-\frac{\tau}{2}\right)}e^{-j2\pi f\tau}du\ d\tau. \tag{3.20}$$

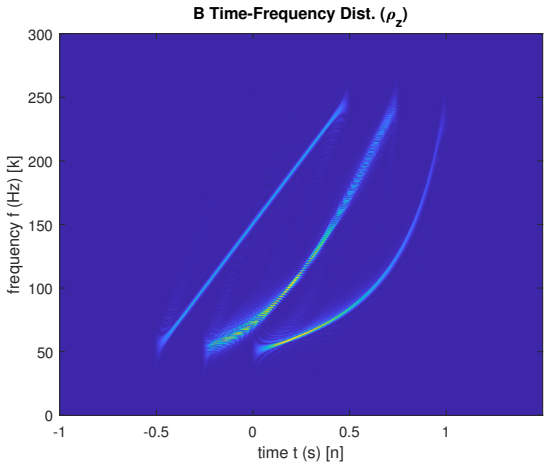


Figure 3.18: B distribution of example signal

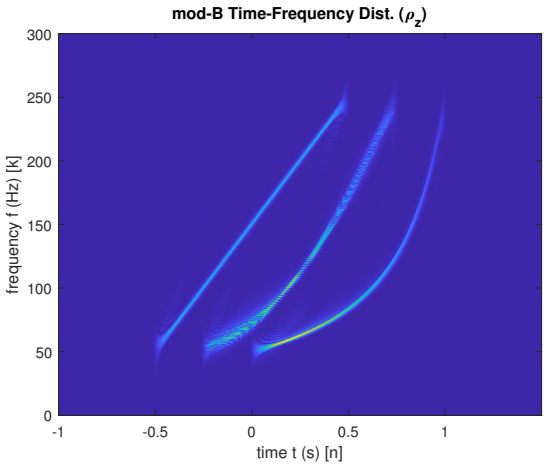


Figure 3.19: Modified-B distribution of example signal

### 3.2.10 Choi-Williams distribution

The Choi-Williams distribution [10] attempts to preserve the high time-frequency resolution of the Wigner-Ville distribution, while significantly reducing the amplitude of cross terms. The time-lag kernel is given as $G(t,\tau) = \frac{\sqrt{\pi\sigma}}{|\tau|} e^{\frac{-\pi^2\sigma t^2}{\tau^2}}$ (with Doppler-lag kernel shown in Figure 3.20 with $\sigma = 4$), yielding an overall expression for the distribution

$$\rho_z(t,f) = \iint \frac{\sqrt{\pi\sigma}}{|\tau|} e^{\frac{-\pi^2\sigma(t-u)^2}{\tau^2}} z\left(u+\frac{\tau}{2}\right)\overline{z\left(u-\frac{\tau}{2}\right)} e^{-j2\pi f\tau} du\, d\tau. \tag{3.21}$$

In Figure 3.21, the cross term artifacts between the two chirps can be seen less concentrated in the time-frequency plane than in the Wigner-Ville or B distributions.

### 3.2.11 Zhao-Atlas-Marks distribution

Zhao, Atlas, and Marks [44] proposed a distribution with the time-lag kernel $G(t,\tau) = w(\tau)\,\mathrm{rect}\left(\frac{at}{2\tau}\right)$ and general expression

$$\rho_z(t,f) = \int_{-\infty}^{\infty}\int_{t-\left|\frac{\tau}{a}\right|}^{t+\left|\frac{\tau}{a}\right|} w(\tau)\, z\left(u+\frac{\tau}{2}\right)\overline{z\left(u-\frac{\tau}{2}\right)} e^{-j2\pi f\tau} du\, d\tau. \tag{3.22}$$

Choosing $a = 8$, as in the Doppler-lag kernel of Figure 3.22 and distribution of Figure 3.23, the latter figure shows what trade-off may be achieved in comparison to earlier

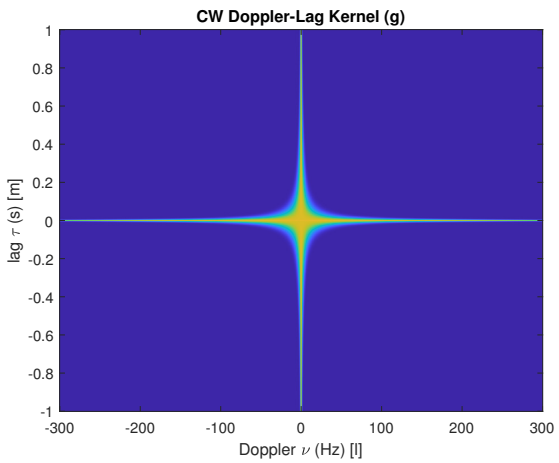


Figure 3.20: Choi-Williams distribution Doppler-lag kernel

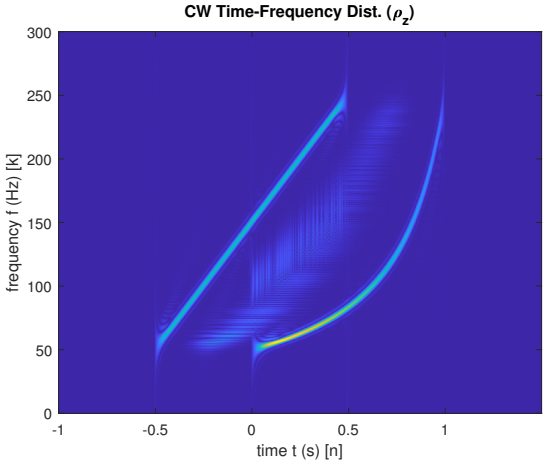


Figure 3.21: Choi-Williams distribution of example signal

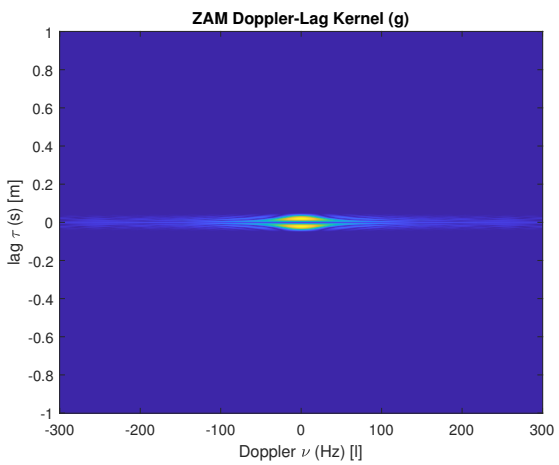


Figure 3.22: Zhao-Atlas-Marks distribution Doppler-lag kernel

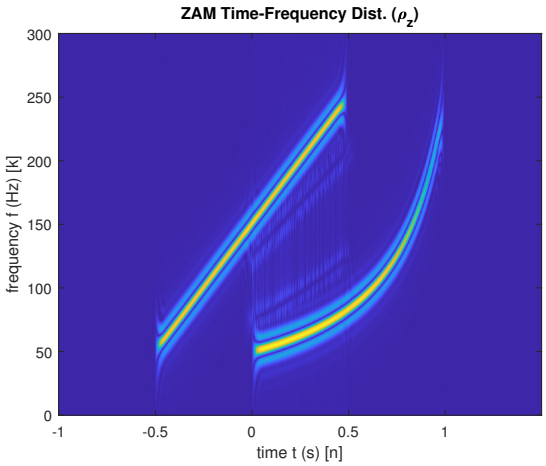


Figure 3.23: Zhao-Atlas-Marks distribution of example signal

distributions, namely that cross term effects can be somewhat exchanged for auto-terms, or artifacts one may say form within or around the real components themselves, rather than halfway between them. In this case, they appear as a kind of sidelobe or ringing about the two chirps.

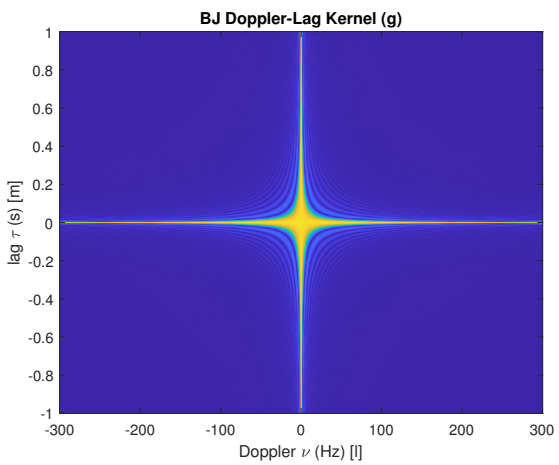


Figure 3.24: Born-Jordan distribution Doppler-lag kernel

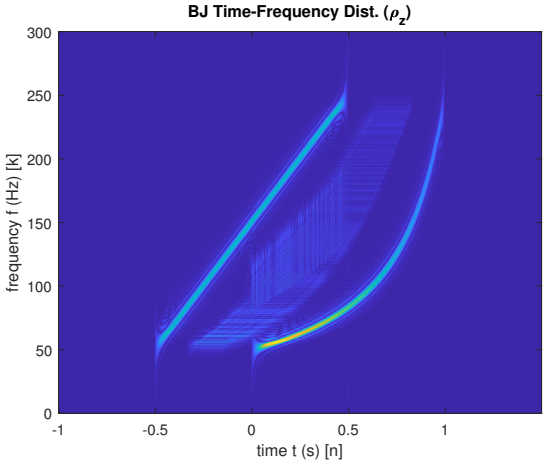


Figure 3.25: Born-Jordan distribution of example signal

### 3.2.12 Born-Jordan distribution

A special case of the Zhao-Atlas-Marks distribution above is the Born-Jordan distribution [8] when $a = \frac{1}{\alpha}$ and $w(\tau) = \frac{1}{|2\alpha\tau|}$. It can be expressed as

$$\rho_z(t,f) = \int_{-\infty}^{\infty} \int_{t-|\alpha\tau|}^{t+|\alpha\tau|} \frac{1}{2\alpha\tau} z\left(u + \frac{\tau}{2}\right) \overline{z\left(u - \frac{\tau}{2}\right)} e^{-j2\pi f\tau} du \; d\tau, \tag{3.23}$$

with a time-lag kernel of $G(t,\tau) = \frac{1}{|2\alpha\tau| \operatorname{rect}\left(\frac{t}{2\alpha\tau}\right)}$. The Doppler-lag kernel, very similar to that of the Choi-Williams distribution with the choice of $\alpha = 0.1$, is shown in Figure 3.24 along with its resulting performance on the previous example function in Figure 3.25.

# Chapter 4

# A proposed time-frequency distribution

A quadratic time-frequency distribution is here proposed which is in much the same vein as the Levin, Rihaczek, and Page distributions. While the Page distribution makes use of a running transform of a signal $s$ up to time $t$ [6], a new approach is considered here that uses instead a transform that runs from time $t$ onward. The relevance is that such a method allows better separation of cross-terms from the information in the time-frequency plane which is important for elastic wave reradiation. It also retains the good performance on pulse-compressed signals—those having wide-band content in a short time duration—as will be seen. It is informative to follow the derivation model of the Page distribution from Boashash [6] but with the necessary changes to arrive at a new distribution.

## 4.1 Derivation

While the Page distribution begins with the left (or negative) side of a Fourier transform of $s$,

$$S_{-}(t,f) = \underset{\theta \to f}{\mathcal{F}}\{s_{t-}(\theta)\} = \int_{-\infty}^{t} s(\theta)\, e^{-j2\pi f\theta} d\theta, \tag{4.1}$$

here instead the corresponding right (or positive) side running onward from $t$ will be defined,

$$S_{+}(t,f) = \underset{\theta \to f}{\mathcal{F}}\{s_{t+}(\theta)\} = \int_{t}^{\infty} s(\theta)\, e^{-j2\pi f\theta} d\theta. \tag{4.2}$$

Also to be defined is a running energy spectrum, which is the squared magnitude of $S_+$:

$$e_s(t,f) = |S_+(t,f)|^2 = S_+(t,f)\, S_+^*(t,f). \tag{4.3}$$

Differentiating with respect to time yields a new distribution $N_s$. Similar to the Page distribution, it is a time-dependent power spectrum.

$$\begin{aligned} \mathrm{N}_s(t,f) &= -\frac{\partial}{\partial t}\left[|S_+(t,f)|^2\right] && (4.4)\\ &= \frac{\partial}{\partial t}\left[-S_+(t,f)\, S_+^*(t,f)\right] && (4.5)\\ &= -S_+(t,f)\,\frac{\partial}{\partial t}\left[S_+^*(t,f)\right] - S_+^*(t,f)\,\frac{\partial}{\partial t}\left[S_+(t,f)\right]. && (4.6) \end{aligned}$$

Substituting using Eq. 4.2 yields the alternative form

$$\mathrm{N}_s(t,f) = S_+(t,f)\left[-\frac{\partial}{\partial t}\int_t^\infty s^*(\theta)\, e^{j2\pi f\theta} d\theta\right] + S_+^*(t,f)\left[-\frac{\partial}{\partial t}\int_t^\infty s(\theta)\, e^{-j2\pi f\theta} d\theta\right] \tag{4.7}$$

$$\begin{aligned} &= S_+(t,f)\, s^*(t)\, e^{j2\pi ft} + S_+^*(t,f)\, s(t)\, e^{-j2\pi ft} && (4.8)\\ &= 2\,\mathrm{Re}\left\{s^*(t)\, S_+(t,f)\, e^{j2\pi ft}\right\} && (4.9) \end{aligned}$$

Continuing with $\lambda = t - \theta$,

$$\begin{aligned} \mathrm{N}_s(t,f) &= 2\,\mathrm{Re}\left\{\int_t^\infty s^*(t)\, s(\theta)\, e^{j2\pi ft} e^{-j2\pi f\theta} d\theta\right\} && (4.10)\\ &= 2\,\mathrm{Re}\left\{-\int_\infty^t s^*(t)\, s(\theta)\, e^{j2\pi f(t-\theta)} d\theta\right\} && (4.11)\\ &= 2\,\mathrm{Re}\left\{\int_{-\infty}^0 s^*(t)\, s(t-\lambda)\, e^{j2\pi f\lambda} d\lambda\right\}. && (4.12) \end{aligned}$$

Proceeding onward to the time-lag kernel, Eq. 4.12 is recast using the unit step function $u(t)$ and with a $\tau = -\lambda$ substitution, where $\tau$ represents lag,

$$\mathrm{N}_s(t,f) = 2\,\mathrm{Re}\left\{\int_{-\infty}^{\infty} s^*(t)\,s(t-\lambda)\,u(-\lambda)\,e^{j2\pi f\lambda}d\lambda\right\} \tag{4.13}$$

$$= 2\,\mathrm{Re}\left\{\underset{\tau\to f}{\mathcal{F}}\left\{s^*(t)\,s(t+\tau)\,u(\tau)\right\}\right\} \tag{4.14}$$

$$= \underset{\tau\to f}{\mathcal{F}}\left\{s^*(t)\,s(t+\tau)\,u(\tau)\right\} + \left[\underset{\tau\to f}{\mathcal{F}}\left\{s^*(t)\,s(t+\tau)\,u(\tau)\right\}\right]^*. \tag{4.15}$$

Taking the inverse Fourier transform yields the smoothed instantaneous autocorrelation function $R_s$,

$$R_s(t,\tau) = s^*(t)\,s(t+\tau)\,u(\tau) + s(t)\,s^*(t-\tau)\,u(-\tau) \tag{4.16}$$

$$= u(\tau)\left[\delta\left(t+\frac{\tau}{2}\right) \underset{t}{*} K_s(t,\tau)\right] + u(-\tau)\left[\delta\left(t-\frac{\tau}{2}\right) \underset{t}{*} K_s(t,\tau)\right] \tag{4.17}$$

$$= \left[u(\tau)\,\delta\left(t+\frac{\tau}{2}\right) + u(-\tau)\,\delta\left(t-\frac{\tau}{2}\right)\right] \underset{t}{*} K_s(t,\tau), \tag{4.18}$$

where $K_s$ is simply the instantaneous autocorrelation function. Separating the time-lag kernel $G(t,\tau)$ unique to this distribution gives

$$G(t,\tau) = u(\tau)\,\delta\left(t+\frac{\tau}{2}\right) + u(-\tau)\,\delta\left(t-\frac{\tau}{2}\right) \tag{4.19}$$

$$= \delta\left(t+\left|\frac{\tau}{2}\right|\right). \tag{4.20}$$

The other kernels in this family of distributions are the Rihaczek, $G(t,\tau) = \delta\left(t-\frac{\tau}{2}\right)$, the Levin, $G(t,\tau) = \frac{1}{2}\left[\delta\left(t+\frac{\tau}{2}\right) + \delta\left(t-\frac{\tau}{2}\right)\right]$, and of course the Page, $G(t,\tau) = \delta\left(t-\left|\frac{\tau}{2}\right|\right)$. A graphical comparison of the Page kernel with this new one is provided in Figure 4.1.

## 4.2 Cross terms and rationale

To understand the reasoning behind the development of this distribution, it is necessary to examine the role cross-terms play in this type of quadratic time-frequency distribution. Mathematically, these cross-terms arise in the same way a cross-term is produced by multiplying together two linear polynomials. Graphically, they manifest as undesired

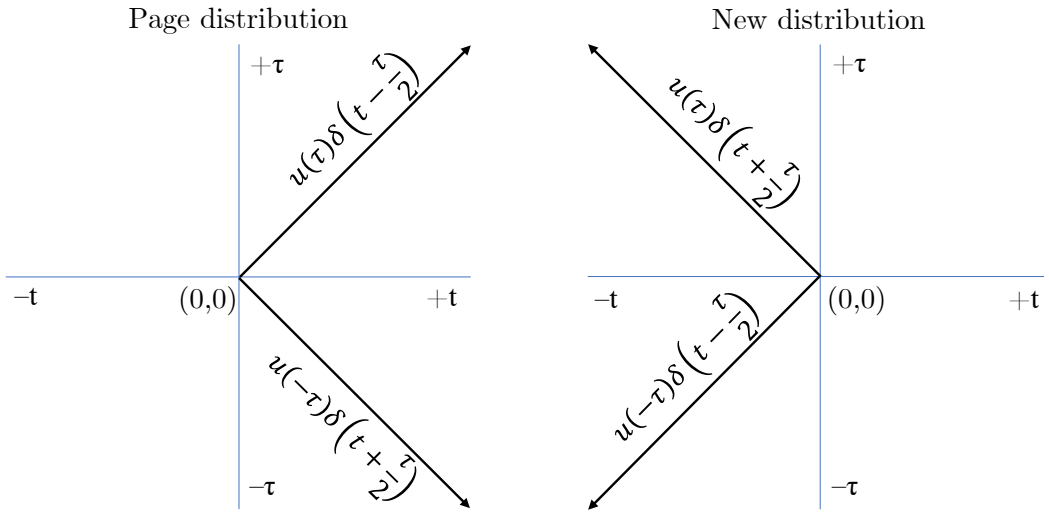


Figure 4.1: Graphical comparison of Page and proposed distribution kernels

artifacts in the time-frequency image. Often in time-frequency analysis, one can conceive of a signal being analyzed as a superposition (in time and/or frequency) of two or more components, which can roughly be defined as sensible conceptual divisions of the time-frequency energy comprising the signal. For instance, a frequency-modulated chirp can be thought of as such a component, since, though its energy is spread across time and frequency, it is described in a single mathematical expression with a particular rule governing its instantaneous frequency. Any given signal may contain multiple components which cannot be easily separated when examined solely in the time or in the frequency domain, where a time-frequency representation may permit such a separation. Cross-terms appear halfway between the signal components in the time-frequency image. It then can become challenging to identify legitimate signal components in a quadratic time-frequency distribution when the signal is not known beforehand. Examples of the various appearances cross-terms can take are shown in Section 3.2.

Also important to note is that this distribution is designed specifically with the analysis of elastic wave reradiation in mind. The relevant aspects of such a signal can be approximated as a train of closely- but irregularly-spaced high-bandwidth, short-duration sinc-like pulses—as a result of pulse compression on the echoes and reradiations from an

object of some elasticity and physical extent. Interestingly, distributions in this Rihaczek-Levin-Page family do well with these temporally-compressed signals in that they exhibit high resolution along the time-axis. This permits specular echoes and reradiations to be more easily separated in time when object size and waveform type may lead to tightly-grouped time-domain pulses.

The simplest example of elastic wave reradiation would be two consecutive sinc functions—the result of pulse compression on a specular and on a single elastic wave return (Figure 4.2). The instantaneous autocorrelation function $K_z$ (Eq. 3.5) of this signal takes on the appearance of four points at the corners of a diamond, as shown in Figure 4.3. Since the structure is foundational to this type of signal, it is useful to consider briefly why it occurs. Approximate the sinc functions with delta functions, such that the signal $z(t)$ becomes

$$z(t) = \delta(t) + \delta(t - l), \tag{4.21}$$

where $l$ is the time delay between the arrival of the specular return and the elastic return. $K_z$ is then

$$\begin{aligned} K_z(t,\tau) &= \left[\delta\left(t+\frac{\tau}{2}\right) + \delta\left(t+\frac{\tau}{2}-l\right)\right]\left[\delta\left(t-\frac{\tau}{2}\right) + \delta\left(t-\frac{\tau}{2}-l\right)\right] && (4.22)\\ &= \delta\left(t+\frac{\tau}{2}\right)\delta\left(t-\frac{\tau}{2}\right) + \delta\left(t+\frac{\tau}{2}-l\right)\delta\left(t-\frac{\tau}{2}-l\right) && (4.23)\\ &\quad + \delta\left(t+\frac{\tau}{2}\right)\delta\left(t-\frac{\tau}{2}-l\right) + \delta\left(t-\frac{\tau}{2}\right)\delta\left(t+\frac{\tau}{2}-l\right). \end{aligned}$$

Each term gives a two-dimensional delta in $K_z$, one each at $(0,0)$, $(l,0)$, $\left(\frac{l}{2},l\right)$, and $\left(\frac{l}{2},-l\right)$. The latter two are the aforementioned cross terms. Moving into the smoothed instantaneous autocorrelation function $R_z$ by way of time-convolution with the Wigner-Ville kernel $G(t,\tau) = \delta(t)$, and then into the Wigner-Ville distribution through a Fourier transform, the basic problem for use with elastic wave reradiation is apparent. The cross terms produce a false component of the reradiation signature. (Compare the time series in Figure 4.2 and its Wigner-Ville distribution in Figure 4.4.) The other kernels in this

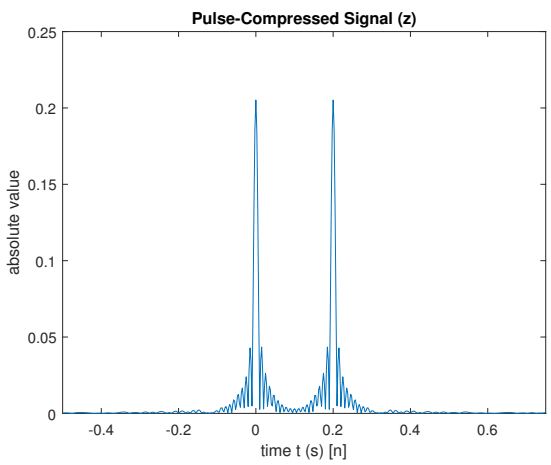


Figure 4.2: Simple model of elastic wave reradiation, time series, pulse-compressed

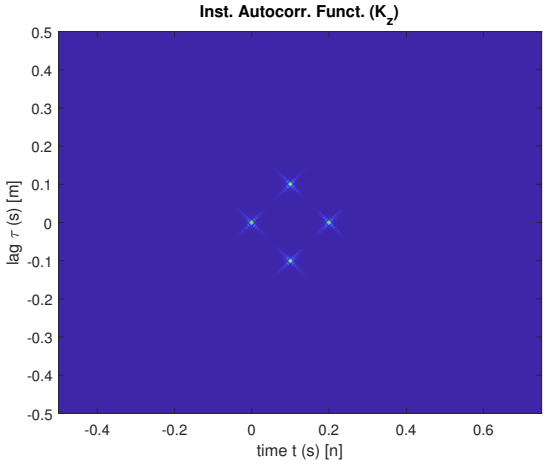


Figure 4.3: Instantaneous autocorrelation function of simple EWR model

distribution family under consideration place the Wigner-Ville kernel delta on a slope through the time-lag plane. Significantly, this shifts the cross terms away from being temporally situated between the specular and reradiated returns, and thus no longer in danger of misconstrual. This is accomplished by variously shifting the terms forward and backward to align with the specular and reradiated returns. (See Figures 4.5, 4.6, 4.7, and 4.8.) The downside is that the spectral content of the cross terms contaminates that of the desired terms, meaning that a frequency-filtering effect of an elastic surface wave interaction may be unobservable. (See Figures 4.9 and 4.10.) The Page distribution (Figure 4.11) notably removes the false signature and keeps the cross terms off of the specular return. While potentially useful, the theory of elastic wave reradiation for sonar suggests that the spectral content of the reradiation may be much more informative for target classification purposes than that of the specular return. What is needed is a sort of mirror of the Page distribution which dumps the cross terms atop the specular return, where the contamination is comparatively unimportant, while retaining the integrity of the reradiated spectrum, and this is the time-frequency distribution here proposed (Figure 4.12). More realistic elastic wave return models of course generate a more complicated collection of cross terms which is not so easily dealt with, but the simple case illustrates the strategy of applying this distribution.

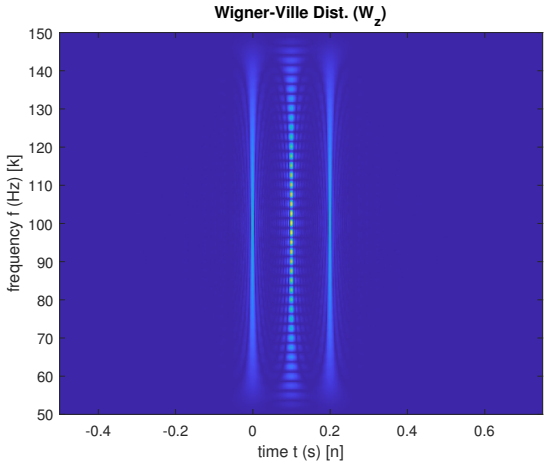


Figure 4.4: Wigner-Ville distribution of simple EWR model

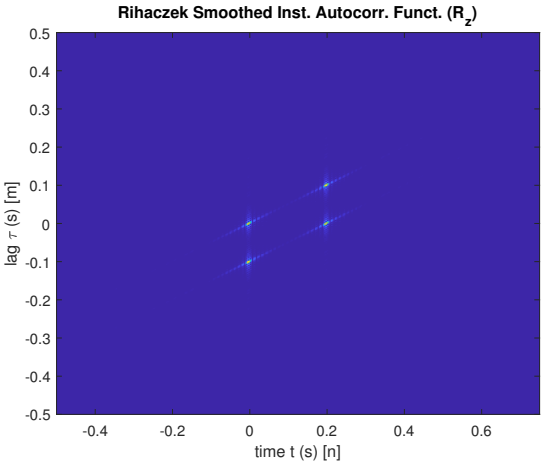


Figure 4.5: Smoothed instantaneous autocorrelation function using Rihaczek kernel

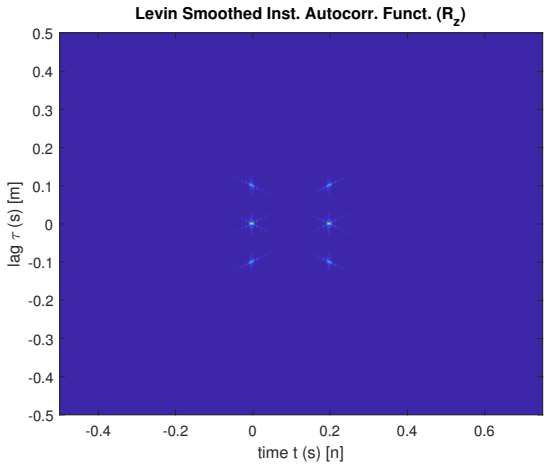


Figure 4.6: Smoothed instantaneous autocorrelation function using Levin kernel

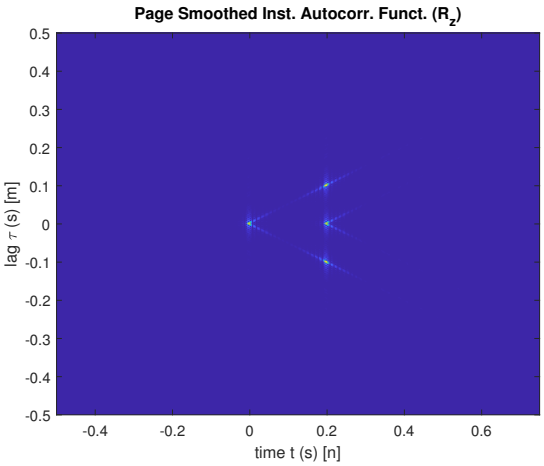


Figure 4.7: Smoothed instantaneous autocorrelation function using Page kernel

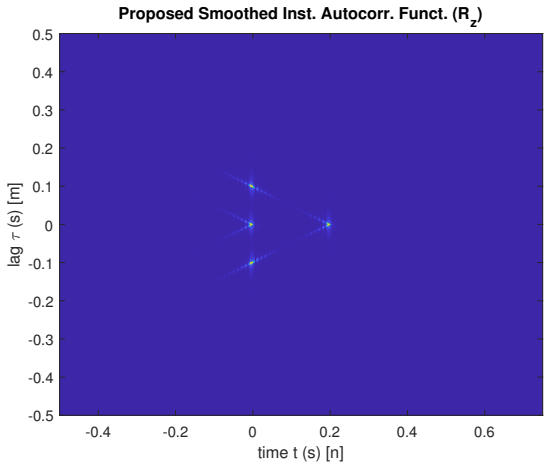


Figure 4.8: Smoothed instantaneous autocorrelation function using proposed kernel

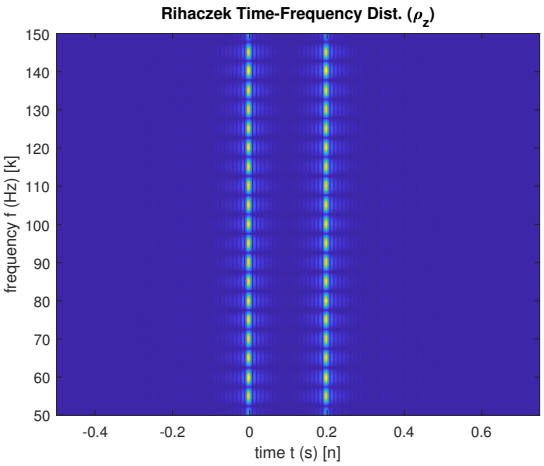


Figure 4.9: Rihaczek distribution of simple EWR model

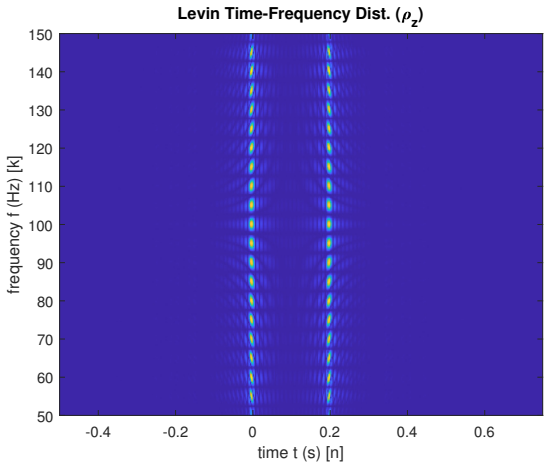


Figure 4.10: Levin distribution of simple EWR model

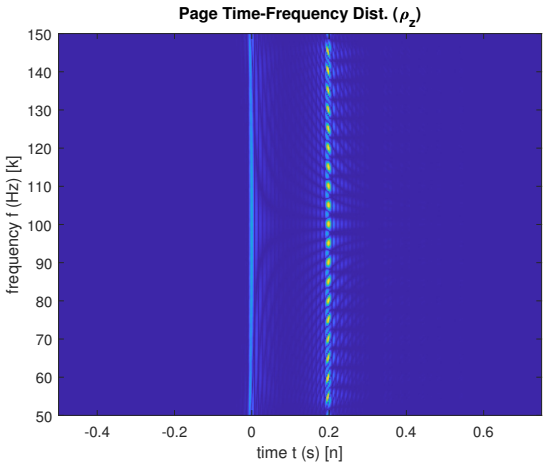


Figure 4.11: Page distribution of simple EWR model

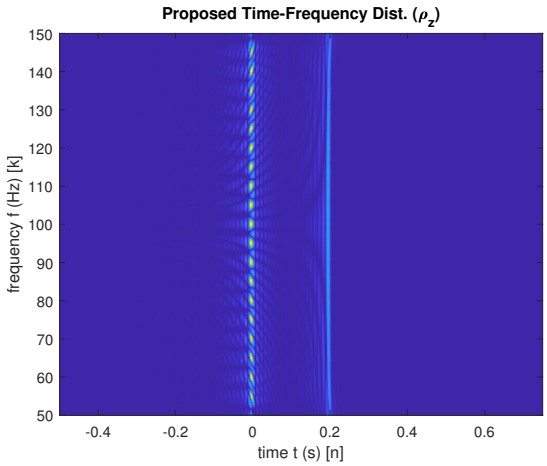


Figure 4.12: Proposed distribution of simple EWR model

It is true that windowing can improve the performance of the Rihaczek, Levin, and Page family of distributions with respect to elastic wave reradiation. This, however, requires a choice of window size which successfully separates the major elements of the acoustic response, allowing them to be effectively treated in isolation. In that case, the effect indeed is to retain the advantages of the family on pulse-compressed signals, while avoiding the inconvenient placement of cross terms. In practice, though, it is difficult to guarantee the window will isolate components sufficiently—especially in sonar applications where reflectors of interest may take on a wide variety of shapes, sizes, and internal structures. Time separation between the specular return and elastic wave

reradiation may well be quite short, and to shorten the window too much is to reduce the resolution with which the distribution can express the complexity of the spectrum. For these reasons the proposed distribution is advantageous; it allows all the benefits of windowing and when windowing is insufficient, it can move cross terms toward (or on top of) the specular return, which is less important for classification in this application.

# Chapter 5

## Elastic waves

As the application in view is the detection in sonar of reradiated elastic waves, it will be useful to consider the physical phenomena which would facilitate this. Solid materials possess a certain degree of elasticity and bending stiffness. Elasticity describes the tendency of a material to recover its original shape when a deforming force has been removed; it is commonly quantified by Young's modulus ($E$). Bending stiffness is simply the resistance of an object against bending; it depends upon Young's modulus for the material and the object's moment of inertia.

In the case of sonar, a transmitted acoustic pulse is incident upon the surface of an object, and as a longitudinal wave in the water, the pulse presents a deforming force to that surface. This will be referred to as acoustic loading. Because the object will deform or deflect under the loading and because its elasticity will restore its original shape, elastic surface waves will be induced in the object. The three broad categorizations of elastic surface waves are transverse, compressional, and shear, distinguishing the direction of particle motion in relation to the direction of wave propagation.

For transverse (or Rayleigh) waves this motion is parallel to the surface normal. When the object is a plate, these are called Lamb waves. Lamb waves are further divided into antisymmetric (or flexural), denoted by $a_0$, and symmetric (or extensional), denoted by $s_0$, depending on the relative phases of the waves on opposing sides of the plate. See Figure 5.1 for an illustration. When the flexural surface waves propagate more slowly than the acoustic waves in the surrounding medium, they are known as Scholte-Stoneley and as subsonic, denoted by $a_{0-}$. Waves denoted $a_{0+}$ (and often simply $a_0$) are mostly

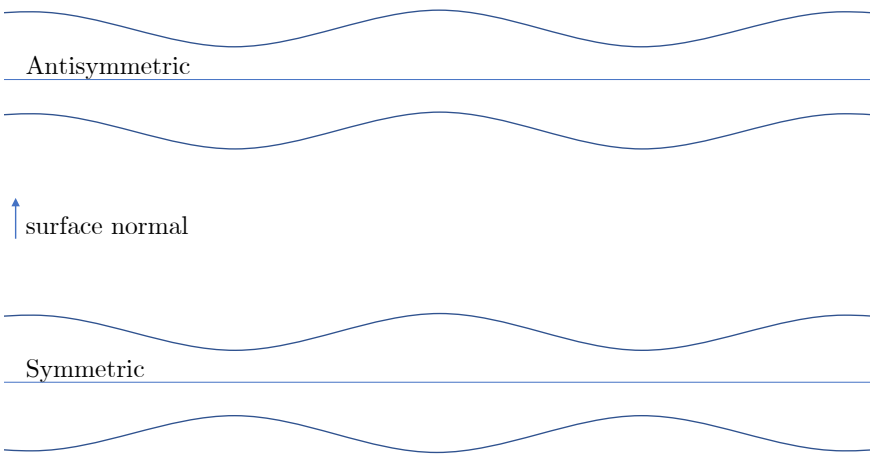


Figure 5.1: Antisymmetric Lamb waves compared to symmetric Lamb waves

supersonic. In the case of spherical or cylindrical shells, the propagation speed depends on the $ka$ product, where $k = \omega/c$ is the wavenumber and $a$ is the outer radius of the shell. Compressional (or longitudinal) waves have particle motion parallel to the direction of propagation. Shear wave motion occurs perpendicularly to both the surface normal and propagation direction.

Bruneau [9] notes that flexural waves are associated both with local changes in volume and shape of a plate. Thus the flexural waves are well-suited to sound radiation from the plate since acoustic loading creates them easily and since particle motion in the surrounding fluid is highly compatible with them.

It appears bending stiffness, more than elasticity alone, is responsible for the ability of an object to support and reradiate elastic surface waves capable of detection by sonar. Observation suggests that steel shells in the ocean, such as submarine hulls and naval mine shells, exhibit more elastic wave reradiation than a naturally-occurring and similarly-sized object such as a rock. This fits with intuition, as it is easy to excite surface waves which audibly couple into the air in an aluminum can and far more difficult to do so with a rock of the same size. Indeed, striking a rock creates sound associated with the impulse and little else; striking the aluminum can, however, generates a ringing as the surface of the can vibrates and can be heard long after the strike (notwithstanding

that this example involves non-linear acoustics and the proposed research will instead assume a linear model). One might suppose elasticity explains some of the difference in behavior, but it happens that aluminum and basalt, a common igneous rock in the ocean, have comparable Young's moduli. Another decisive difference in the objects is in their thicknesses. Aluminum, being much more malleable and ductile (able to be permanently deformed without breaking) than basalt, is found very thin in cans. Basalt, of course, is not found in such a shape. A more informative approximation, then, is likely the bending stiffness, which accounts additionally for the object's thickness in the form of its moment of inertia.

Consider a further illustrative example. [9] gives the bending stiffness $B$ of a plate as

$$B = \frac{Eh^3}{12\,(1-\nu^2)}, \tag{5.1}$$

where $h$ is the thickness of the plate, and $\nu$ is Poisson's ratio. The most common stainless steel is grade 304 (abbreviated SS304) and has a Young's modulus approximately three times greater than that of basalt and a comparable Poisson's ratio. Consequently, given two plates of the same shape, one of SS304 and the other of basalt, the latter will actually have less bending stiffness than the former. The basalt plate would bend more easily and would be better able to support elastic surface waves under acoustic loading. It appears, then, that the $h^3$ factor accounts for the discord with the above observation that stainless steel is associated with elastic surface wave reradiation rather than rock in acoustic research. The basalt plate would need only to be 50% thicker to have roughly the same bending stiffness as the stainless steel; if the basalt were twice as thick, it would be more than twice as stiff as the steel. The fact that stainless steel occurs in smooth, man-made shells, while basalt occurs in irregular, relatively thick formations, likely explains why the two materials may be differentiable in sonar—that is, the typical shape of the material, rather than the material itself.

Imagine the limiting case. Suppose it were possible for a material to have an infinite Young's modulus. An object composed of such material would be perfectly rigid. Regardless of the stress or loading applied, the object would exhibit no deformation—no

internal strain. Because of the principle of conservation of energy, incident acoustic loading would be entirely reflected (or be dissipated in the surrounding medium by another means), but the acoustic wave could not couple into the object and travel either across its surface or through its body. No bending of the rigid plate means no flexural waves. No compression and rarefaction of the composing molecules means no longitudinal waves. If, however, a plate has a finite Young's modulus, then incident acoustic energy is partially reflected on contact (known as the specular return) and partially absorbed into the molecular structure of the material as deformation. Elasticity determines that the energy absorbed in deformation is not permanently stored there, but rather that the restorative tendency passes that energy through the material and back into the surrounding medium (in addition to losses in the form of heat). As [9] notes and acoustic research concurs, flexural waves represent the most prominent contribution to the reradiated energy from an acoustically loaded shell.

In the case of thin elastic spherical shells researchers have observed a phenomenon known as the mid-frequency enhancement [22,29]. Near the coincidence frequency (where $ka = a/h$), constructive interference among circumnavigating $a_{0-}$ waves results in a strong backscattering effect temporally removed from the specular return—an effect which can have an amplitude three times that of the specular return. This elastic reradiation can be observed at varying bistatic angles, although the amplitude is significantly reduced [1]. (Monostatic sonar has the transmitter and receiver co-located, whereas bistatic sonar has them separated. The bistatic angle is measured at the point of reflection between the transmitter and receiver.) Simple rearrangement and substitution of $ka = a/h$ yields $f = c/2\pi h$, where $f = \omega/2\pi$, and this allows an estimation of where the mid-frequency enhancement will be observed for various shell thicknesses. Figure 5.2 shows the approximate coincidence frequency as a function of spherical shell thickness for a sound speed of $c = 1500\,\mathrm{m/s}$. The important conclusion from this figure is that practical sonar systems are in operation at the coincidence frequencies for shell thicknesses in common use. In other words, extant systems should be able to observe this phenomenon.

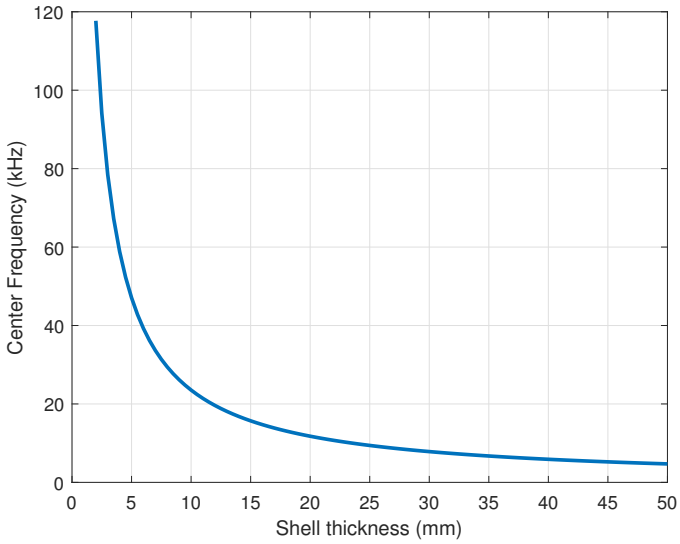


Figure 5.2: Coincidence frequency as a function of spherical shell thickness

# Chapter 6

# Measurement

In order to measure the suitability of a given time-frequency method for identifying the elastic wave reradiation it will be necessary to apply quantitative measures. These will differ for the simulation and collected acoustic data processing chapters since the numerical evaluations can only be made relative to known and objective criteria. The criteria during simulation will rely upon the fact that the simulated signal is known *a priori*, and therefore the fidelity of the distribution can be in at least three useful ways directly calculated. What is unknown in simulation is how faithful the simulated signal is to actual, physical elastic wave reradiation. Here, the collected acoustic data is beneficial. This data contains recordings of echoes from three cylindrical shells which differ only in material composition. The assumption will be that their shapes, sizes, and the conditions of data collection are sufficiently similar that any differences in the time-frequency representations will be due to the acoustic properties of the material. For this reason the attempt will be to quantify the difference between the time-frequency representations of different materials, holding the distribution constant.

## 6.1 Simulation

For the simulation portion of this study, this measurement will primarily involve quantifying the following concepts for the EWR application:

1. Separability of the components of the time-frequency image—namely, how easily the elastic wave reradiation can be isolated from the specular return.

2. Accuracy with which spectral nuances in the elastic wave reradiation can be shown.

3. Signal-to-noise ratio.

Naturally, a time-frequency distribution will be preferable for analyzing elastic wave reradiation to the extent that it clearly separates components of the signature without cross term artifacts and to the extent that it accurately reveals the spectral composition of the reradiation components.

### 6.1.1 Separation

Separation $S$ between the spectral return and elastic wave reradiation will be measured by the following weighted average:

$$S = \frac{\sum_{k=\mathrm{BW}} \sum_{n=n_{\mathrm{spec}}}^{n_{\mathrm{ewr}}} \left|\rho_z\left[n,k\right]\right| \left|n - \frac{1}{2}\left(n_{\mathrm{spec}} + n_{\mathrm{ewr}}\right)\right|}{\sum_{k=\mathrm{BW}} \sum_{n=n_{\mathrm{spec}}}^{n_{\mathrm{ewr}}} \left|\rho_z\left[n,k\right]\right| \cdot \frac{1}{2}\left(n_{\mathrm{ewr}} - n_{\mathrm{spec}}\right)}, \tag{6.1}$$

where BW is frequency sample indices of the transmit waveform bandwidth, $n_{\mathrm{spec}}$ the time sample index centered on the specular return, $n_{\mathrm{ewr}}$ the time sample index centered on the elastic wave reradiation, and $\rho_z\left[n,k\right]$ the discrete distribution indexed in time ($n$) and frequency ($k$). Basically, this is a weighted average of the time difference magnitude between each $\rho_z$ sample and the time midpoint between the specular return peak and the elastic wave reradiation peak, and this only for samples between the peaks and within the bandwidth of the transmit signal. The weighting is the magnitude of $\rho_z$. Thus, when a distribution concentrates energy at the points of the specular and elastic wave reradiation returns and avoids intervening energy (like cross-terms) it will receive a higher separation score. The denominator term $\frac{1}{2}\left(n_{\mathrm{ewr}} - n_{\mathrm{spec}}\right)$ is merely a scaling factor representing the maximum average. The maximum score of 1 arises when all energy occurs only at the points of the specular return and the elastic wave reradiation return, in which case the weighted average will be equal to the scaling factor. The worst score, when all energy is concentrated at the midpoint, is 0; in practice, however, 0 is not really possible since energy must necessarily exist at the point of the assumed specular return, which in any meaningful score will not be the midpoint.

### 6.1.2 Spectral accuracy

To estimate the error with which the time-frequency distribution represents the spectrum of the elastic wave reradiation, the following straightforward metric will be used:

$$\mathrm{Err} = \sum_{k} \left| \frac{|\rho_z [n_{\mathrm{ewr}}, k]|}{a_\rho} - \frac{|X_{\mathrm{ewr}} [k]|}{a_X} \right|^2, \tag{6.2}$$

where $X_{\mathrm{ewr}}$ is the discrete Fourier transform of the elastic wave reradiation in isolation. $a_\rho$ and $a_X$ are scale factors defined based on the root-mean-square of the function to be scaled:

$$a_\rho = \sqrt{\frac{1}{N_k} \sum_{k} |\rho_z [n_{\mathrm{ewr}}, k]|^2}, \tag{6.3}$$

$$a_X = \sqrt{\frac{1}{N_k} \sum_{k} |X_{\mathrm{ewr}} [k]|^2}, \tag{6.4}$$

where $N_k$ is the number of samples summed over $k$.

### 6.1.3 Signal-to-noise ratio

Concerning the signal-to-noise ratio of a time-frequency distribution, the results of Seddighi et al. [38] are interesting. They derive an approach based on the distribution kernel. In this case cross terms are considered as part of the signal rather than noise. For discrete signals this SNR is given by

$$\mathrm{SNR} = \frac{E_s \sum_{m=-\frac{M}{2}}^{\frac{M}{2}} \sum_{n=-\frac{N}{2}}^{\frac{N}{2}} \gamma (m, n)}{N \sigma_\varepsilon^2 \sum_{m=-\frac{M}{2}}^{\frac{M}{2}} g (m)}. \tag{6.5}$$

$E_s$ represents signal energy given by $TP_s$ for signal period $T$ and average signal power $P_s = E \left\langle |s (t)|^2 \right\rangle$, where $E$ is an expected value and $\langle \cdot \rangle$ denotes an average across time. $M$ and $N$ represent the time and frequency support of the distribution, respectively. $\sigma_\varepsilon^2$ gives noise variance, and $g (m)$ is a discrete version of $g (t) = \int_{-\infty}^{\infty} G (t - u, 0)\, du$. As in previous chapters, $\gamma$ gives the time-frequency kernel and $G$ the time-lag kernel.

For the present investigation, however, a simpler approach is afforded by the nature of the simulation in that the signal and noise can be generated completely in isolation from one another. This takes the form (as in [16]),

$$\mathrm{SNR} = \frac{\sum_{m=0}^{M-1}\sum_{n=0}^{N-1}\left|\rho_z\left(m,n\right)\right|^2}{\sum_{m=0}^{M-1}\sum_{n=0}^{N-1}\left|\rho_N\left(m,n\right)\right|^2}, \tag{6.6}$$

where $\rho_N$ is the time-frequency distribution under consideration but with only noise as the input.

## 6.2 Acoustic tank data

Quantifying the performance of the distributions for the collected acoustic tank data is not so simple, as the true breakdown of the recorded signal into its specular and reradiated components is not known, nor is it known what effective frequency filtering is performed on the reradiated component by the physical process. However, the difference in material for the targets collected with the same waveforms at the same incident angles is known, so the goal will be to find which distributions maximize the measurement of that material difference. It is important to note that this metric should not be interpreted in the absence of the simulation metrics, since this simple difference might be enhanced by the presence of a prominent cross term artifact, for instance, when such an artifact really provides no benefit (or is counterproductive) to the time-frequency analysis. Let a root-mean-square normalized time-frequency distribution be defined as

$$\hat{\rho}_{z,A}\left[n,k\right] = \frac{\left|\rho_{z,A}\left[n,k\right]\right|}{\sqrt{\frac{\sum_{n=1}^{N}\sum_{k=1}^{K}\left|\rho_{z,A}[n,k]\right|^2}{NK}}}, \tag{6.7}$$

where $\rho_{z,A}\left[n,k\right]$ is the discrete time-frequency distribution of the cylinder of material $A$ and the mean is performed over a region of interest bounded by the apparent specular component of the acoustic response and by the bandwidth of the transmitted waveform. This boundary shall be represented by $1 \leq n \leq N$ and $1 \leq k \leq K$ as the time and

frequency indices, respectively. The difference metric $D$ will be expressed as

$$D = \sum_{n=1}^{N} \sum_{k=1}^{K} \left| \hat{\rho}_{z,A}\left[n,k\right] - \hat{\rho}_{z,B}\left[n,k\right] \right|. \tag{6.8}$$

$D$ will then be averaged across all incident angles and transmitted waveforms for each pair of compared materials.

# Chapter 7

# Simulation

## 7.1 Preliminary

Simulations seem preferable for first addressing the evaluation of time-frequency methods for identifying elastic wave reradiation. Any attempt to base the evaluation solely on real data would be open to critique of the data collection methodology. By simulation is meant an estimated fabrication of the return which does not involve calculations with acoustics models, which would be beyond the scope of this work—rather only experimentation with the simple variables at the point of recording. So the procedure will first be to simulate signals with and without delayed reradiation in accordance with the manner in which the acoustic literature predicts it. There will be two major variables examined:

1. Delay between specular return and reradiated return.

2. Frequency-dependent filters applied to the reradiated return but not the specular return.

The purpose of the second is related to the degree to which the amplitude of the reradiated return varies with frequency. The literature describes significant frequency-dependent variation in the tendency for elastic surface waves to be excited under acoustic loading. The most prominent feature is perhaps the mid-frequency enhancement. Frequency variation arises not only in the acoustic coupling from fluid to surface, but also as the elastic surface wave propagates before reradiation. Anderson [1] describes the faster attenuation of higher frequencies in the elastic solid. This results in an elastic reradiation of an apparently lower center frequency. Characterizing this as a frequency shift is misleading, as

there seems to be no mechanism of turning one frequency into another, but rather that higher frequencies are suppressed through their more rapid attenuation. Certain time-frequency methods may better highlight the nature of the apparent frequency filtration applied to the reradiated return. Such information could be used to refine classification strategies.

Many of the time-frequency methods under consideration introduce their own parameters to the simulations along with choices of window type and width. Selections should be made in an attempt to reach the best possible performance of each time-frequency distribution for the problem at hand. The goal is to maximize both the energy separation between the specular return and the elastic wave reradiation and the accuracy with which a filter simulating the frequency-dependent effects of the reradiation process can be estimated. Not every tested value for each parameter will be reproduced here in figures, but instead the immediate vicinity of the best values will be shown. It is considered an advantage if the distribution does not require particular fine-tuning in order to perform well.

Signal parameters such as the time-bandwidth product, sample rate, and waveform type could be varied, as well. Differences between the matched filter and deconvolution have been previously discussed in Chapter 2, and for the reasons given there the deconvolution will be chiefly used. The primary concern here, however, is, given a representative sonar scenario, the determination of which distribution will perform best. There are already an abundance of variables in this simulation, so the simulation will be tailored to the scope. Window width will be varied, but because differences are likely greater between the distributions than between window types, the hunt for the perfect window will be postponed. A Hann window will be kept constant for the experiment. Also, rather than vary all three major signal variables simultaneously, a typical value for each will be chosen and kept constant while each other variable is swept independently across a range of interest. A handful of distribution parameter values will be chosen in the region of apparent best performance to optimize the distribution to the problem. Particular

care will be taken with the Zhao-Atlas-Marks distribution, which is affected by both a parameter and a choice of window width, and thus two variables to try to optimize.

There is, of course, the question: what does it mean to optimize a given time-frequency distribution for this problem? Both separation and spectral accuracy are desired. This is the reason simulations will not be restricted to a choice of one distribution parameter value or to a choice of one window width. The range and sampling of chosen values reflect the processing trade-off, and conclusions can be drawn afterward.

To keep the scope of the simulations under control, it is worth noting that it will not be necessary to test many different combinations of waveform bandwidth $f_{\mathrm{BW}}$ and pulse duration $T$. Instead, the product of these two values, referred to as the time-bandwidth product, determines the width of the main lobe in pulse compression output which is fed into the time-frequency distribution. Thus, a given time-bandwidth product could be achieved regardless of whether a high or low frequency sonar system is being used. Secondly, changing the time-bandwidth product will only result in a change in the width of the main lobe after pulse compression, and, the product being held constant for the experiment, will not materially affect the relative performances of the time-frequency distributions. An explanation of the dependence of the pulse compression main lobe width on the time-bandwidth product is provided in Appendix B.

Five different types of frequency filter will be applied to the elastic wave reradiation component to see how accurately the distribution is able to reveal the effects of this filtering. The default will be no filter—meaning physically that the specularly reflected and reradiated signals have the same frequency content—which shall be referred to as flat. The other frequency filters will take the following shapes, mimicking the effect of a suppression of certain frequencies within the waveform bandwidth in the process of elastic waves reradiation:

1. A triangular window (TW), peaking in the center of the bandwidth and tapering to zero at the edges.

2. A triangular notch (TN), zero in the center of the bandwidth and rising to the edges.

3. A Hann window (HW), peaking in the center of the bandwidth and tapering to zero at the edges.

4. A Hann notch (HN), zero in the center of the bandwidth and rising to the edges.

## 7.2 Time-frequency distributions

This section will describe the performance of each quadratic time-frequency distribution, including the one proposed in this dissertation, on simulated elastic wave reradiation based on the above criteria. The last section in the chapter will describe conclusions drawn therefrom. The primary simulated transmission waveform will be a linear frequency-modulated chirp running from 50 Hz to 150 Hz over a pulse duration of 1 s, resulting in a time-bandwidth product of 100. The sampling rate is simulated at 400 Hz. This is the same as was used in the simple elastic wave reradiation model used in chapter 4 and which will build in complexity upon it. Noise will be Gaussian in distribution. The instantaneous autocorrelation function $K_z$ and the Wigner-Ville distribution $W_z$ of the basic model containing merely a specular echo component and one well-defined elastic wave reradiation component of equal magnitude occurring 0.2 s later are shown in Figures 4.3 and 4.4, respectively. The remaining two domains in the time-frequency analysis quartet, that of Doppler-lag ($A_z$, called the symmetric ambiguity function) and of Doppler-frequency ($k_z$, called the spectral autocorrelation function) are given in Figures 7.1 and 7.2.

In the course of the analysis, it will be preferable to examine each distribution at its best, so appropriate values for the parameters and window sizes must be chosen. This will be done by varying the parameters and selecting a value which reasonably results in low spectral error and high separation scores, as defined above.

### 7.2.1 Spectrogram

Beginning with the spectrogram, a baseline of performance will be established. The essential trade-off with the spectrogram comes from choice of window size. The narrower the window, the more separation can be achieved between components of the return;

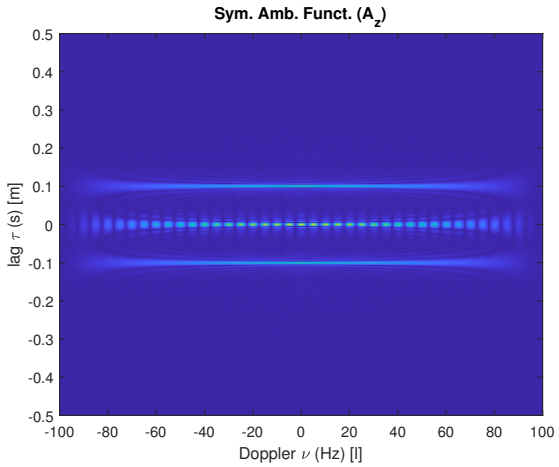


Figure 7.1: Symmetric ambiguity function of basic EWR model

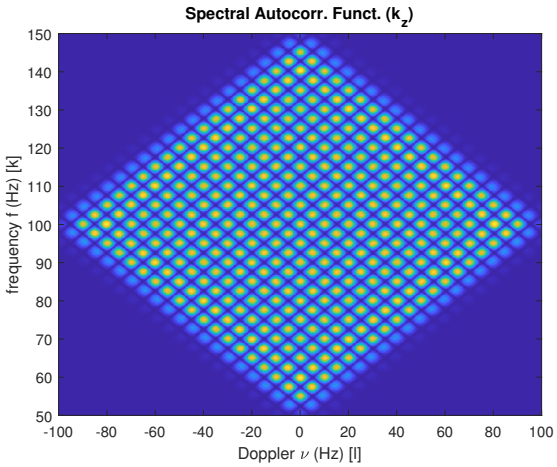


Figure 7.2: Spectral autocorrelation function of simple EWR model

however, the narrower window also reduces the frequency resolution, making it more difficult to evaluate the spectrum of each component. Figures 7.3 and 7.4 illustrate this choice with no spectral filtering applied to the elastic wave radiation. The advantage of the smaller window is clear in the first of these, as a small window size produces good separation scores across a wide range of delays. Figure 7.4 might entice one to choose a particularly narrow window, such as 0.02 s or 0.03 s, but this would only work well if there were not complicated variations in the spectral information. For instance, while the separation and spectral error look much the same for the triangular window described above, these smaller window sizes struggle with the triangular notch (see Figure 7.5). The high error region in the bottom-right corner of the spectral error plots results from the interaction of the specular component with the EWR component when the delay is small, creating artifacts. The separation score is very similar across the types of spectral filter placed on the EWR investigated here.

### 7.2.2 Wigner-Ville distribution

The Wigner-Ville distribution produces much finer time-frequency resolution than the spectrogram but has a very prominent cross-term as shown in Figure 4.4, which heavily penalizes the separation metric (see Figure 7.6). It is also deficient in its spectral accuracy for this application. In this respect, auto-terms, rather than cross-terms, prove to be the

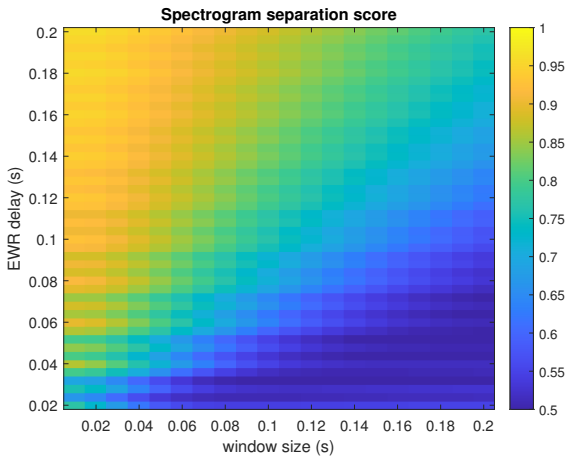


Figure 7.3: Spectrogram separation; no filter

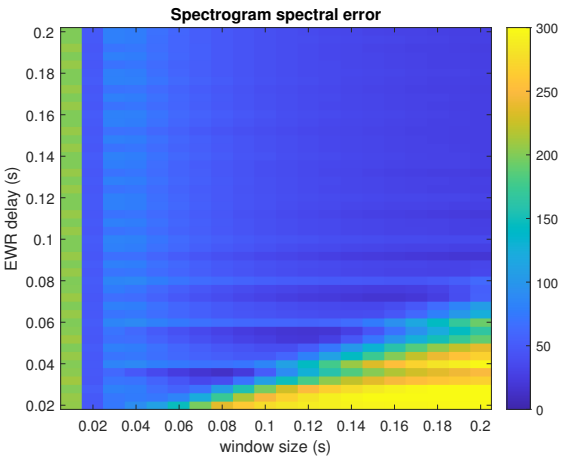


Figure 7.4: Spectrogram spectral error; no filter

problem. While the frequency content along the vertical line of the EWR in the time-frequency plane is nicely isolated from other content, the auto-terms resulting from the interaction between each bit of energy on the vertical line and each other bit on that same line cause the concentration of energy to be highest in the center of that vertical-line component and taper to the ends. This can be misleading for evaluating the relative intensities of the frequency content in the signal. When comparing the EWR filters, for instance, errors vary significantly. If a triangular window filter is used, spectral errors will be very low as the distribution naturally produces a triangularly-shaped intensity to the components, but the triangular notch produces significant error since it opposes this natural component shape (see Figure 7.7).

### 7.2.3 Windowed Wigner-Ville distribution

The windowed Wigner-Ville attempts to mitigate the cross terms of the Wigner-Ville, adopting the window-size trade-off of the spectrogram. It does achieve generally better separation between the specular and EWR returns than does the spectrogram on a wide range of window sizes and delays (see Figures 7.8 and 7.3). It does still suffer considerably when it comes to accuracy (see Figure 7.9), but this has more to do with the nature of the distribution than the windowing. The explanation in Subsection 7.2.2 also applies here. Figures 7.10 and 7.11 demonstrate this difference by comparing the reference FFT

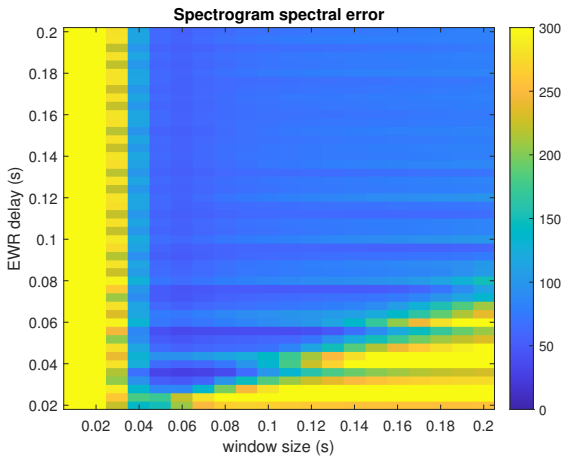


Figure 7.5: Spectrogram spectral error; TN filter

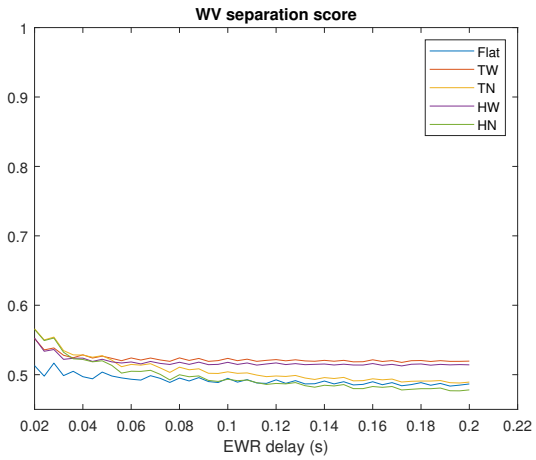


Figure 7.6: Wigner-Ville separation by EWR filter and delay

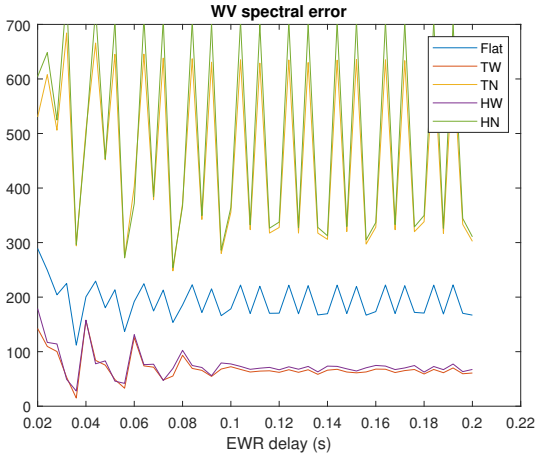


Figure 7.7: Wigner-Ville spectral error by EWR filter and delay

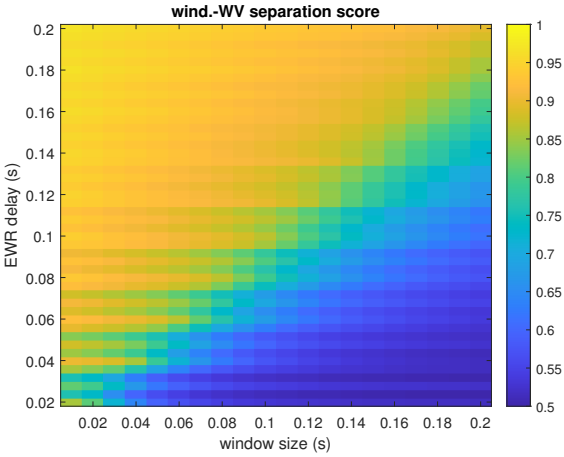


Figure 7.8: Windowed Wigner-Ville separation; no filter

of the simulated EWR to the spectral cross-section of the time-frequency distribution at the corresponding moment in time (EWR delay of 0.1 s and window width of 0.1 s).

### 7.2.4 Levin distribution

Regarding the separation score, the Levin distribution offers a substantial improvement over the Wigner-Ville by removing the cross-term from between the components (see Figures 4.10 and 7.12), but this compromises accuracy by essentially piling the cross-terms atop the specular and EWR components. Note in Figure 7.13, that while not as bad as the worst performance of the Wigner-Ville with the notched filters, it also does

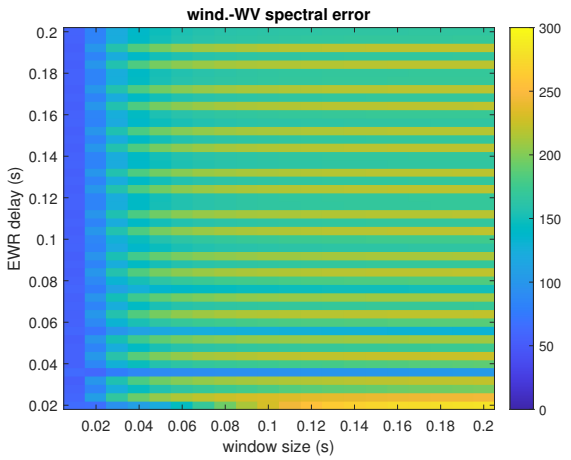


Figure 7.9: Windowed Wigner-Ville spectral error; no filter

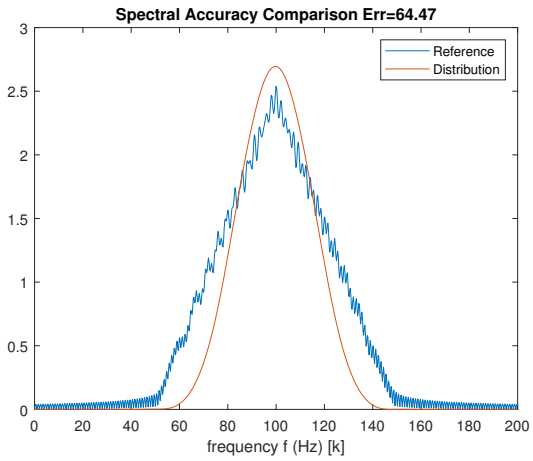


Figure 7.10: Windowed Wigner-Ville EWR spectral accuracy; TW filter

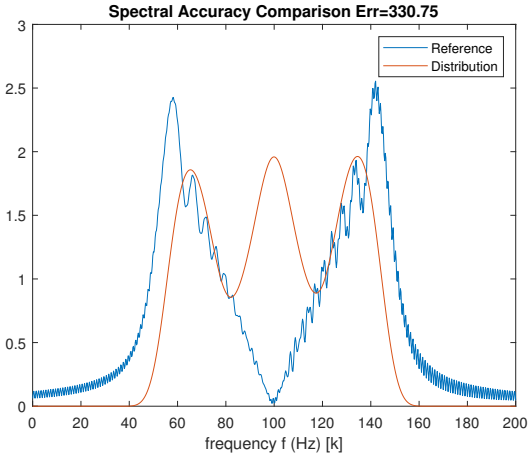


Figure 7.11: Windowed Wigner-Ville EWR spectral accuracy; TN filter

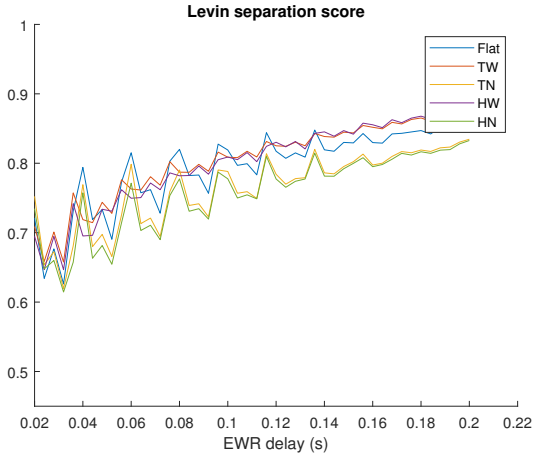


Figure 7.12: Levin separation by EWR filter and delay

not achieve that distribution's best results on the window filters, and would be difficult to use effectively for this application.

### 7.2.5 Windowed Levin distribution

As with the Wigner-Ville distribution, windowing serves to remove cross-terms by isolating components with a sufficient time separation. Compare Figure 7.14 with Figure 4.10 to observe the difference after applying a 0.1 s window. The separation scores are relatively unchanged in comparison with the non-windowed Levin (see Figures 7.15 and

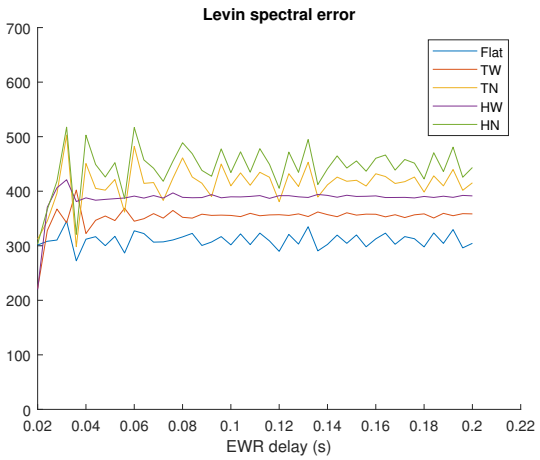


Figure 7.13: Levin spectral error by EWR filter and delay

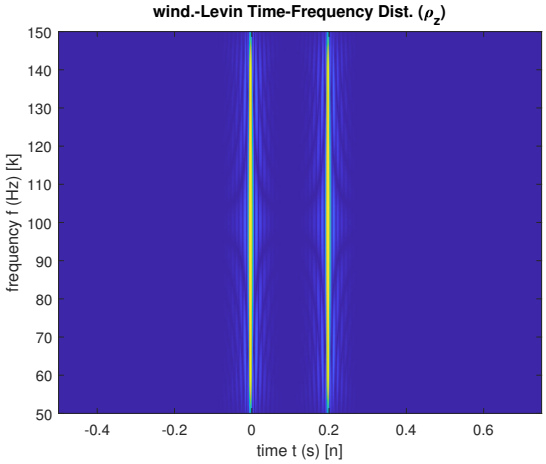


Figure 7.14: Windowed Levin EWR distribution

7.12), but this is to be expected, since the Levin already keeps cross-terms from occurring between two components. Interestingly, however, the fact that a cross-term is now superimposed upon the EWR component makes windowing a proposition which reduces spectral error for that component (see Figures 7.16 and 7.13). To the degree, then, that the window sufficiently isolates the components, the spectral error is significantly reduced over the non-windowed form. Adding the spectral filters to the EWR component does not produce any substantially different result. Spectral errors with a filter applied tend to be higher when the window is either much too narrow or when it is too long given the EWR delay. The notch filters result in a somewhat lower separation score across window size and delay.

### 7.2.6 Page distribution

The performance of the Page distribution looks very similar to that of the Levin since it has the same issue of displacing the typical cross-term position—that of being between the vertical components—to superposition with the EWR component. The primary difference, shown in Figure 4.11, from the Levin is that no cross-term is placed atop the specular component. It was largely this observation (*i.e.* can the cross-terms be diverted

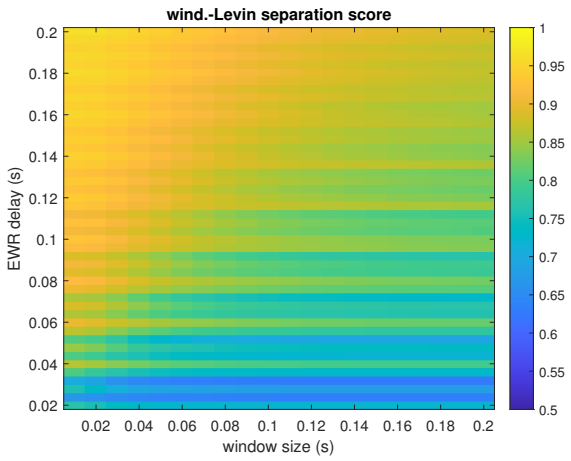


Figure 7.15: Windowed Levin separation; no filter

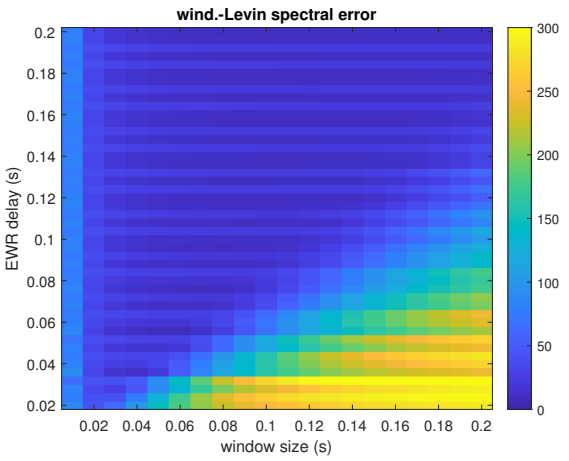


Figure 7.16: Windowed Levin spectral error; no filter

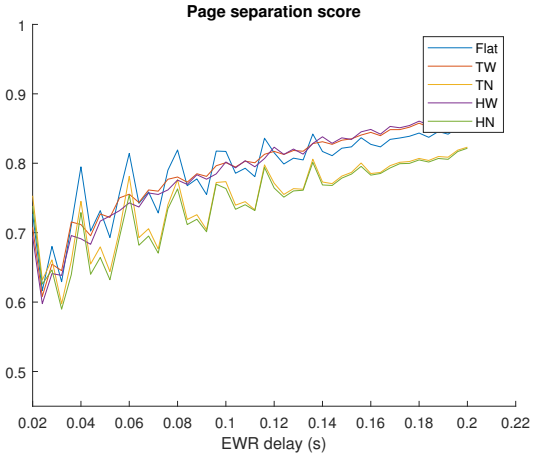


Figure 7.17: Page separation by EWR filter and delay

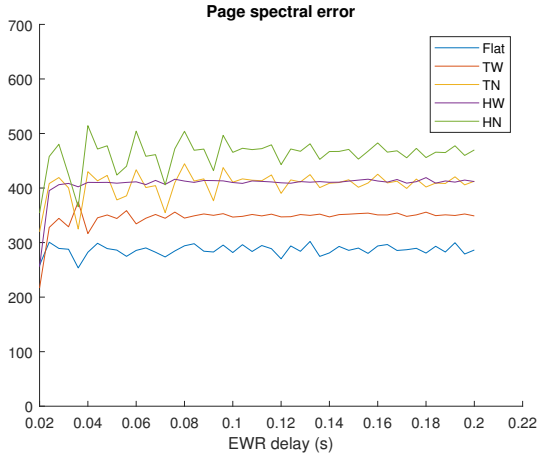


Figure 7.18: Page spectral error by EWR filter and delay

to the specular component instead?) which led to the development of the proposed distribution, which will be examined later. Figures 7.17 and 7.18 show the performance similarity with the Levin from Subsection 7.2.4.

### 7.2.7 Windowed Page distribution

As expected, windowing the Page distribution has a similar effect to that of windowing the Levin, and in fact, the separation scores are very similar (compare Figures 7.19 and 7.15). Spectral error is generally higher with the windowed Page (see Figure 7.20) than with the windowed Levin. This is a result of the fact that for EWR the cross-terms are all

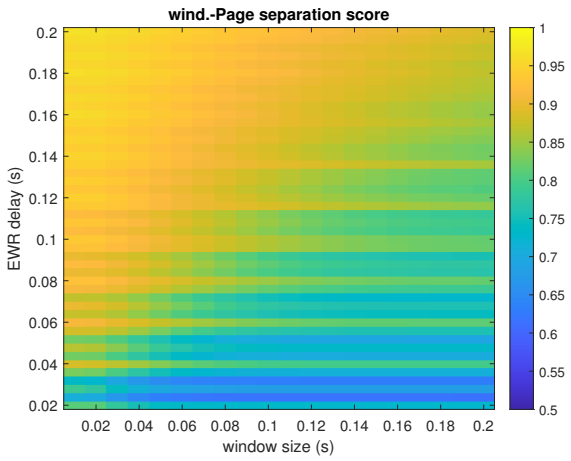


Figure 7.19: Windowed Page separation; no filter

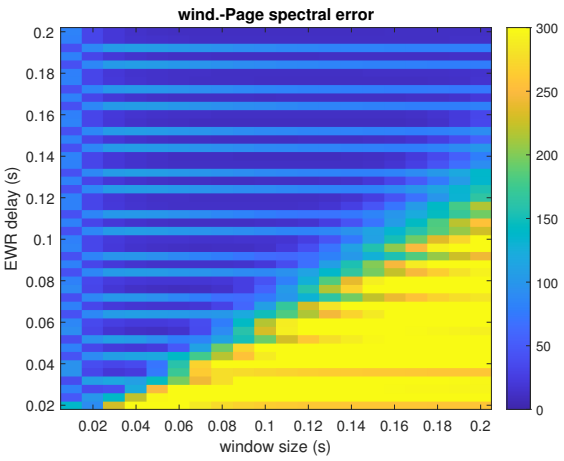


Figure 7.20: Windowed Page spectral error; no filter

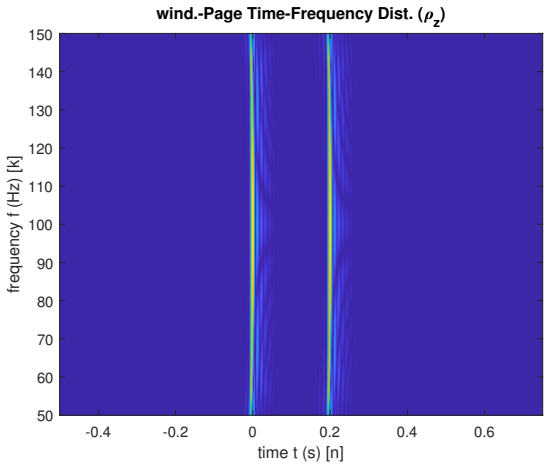


Figure 7.21: Windowed Page EWR distribution

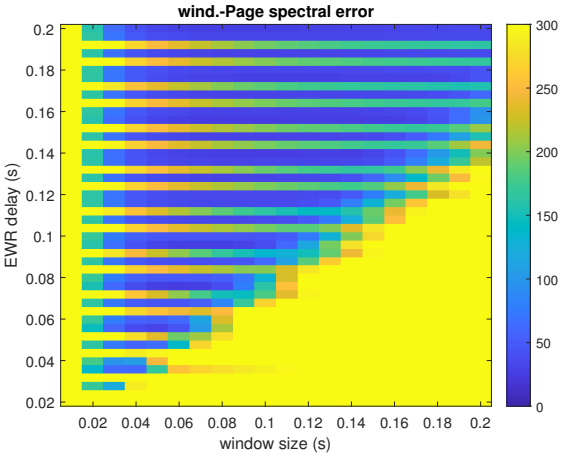


Figure 7.22: Windowed Page spectral error; TN filter

concentrated in the same time as the EWR component, unlike the Levin, which divides the cross-terms between the spectral and EWR components. Compare Figures 4.6 and Figures 4.7, observing the time axis for the off-zero lag components. Note also the artifacts appearing on the right sides of the components in the time-frequency distribution itself in Figure 7.21, hinting at that sidedness relative to the Levin in Figure 7.14. Spectral filters also treat the windowed Page like the windowed Levin, with higher errors at the window size extremities, except that the notch filters result in significantly higher errors across delay and window size, as shown in Figure 7.22. Separation score is largely unchanged regardless of spectral filter.

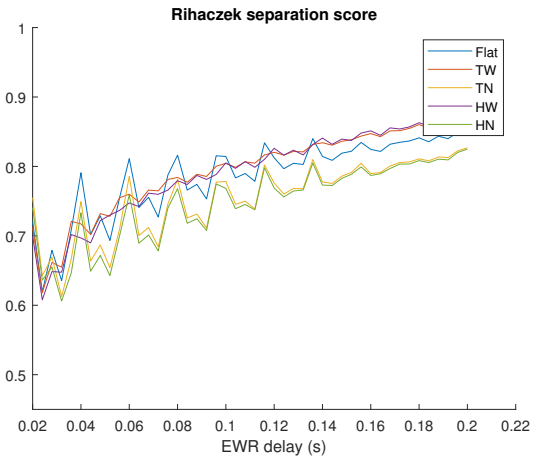


Figure 7.23: Rihaczek separation by EWR filter and delay

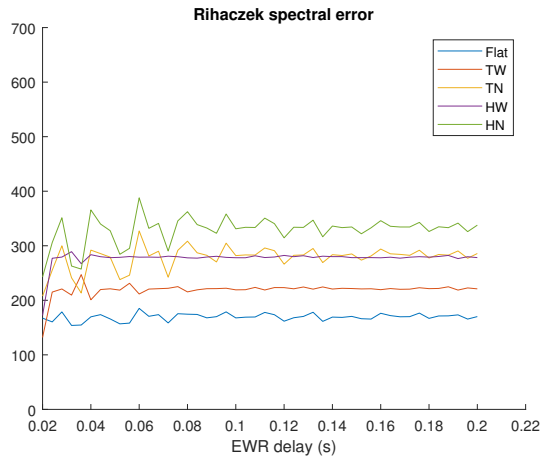


Figure 7.24: Rihaczek spectral error by EWR filter and delay

### 7.2.8 Rihaczek distribution

For the Rihaczek, the separation score is nearly identical to both that of the Levin and that of the Page (see Figures 7.12, 7.17, and 7.23); however, the Rihaczek performs the best of the three in regards to spectral error (see Figures 7.13, 7.18, and 7.24). Similar to the Levin, the Rihaczek places cross-terms concurrently with both the specular and EWR components (again leaving no cross-term between; see Figure 4.5), resulting in spectral errors—even though they are smaller errors than the other two.

### 7.2.9 Windowed Rihaczek distribution

As mentioned with the non-windowed Rihaczek, separation scores mirror those of the Levin and Page (see Figures 7.15, 7.19, and 7.25), but the Rihaczek's superiority in spectral error is clear in Figure 7.26 (see also Figures 7.16 and 7.20). Using any of the described spectral filters results in increased spectral error when the window size is greater than approximately twice the EWR delay. This is due to the fact that the window no longer prevents the occurrence of the cross-term artifact pattern along the frequency axis seen in Figure 4.9.

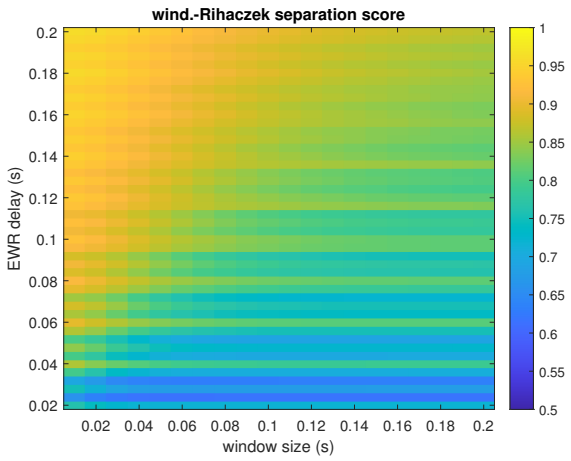


Figure 7.25: Windowed Rihaczek separation; no filter

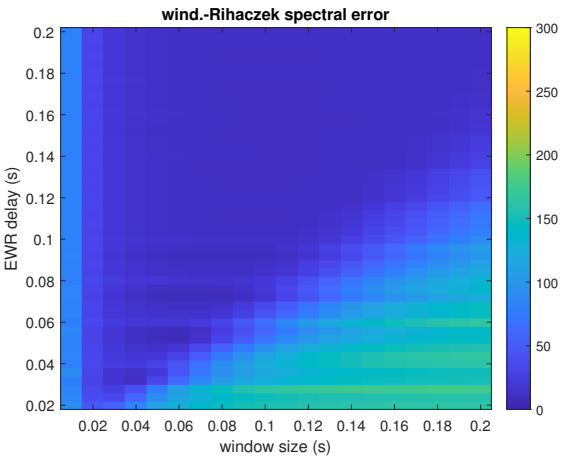


Figure 7.26: Windowed Rihaczek spectral error; no filter

### 7.2.10 B distribution

The B distribution is of a type different from the Levin, Page, and Rihaczek family from the previous sections. Two variables will still be examined, but window size will be replaced with the $\beta$ parameter described in Subsection 3.2.8. The B distribution has significant, early disqualification for EWR processing in its separation scores shown in Figure 7.27. Figure 7.29 shows the cross-term contributing to the poor separation scores. This is the nominal EWR processing case used before, and in this case $\beta = 0.1$. The authors recommend $\beta = 0.01$ [3], but this seems unsuitable for the EWR scenario at hand, as Figure 7.28 reveals that spectral errors become high across a wide range of EWR delays as $\beta$ approaches 0.01. The triangular and Hann window filters result in little change in spectral error when compared with no filtering. The notch filters do increase the error somewhat, especially in situations with short EWR delays (see Figure 7.30). Figure 7.31 shows the distortion from the B distribution resulting in the poor spectral error scores for the triangular notch filter. The EWR delay is set to 0.1 s and $\beta = 0.1$.

### 7.2.11 Modified-B distribution

Modifying the B distribution as described in Subsection 3.2.9 provides no noticeable improvement for the application of revealing elastic wave reradiation. Compare Figures

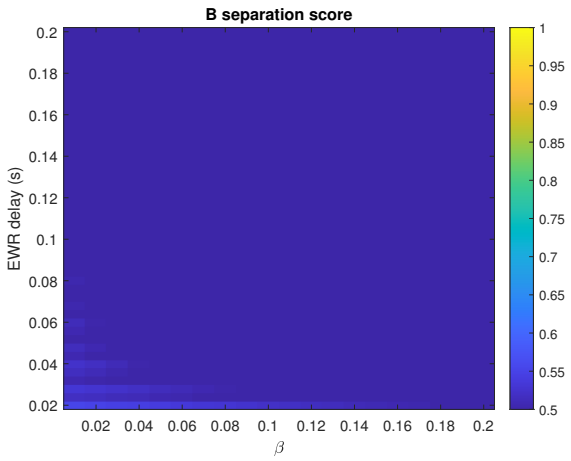


Figure 7.27: B separation; no filter

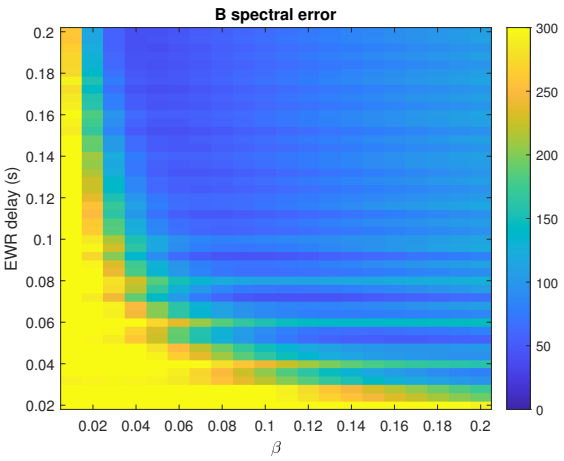


Figure 7.28: B spectral error; no filter

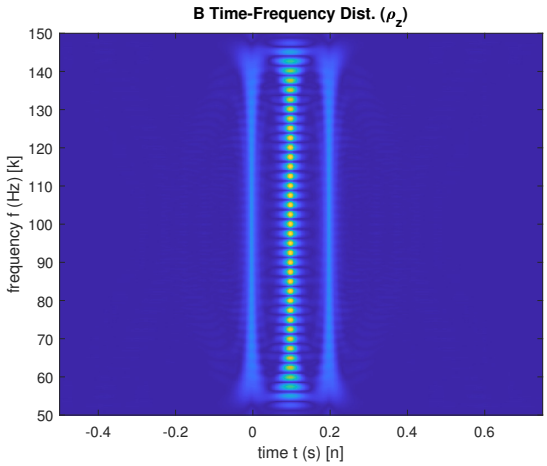


Figure 7.29: B EWR distribution

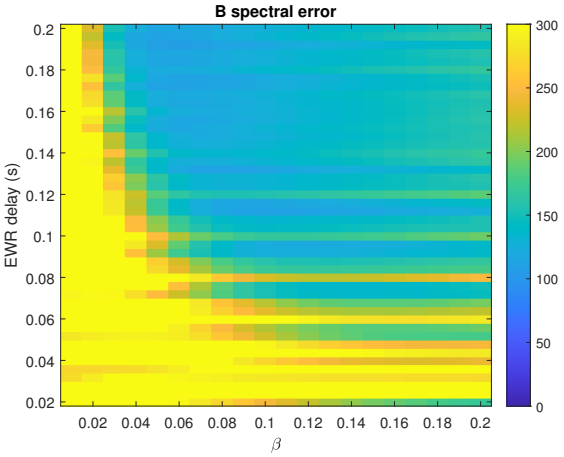


Figure 7.30: B spectral error; TN filter

7.27 and 7.28 with 7.32 and 7.33. There is no significant change in the cross-term or the appearance of the EWR example in the time-frequency space at all (see Figure 7.34). Note again that window size has been replaced as a variable by the $\beta$ parameter.

### 7.2.12 Choi-Williams distribution

The Choi-Williams distribution offers a promising turn in this search through time-frequency methods. While at first glance separation scores seem modest in Figure 7.35, the score does not fully capture the performance. Figure 7.37 reveals that the distribution spreads the energy remaining between the specular and elastic wave components quite evenly—significantly reducing any risk that the cross-term energy could result in false

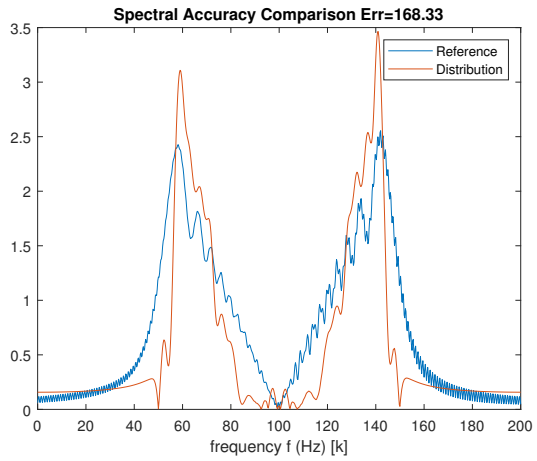


Figure 7.31: B EWR spectral accuracy; TN filter

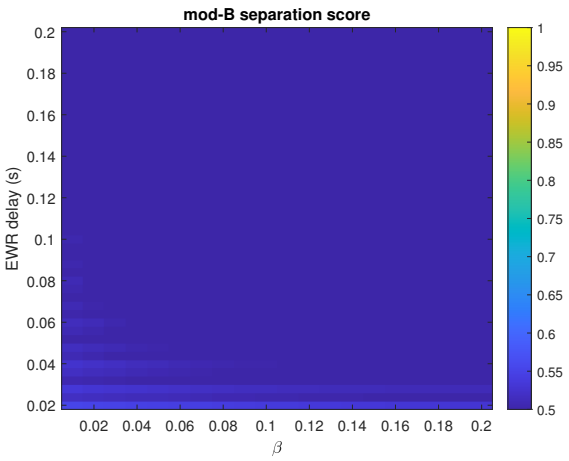


Figure 7.32: Modified B separation; no filter

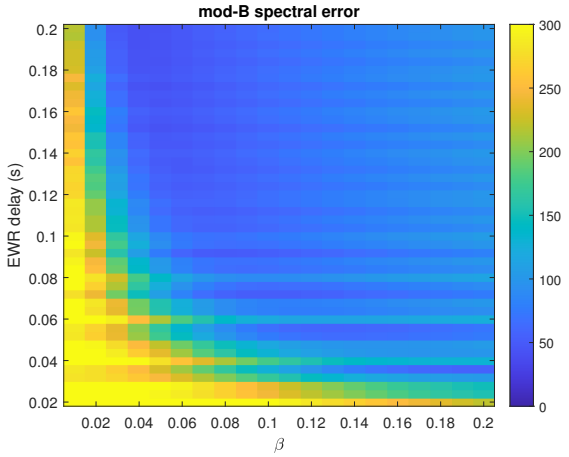


Figure 7.33: Modified B spectral error; no filter

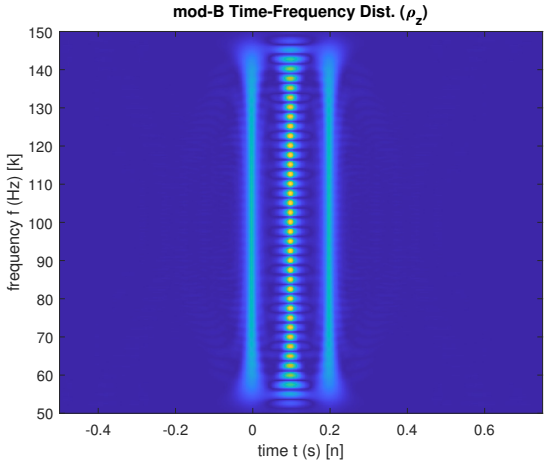


Figure 7.34: Modified B EWR distribution

elastic components. Figure 7.36 shows that not only is separation good, but the spectral error remains low across a range of delays and choices of $\sigma$, which takes the place of window size in the two-dimensional scoring representations. Applying the TW spectral filter has little impact on the separation score, but the spectral error still performs well (see Figure 7.38), faltering only when the time spacing between the components becomes small. The TN filter degrades performance further (see Figure 7.39), but this loss is not, perhaps, decisive. The HW and HN filters perform analogously to the TW and TN, respectively. Figure 7.40 shows the nature of the spectral error appearing when the TN filter is used with EWR delay set to 0.08 s and $\sigma$ to 0.12.

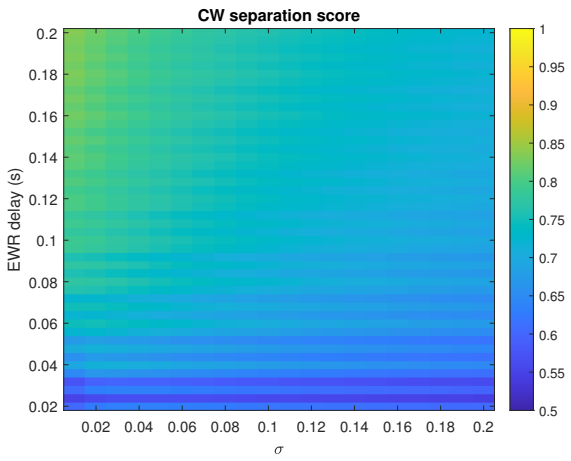


Figure 7.35: Choi-Williams separation; no filter

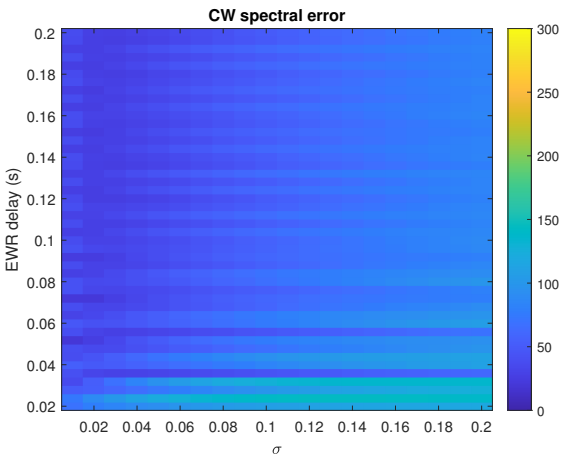


Figure 7.36: Choi-Williams spectral error; no filter

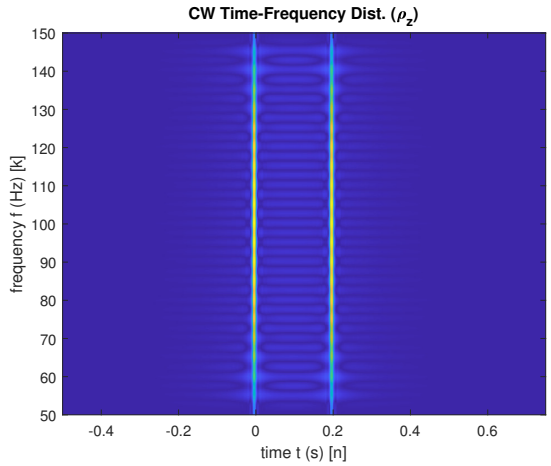


Figure 7.37: Choi-Williams EWR distribution

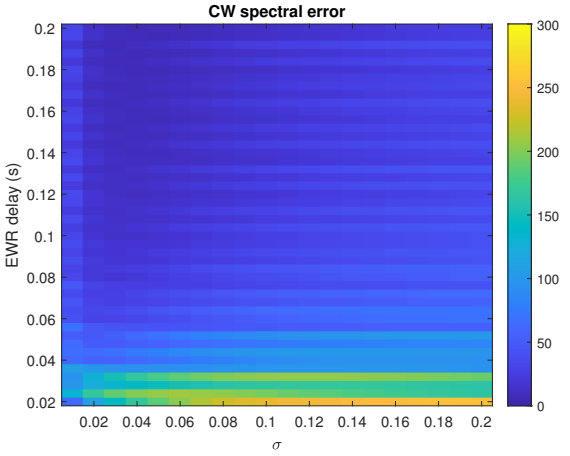


Figure 7.38: Choi-Williams spectral error; TW filter

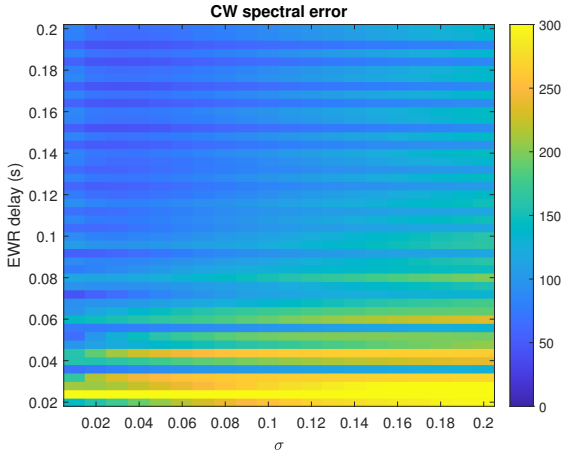


Figure 7.39: Choi-Williams spectral error; TN filter

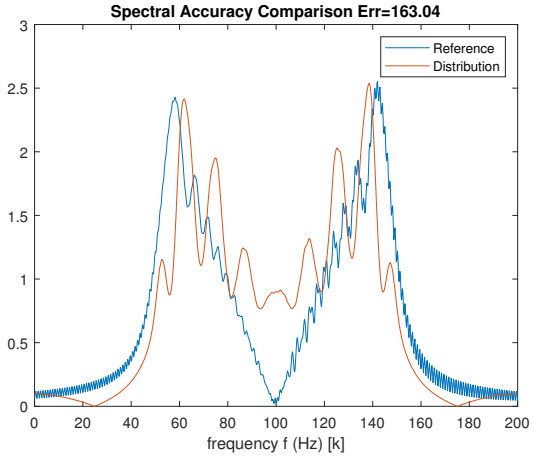


Figure 7.40: Choi-Williams EWR spectral accuracy; TN filter

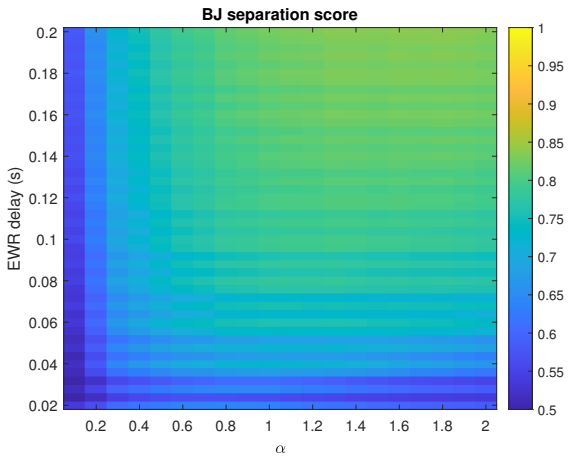


Figure 7.41: Born-Jordan separation; no filter

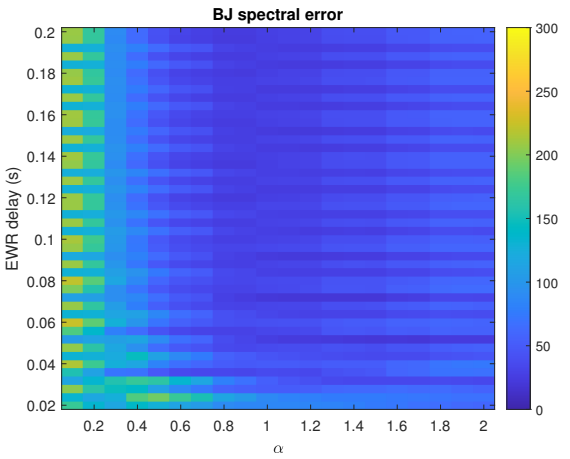


Figure 7.42: Born-Jordan spectral error; no filter

### 7.2.13 Born-Jordan distribution

Like the Choi-Williams, the Born-Jordan distribution is one which has fairly diffuse cross-term effects between the specular and EWR components, as shown in Figure 7.43. Again, the separation scores in Figure 7.41 do not seem to completely capture the benefit of this, since the focused cross-terms appearing halfway between the components in other distributions are far more likely to be misinterpreted in noisy data as additional acoustic components. The spectral error (see Figure 7.42) is perhaps not as impressive as the Choi-Williams, but it is still quite good, getting noticeably worse when $\alpha$ (which has become the horizontal axis variable) is small. The Born-Jordan performs well with the TW filter (Figure 7.44) but has much more trouble with the TN (Figure 7.45). Performance on components filtered by the HW or HN is comparable. The results suggest a choice of 1, or slightly below, for the $\alpha$ parameter, where exists the region of lowest error and which retains reasonable separation scores.

### 7.2.14 Zhao-Atlas-Marks distribution

The Zhao-Atlas-Marks distribution calls for less straightforward testing since it requires searching across three variables—EWR delay, window size $w$, and choice of parameter $a$. Holding the window size constant at 0.1 s to begin, a sweep of $a$ reveals two differing

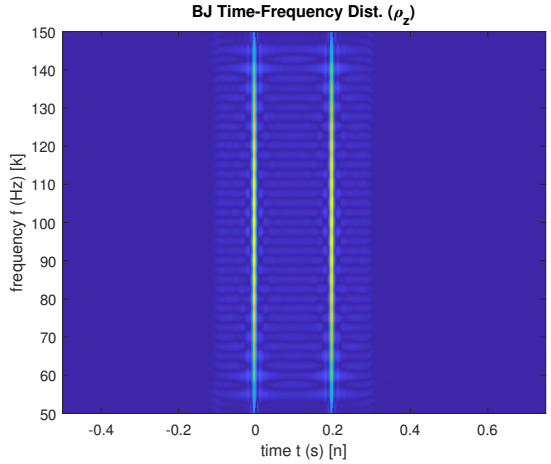


Figure 7.43: Born-Jordan EWR distribution

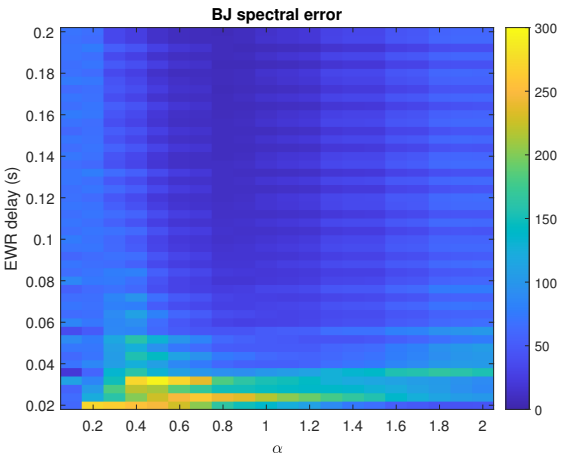


Figure 7.44: Born-Jordan spectral error; TW filter

performance regions with respect to EWR. When $a > 1$ (Figures 7.46 and 7.47), spectral error scores are generally poor, but separation is decent when the EWR delay exceeds 0.1 s. Performance under an EWR delay of 0.1 s is uniformly bad. The distribution fares better when $a < 1$. Separation is worse, but the spectral error is significantly reduced, making this likely preferable for EWR.

Here, two options will be compared: a low and a high option for $a$. Holding $a$ at 0.35, sweeping across window size produces Figures 7.50 and 7.51, and holding $a$ at 1, Figures 7.52 and 7.53 are produced. Lest these plots incline one to choose a particularly narrow window size, a brief look at Figures 7.54 and 7.55 reveal that the apparent advantage at $a < 0.01$ is a product of the simple spectrum under consideration. When the EWR component is filtered with the TN, it seems a better compromise to choose $w = 0.03$ s, trying to get both a low spectral error and as much in the way of separation as possible. And this is true for both $a = 0.35$ and $a = 1$. Examining Figures 7.56 and 7.57, the trade-off in choice of $a$ is made clearer. $a = 0.35$ provides a lower spectral error, and $a = 1$ produces better component separation. For comparison with the other distributions, Figures 7.58 and 7.59 gives an idea of what the distribution looks like with $w = 0.03$ s and with $a = 0.35$ and $a = 1$, respectively.

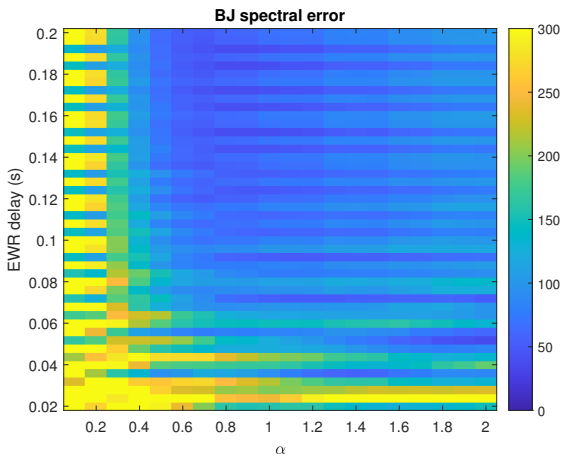


Figure 7.45: Born-Jordan spectral error; TN filter

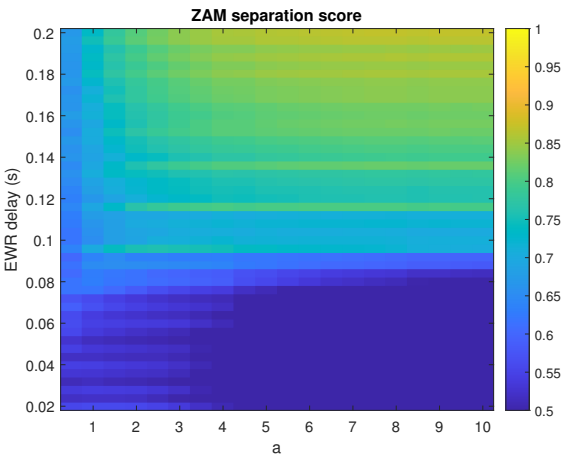


Figure 7.46: Zhao-Atlas-Marks separation; no filter; $a > 1$; $w = 0.1$

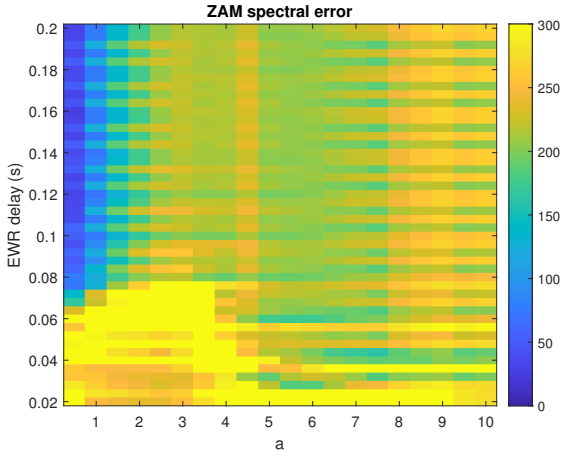


Figure 7.47: Zhao-Atlas-Marks spectral error; no filter; $a > 1$; $w = 0.1$

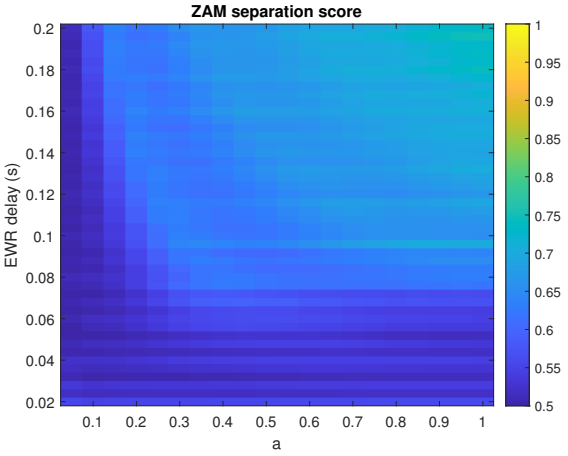


Figure 7.48: Zhao-Atlas-Marks separation; no filter; $a < 1$; $w = 0.1$

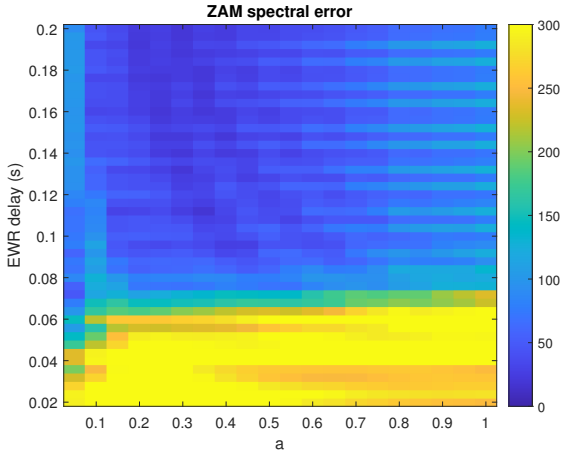


Figure 7.49: Zhao-Atlas-Marks spectral error; no filter; $a < 1$; $w = 0.1$

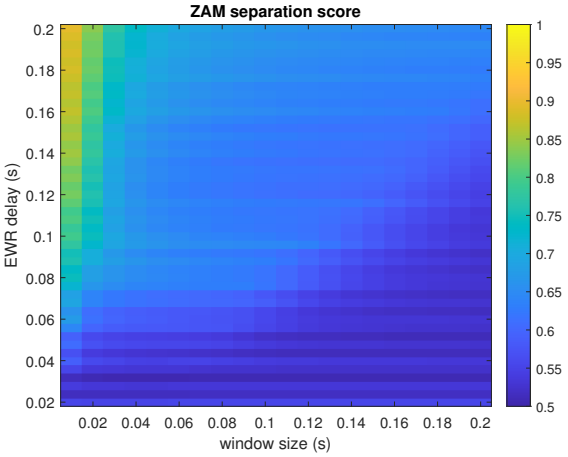


Figure 7.50: Zhao-Atlas-Marks separation; no filter; $a = 0.35$

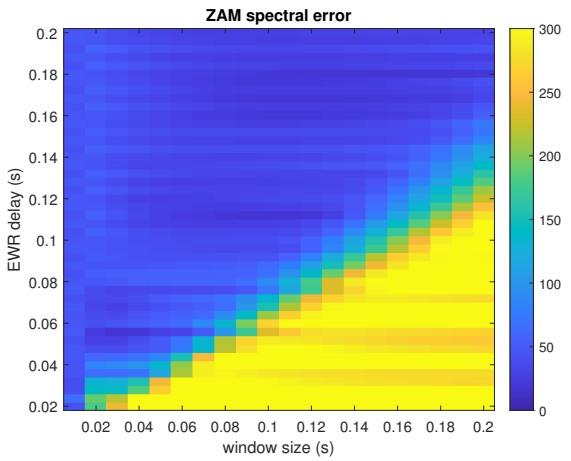


Figure 7.51: Zhao-Atlas-Marks spectral error; no filter; $a = 0.35$

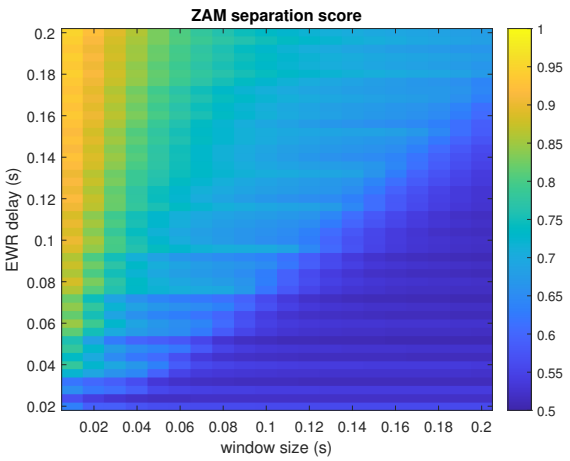


Figure 7.52: Zhao-Atlas-Marks separation; no filter; $a = 1$

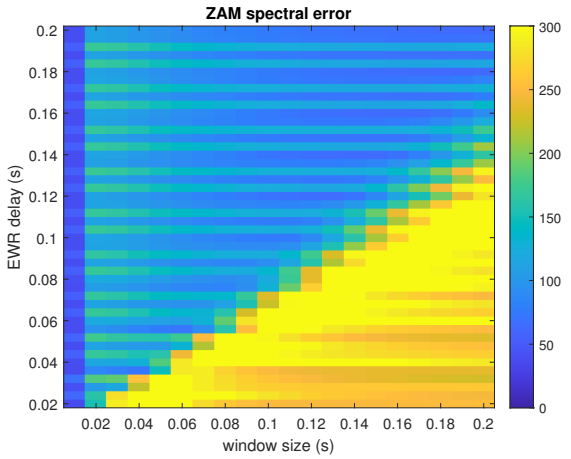


Figure 7.53: Zhao-Atlas-Marks spectral error; no filter; $a = 1$

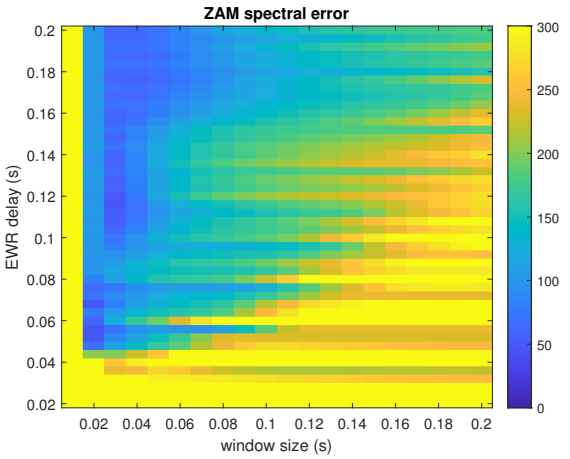


Figure 7.54: Zhao-Atlas-Marks spectral error; TN filter; $a = 0.35$

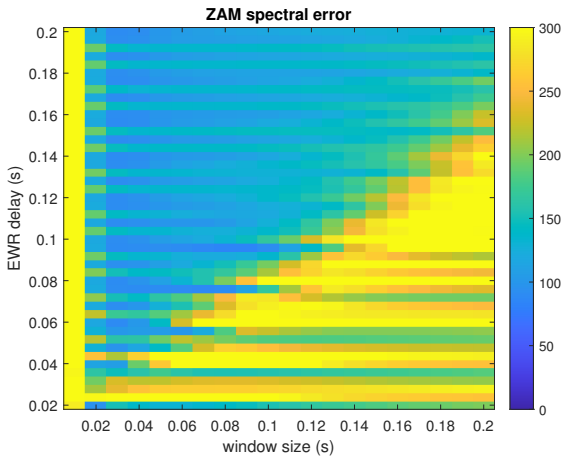


Figure 7.55: Zhao-Atlas-Marks spectral error; TN filter; $a = 1$

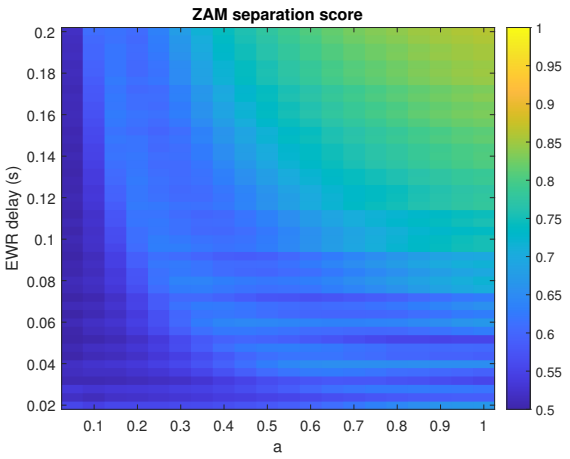


Figure 7.56: Zhao-Atlas-Marks separation; TN filter; $w = 0.03$

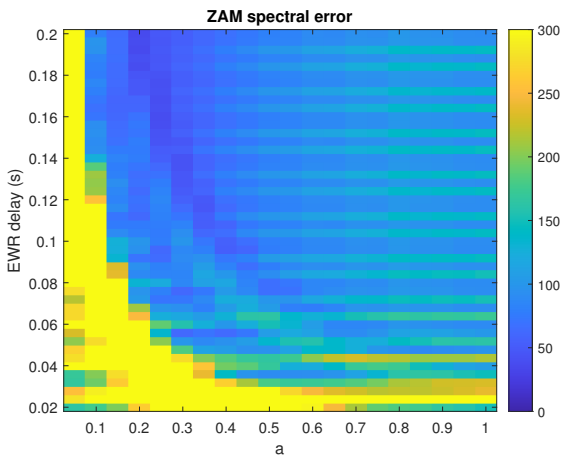


Figure 7.57: Zhao-Atlas-Marks spectral error; TN filter; $w = 0.03$

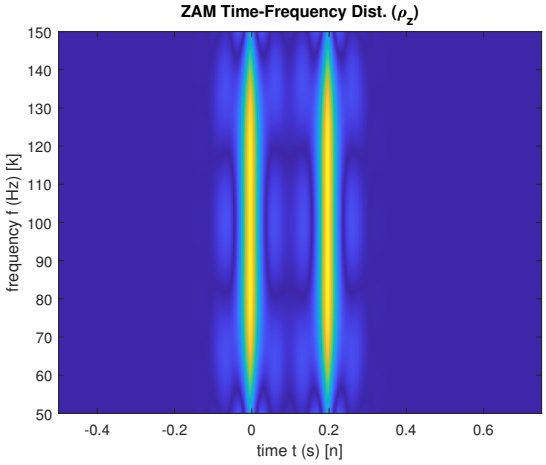


Figure 7.58: Zhao-Atlas-Marks EWR distribution; $a = 0.35$; $w = 0.03$

### 7.2.15 Proposed distribution

Now the performance of the time-frequency distribution proposed in Chapter 4 will be examined. Since the spectral fidelity of the EWR component is of such importance in this application, it becomes clear why the proposed distribution was designed to move cross-term influence away from it, at the acceptable cost of corrupting the specular component. It will be noted that this isolation works well in the case of one specular and one EWR component but not so, perhaps, when multiple EWR returns are arriving consecutively. Indeed, perfect cross-term isolation will not be possible as an EWR component will be corrupted by any additional component which happens to follow it.

Figure 7.60 shows that the proposed distribution makes no improvement over the similar distributions—Page, Rihaczek, Levin—as expected. These all succeed in removing the cross-term from between the specular and EWR components. The real advantage is revealed in the reduced spectral errors in Figure 7.61. The distribution applied to the example pulses has already been shown in Figure 4.12, but an example of the accuracy achieved with the TN spectral filter, which has been a challenge for most distributions, can be seen in Figure 7.62.

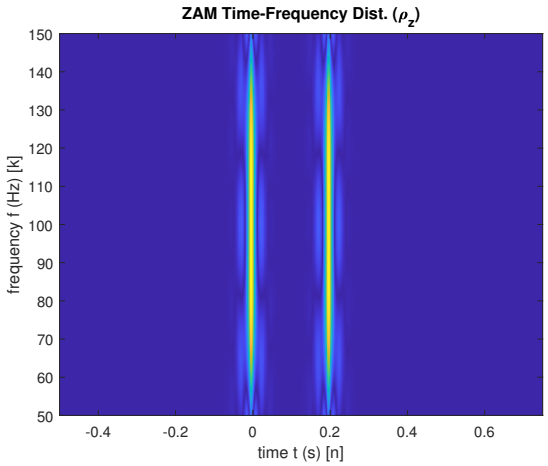


Figure 7.59: Zhao-Atlas-Marks EWR distribution; $a = 1$; $w = 0.03$

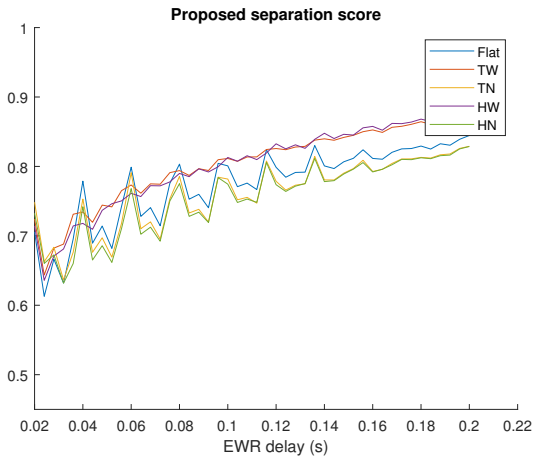


Figure 7.60: Proposed separation by EWR filter and delay

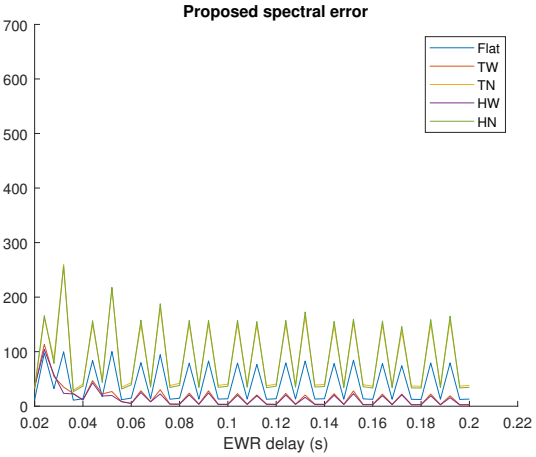


Figure 7.61: Proposed spectral error by EWR filter and delay

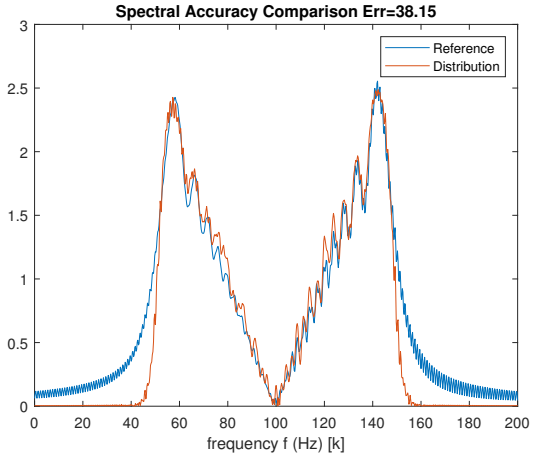


Figure 7.62: Proposed EWR spectral accuracy; TN filter

## 7.3 Multiple EWR components

A last element of the simulation which is necessary for completeness is the addition of multiple EWR components. This will be accomplished by having one specular echo followed two EWR echos at even spacing, providing the greatest opportunity for the first and last components to interfere with the spectral accuracy of the one in the center. All components will have the same amplitude, and when a spectral filter is applied, it will be applied to both of the EWR returns. The spectral errors are recorded in Table 7.1.

Table 7.1: Multiple EWR Spectral Errors

| TF representation | No filter | TW | TN | HW | HN | Parameters |
|---|---|---|---|---|---|---|
| Spectrogram | 60.1 | 22.5 | 55.7 | 17.0 | 42.1 | $w = 0.06\,\mathrm{s}$ |
| Wigner-Ville | 419.1 | 228.7 | 593.2 | 225.1 | 629.2 | |
| Windowed Wigner-Ville | 115.5 | 42.5 | 276.0 | 41.4 | 266.3 | $w = 0.06\,\mathrm{s}$ |
| Levin | 286.6 | 288.3 | 335.1 | 312.7 | 356.1 | |
| Windowed Levin | 12.2 | 2.7 | 32.3 | 2.5 | 28.6 | $w = 0.06\,\mathrm{s}$ |
| Page | 286.6 | 347.7 | 413.7 | 410.3 | 471.0 | |
| Windowed Page | 12.2 | 2.8 | 31.4 | 2.8 | 28.0 | $w = 0.06\,\mathrm{s}$ |
| Rihaczek | 286.6 | 273.0 | 329.0 | 323.6 | 375.3 | |
| Windowed Rihaczek | 12.2 | 2.7 | 32.3 | 2.5 | 28.6 | $w = 0.06\,\mathrm{s}$ |
| B | 239.3 | 182.7 | 305.7 | 184.8 | 299.7 | $\beta = 0.1$ |
| Modified-B | 333.2 | 220.9 | 333.8 | 230.5 | 336.9 | $\beta = 0.1$ |
| Choi-Williams | 32.2 | 13.4 | 78.9 | 16.2 | 76.5 | $\sigma = 0.04$ |
| Born-Jordan | 30.7 | 19.0 | 77.7 | 24.0 | 76.2 | $\alpha = 1$ |
| Zhao-Atlas-Marks | 39.6 | 31.2 | 61.7 | 22.3 | 67.7 | $w = 0.03\,\mathrm{s},\ a = 0.35$ |
| Zhao-Atlas-Marks | 109.0 | 101.5 | 91.6 | 99.1 | 102.4 | $w = 0.03\,\mathrm{s},\ a = 1$ |
| Proposed | 286.6 | 276.4 | 306.0 | 276.3 | 304.1 | |
| Windowed Proposed | 12.2 | 2.7 | 33.0 | 2.3 | 29.0 | $w = 0.06\,\mathrm{s}$ |

By far the best-performing distributions are the windowed versions of the Levin, Page, Rihaczek, and proposed distributions. The spectral accuracy in this family is unsurpassed, but they must have separation in time from the other components or the cross-terms cause errors to skyrocket. Windowing succeeds here, except that, depending on the object size and sonar frequencies involved, the spacing between the components could be quite narrow. Assuming that windowing solves part of the problem, the remainder could be mitigated by using in parallel the counterpart distributions of the Page and the one proposed. A comparison of the representations which shift cross-terms in opposite directions may allow unraveling artifact interactions when the window happens not to be small enough to separate components. Interestingly, even the windowing is not sufficient to save the accuracy of the Wigner-Ville distribution, and neither of the B distributions is competitive in this metric. In the middle are the spectrogram, and the Choi-Williams, Born-Jordan, and Zhao-Atlas-Marks distributions, which perform acceptably. The earlier observation about $a = 0.35$ performing better in terms of accuracy than $a = 1$ for the Zhao-Atlas-Marks is borne out by this test.

Table 7.2: Time-frequency SNR

| TF representation | SNR (dB) | Parameters |
|---|---|---|
| Spectrogram | 34.45 | $w = 0.06\,\mathrm{s}$ |
| Wigner-Ville | 16.93 | |
| Levin | 23.16 | |
| Page | 23.82 | |
| Rihaczek | 22.05 | |
| B | 10.28 | $\beta = 0.1$ |
| Modified-B | 15.81 | $\beta = 0.1$ |
| Choi-Williams | 33.39 | $\sigma = 0.04$ |
| Born-Jordan | 33.43 | $\alpha = 1$ |
| Zhao-Atlas-Marks | 29.50 | $w = 0.03\,\mathrm{s},\ a = 0.35$ |
| Zhao-Atlas-Marks | 32.77 | $w = 0.03\,\mathrm{s},\ a = 1$ |
| Proposed | 18.50 | |

## 7.4 Signal-to-noise ratio

Using Equation 6.6, signal-to-noise ratios are given for each of the above time-frequency representations using additive white Gaussian noise. The region of interest will surround only the EWR component with a tight boundary, excluding the specular return and any cross-terms not coincident with the EWR. One thousand trials of random noise for each distribution will be used to estimate the expected value of the noise power. Results appear in Table 7.2. Important for understanding this table is that cross-term energy appearing inside the region will be counted as signal energy, while it may be argued this is not necessarily part of the signal of interest. On the other hand, when considering SNR, the pertinent question is whether one is able to discern the presence of the EWR component against the background of noise at all. To this end any signal energy, cross-term or not, within this highly restricted area is helpful.

Based on the results, there are three broad categories. First are the B, modified-B, and Wigner-Ville distributions, which have the lowest SNRs of the lot. Taking also the cross-terms present in each of them, the poor SNRs make a convincing case that they are not appropriate for the sonar EWR application. The second category includes the group having a related set of kernels and middling SNR performance—the Levin, Page, Rihaczek, and the proposed distribution. The SNR deficiency of the proposed distribution

compared to its sisters is likely due to the design choice to redirect the cross-term from alignment with the EWR component, so then this loss is the cost of the spectral accuracy gains. While these representations have good resolution along the time axis, they may not be the best choice for revealing the signal in the presence of considerable noise. The collected data investigated in Chapter 8 was generated under controlled circumstances in an acoustic tank, so at least in that situation, noise is not much of a concern. The last group performs the best in the SNR category. This includes the spectrogram, Choi-Williams, Born-Jordan, and Zhao-Atlas-Marks distributions.

## 7.5 Conclusions

The next chapter examines the application of time-frequency representations to a set of collected acoustic data. A common theme is that the choice of window size should be on the order of the width of the pulse-compressed signal's main lobe—a fairly intuitive finding, which will be applied in processing of the sonar tank data. The foregoing simulations will serve as a test for weeding out representations not worth further investigation for the elastic wave reradiation application. Those ruled out include:

1. Wigner-Ville — The Wigner-Ville has fairly significant cross-term artifacts, resulting in a poor separation score. Spectral errors are high, except with TW or HW spectral filters. Neither SNR or multiple EWR error levels provide any compelling counter-argument.

2. Windowed Wigner-Ville — Windowing the Wigner-Ville helps with separation, of course, but accuracy issues remain, and there are better options.

3. Levin, Page, Rihaczek, proposed — These distributions, in their un-windowed forms, simply have too much of a problem with multiple EWR error. If one is going to apply these at all for EWR, one may as well exercise control over a windowing function.

4. B, modified-B — These are perhaps the most ill-suited for the given application. As discussed above, the cross-terms lead to poor separation scores, and neither the SNR nor the multiple EWR errors prove redemptive.

5. Windowed Levin, windowed Page, windowed Rihaczek — These will be eliminated simply because of their close similarity to the windowed proposed distribution and because it does not seem necessary to send another from this family of distributions.

By process of elimination, the performance of the following will be further analyzed in Chapter 8:

1. Spectrogram — The spectrogram serves as a good baseline for comparison, particularly since it does not suffer from cross-term issues.

2. Choi-Williams, Born-Jordan, Zhao-Atlas-Marks — These are grouped due to their very similar performance. They have some of the highest SNRs of the bunch and have respectable multiple EWR error scores. Additionally, these distributions solve the problem of cross-terms by dispersing the energy rather than focusing the cross-terms exactly halfway between components. Windowed distributions, including the spectrogram, can achieve very high separation scores of around 0.9, where the Choi-Williams and Born-Jordan do not. Subjectively, however, the latter do apparently well at separation because of their diffuse cross-terms and sidelobes (See again Figures 7.37 and 7.43). It seems sufficient energy is present to suppress their separation scores, but the benefit of the diffuse energy is not captured in the metric, as the diffuse energy is more easily ignored than the focused cross-term of the Wigner-Ville distribution.

3. Windowed proposed — This maintains the advantages of others in its family but with the added benefit of deflecting cross-terms toward the specular rather than the EWR components. This latter property works hand-in-hand with the windowing to ensure that, even if the window captures more than one component at a time, the cross-terms are relatively controlled and shift in a preferable direction.

# Chapter 8

# Acoustic tank data

This data set was collected in a tank in the Acoustics Test Facility at the Naval Undersea Warfare Center (NUWC) in Newport, RI in August of 2012. It involved active sonar recordings of three different 4 in.-diameter, 1 m-long air-filled cylinders with endcaps. The geometries were identical, save minor variations in the endcaps, while the three different materials were steel, aluminum, and PVC . Data was collected at incident angles $\theta$ of 0°, 15°, 30°, 45°, 60°, and 90°, where 0° indicates that the transmitted waveform is directly incident upon the endcap and 90° that the incidence is broadside to the cylinder. The intent was to demonstrate variation in the acoustic responses of materials with different elasticities. The three have quite different Young's moduli of elasticity: $\approx 200$ GPa for steel, 70 GPa for aluminum, and $< 5$ GPa for PVC. With the same shell thickness in each, the differences will be carried forward into the respective bending stiffnesses. Six incident angles, five transmitted signal bandwidths, and three acoustic targets make up the data set, creating a total of 150 individual recorded transmissions. Figures 8.1-8.3 show the cylinders used during the data collection.

## 8.1 Transmitted waveforms

This data set used five non-standard wide-band waveforms with the frequency characteristics detailed in Table 8.1. Figure 8.4 shows the nature of these signals in the time domain. Figure 8.7 provides the frequency domain, and Figures 8.5, 8.6, 8.8, 8.9, and 8.11 provide the spectrogram time-frequency representations. In the latter figures it is apparent that there is no simple structure underlying the time-frequency design of the

Figure 8.1: Steel cylinder used in acoustic tank experiments

Table 8.1: Transmitted waveform frequency characteristics

| Center frequency (kHz) | Frequency span (kHz) | Bandwidth (kHz) |
|---|---|---|
| 20 | 5 – 35 | 30 |
| 50 | 20 – 80 | 60 |
| 65 | 35 – 95 | 60 |
| 85 | 55 – 115 | 60 |
| 120 | 90 – 150 | 60 |

signal. The waveform does not have a constant amplitude, nor does it have well-defined boundaries at the limits of its bandwidth. Figure 8.10 shows the autocorrelation of these waveforms to provide insight into the time resolution of the signal as a sonar transmission. The recorded data is purely real, and for the purposes of this analysis, the Hilbert transform is used to generate corresponding imaginary data to form a complex analytic signal. For brevity, the waveforms will be referred to by their center frequencies.

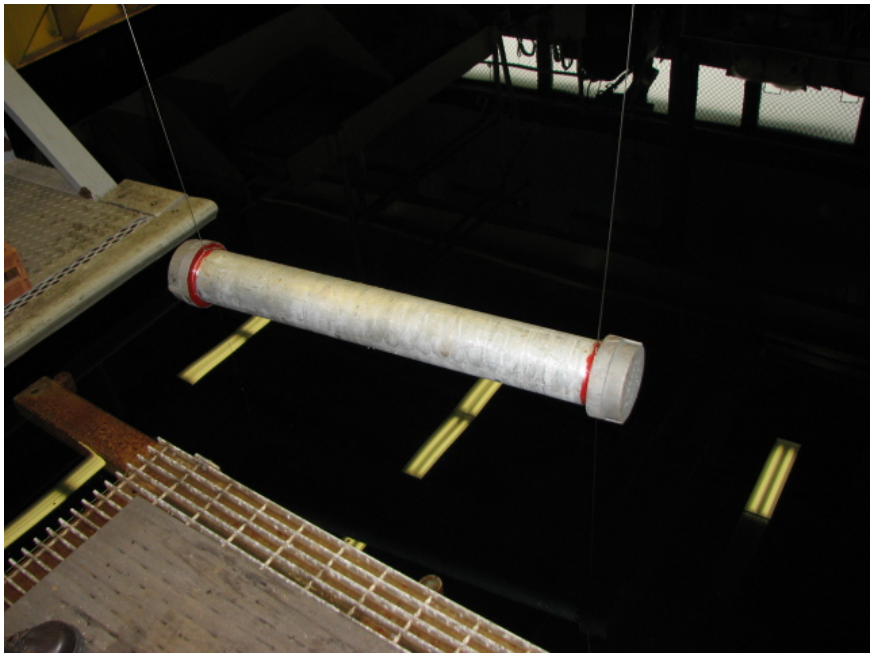

Figure 8.2: Aluminum cylinder used in acoustic tank experiments

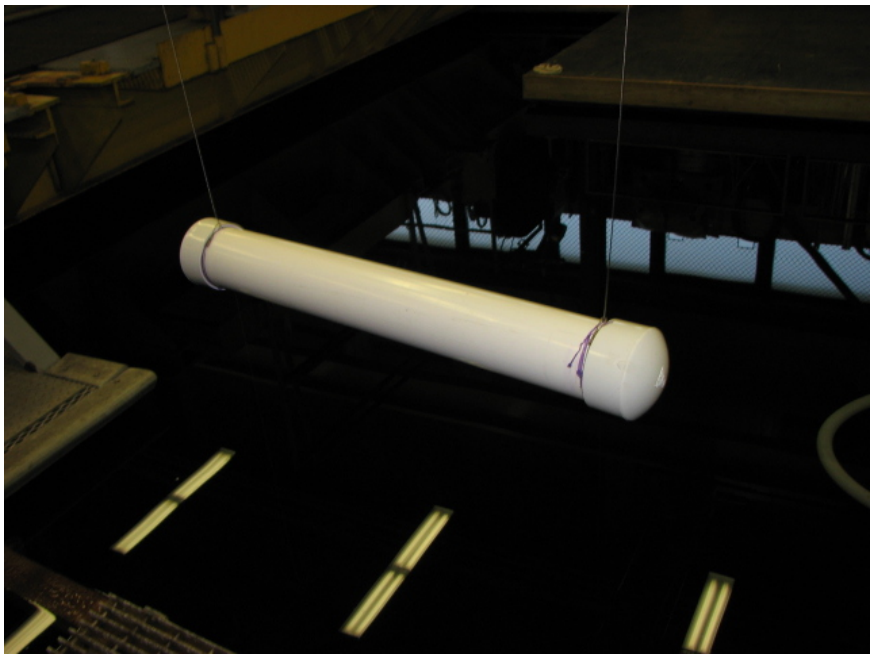

Figure 8.3: PVC cylinder used in acoustic tank experiments

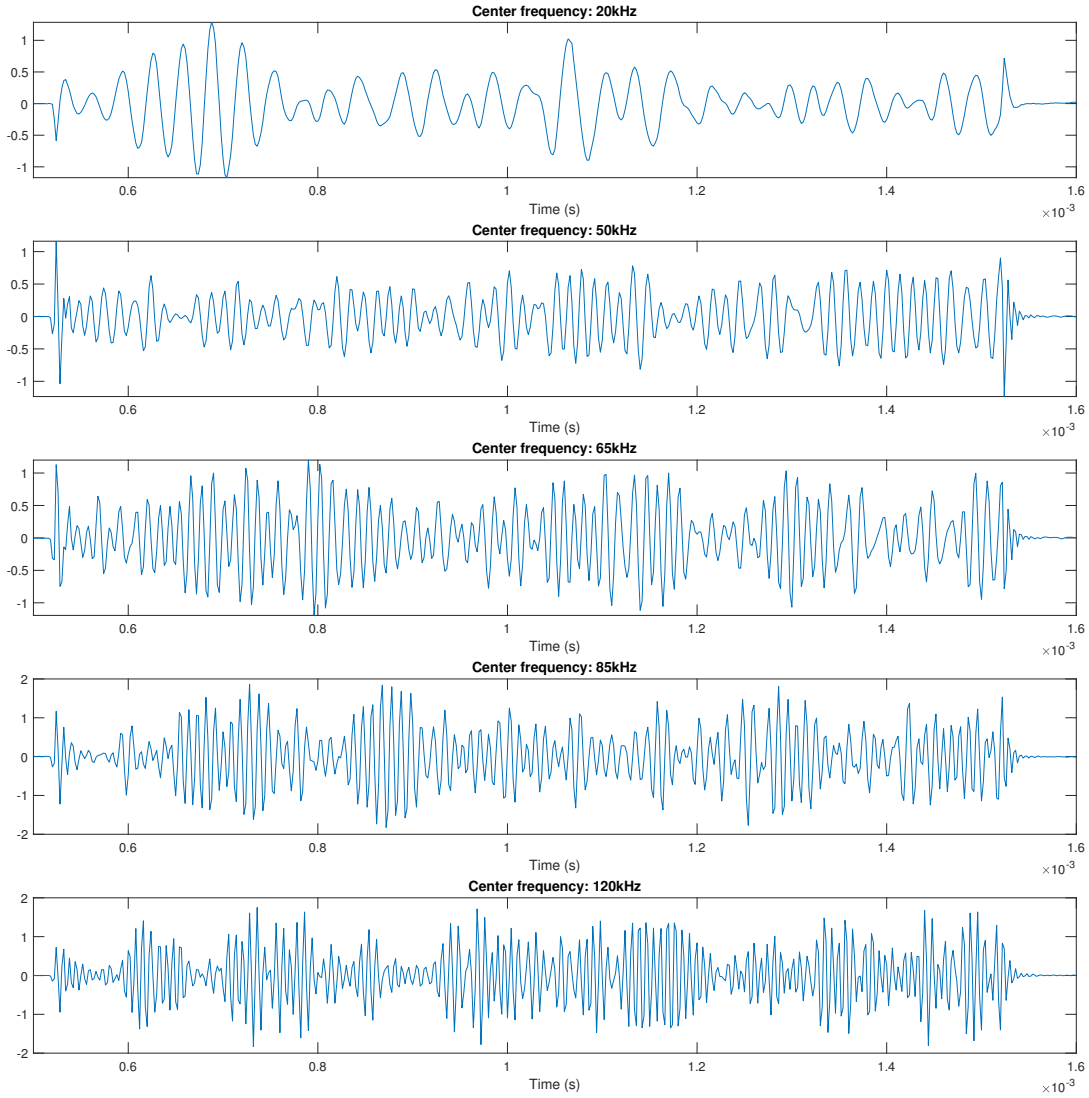


Figure 8.4: Tank data transmitted waveforms shown in the time domain

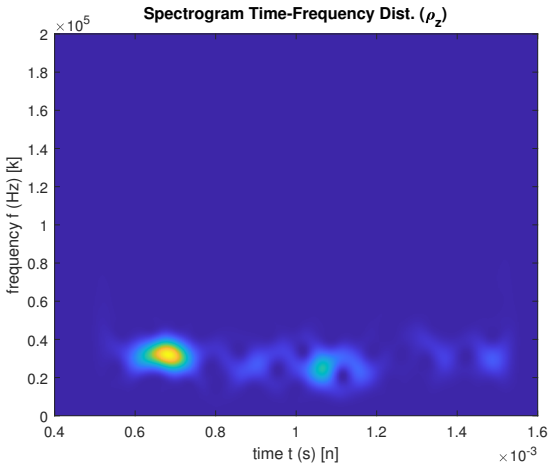


Figure 8.5: Spectrogram of tank transmit waveform centered at 20 kHz

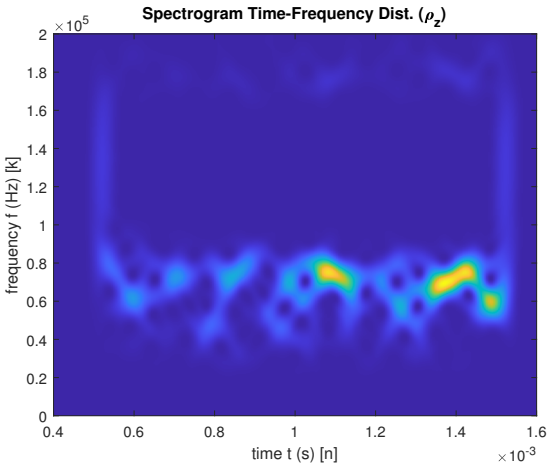


Figure 8.6: Spectrogram of tank transmit waveform centered at 50 kHz

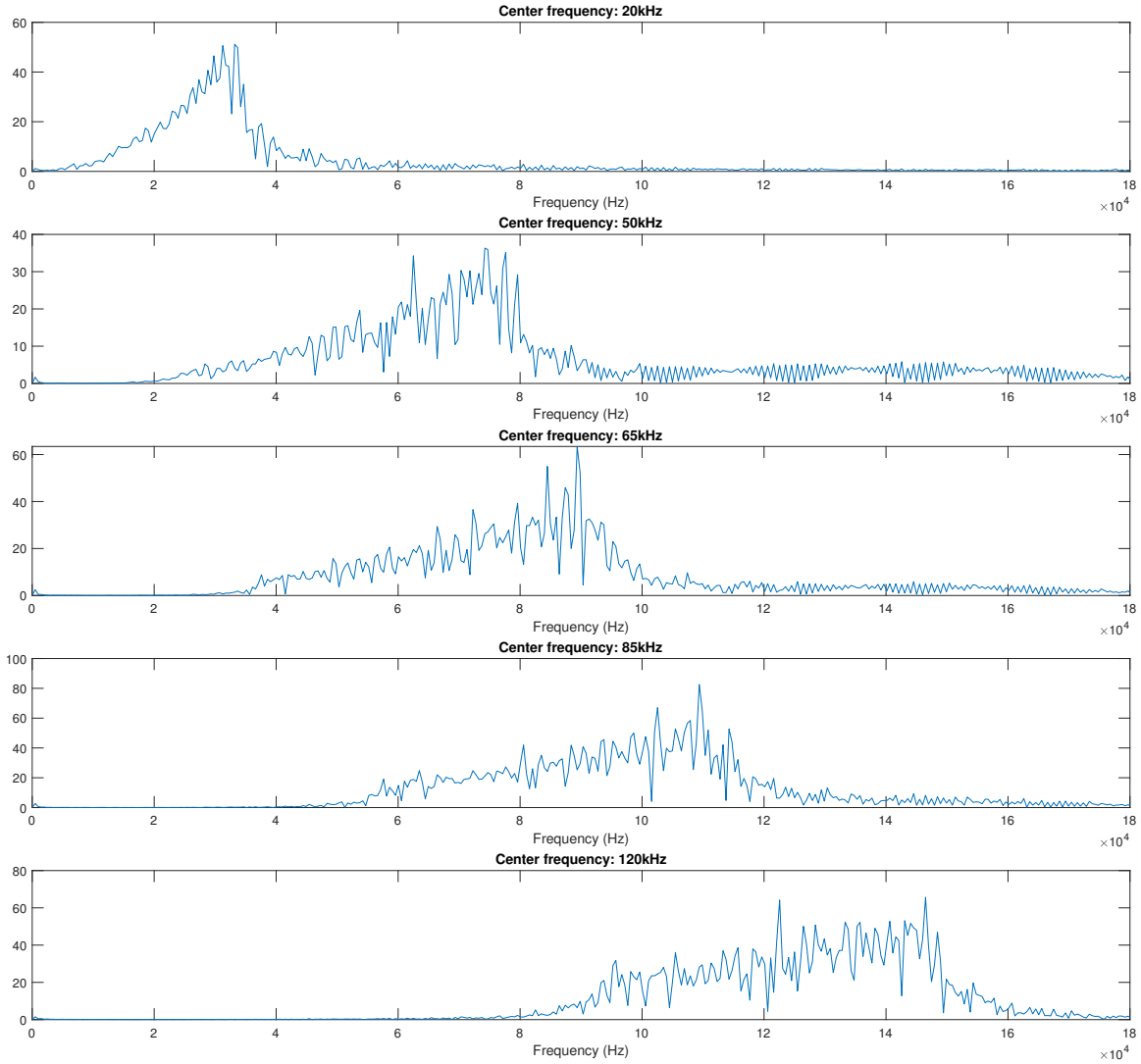


Figure 8.7: Tank data transmitted waveforms shown in the frequency domain

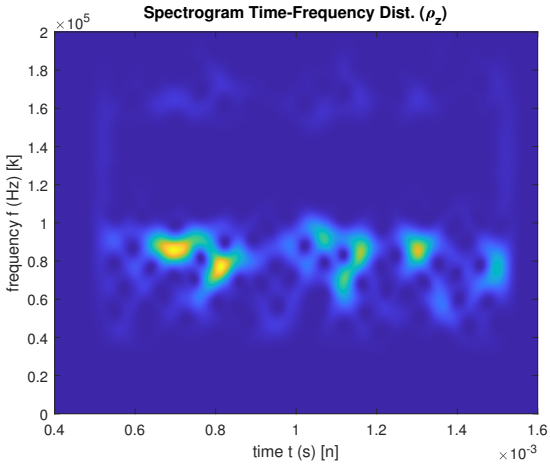


Figure 8.8: Spectrogram of tank transmit waveform centered at 65 kHz

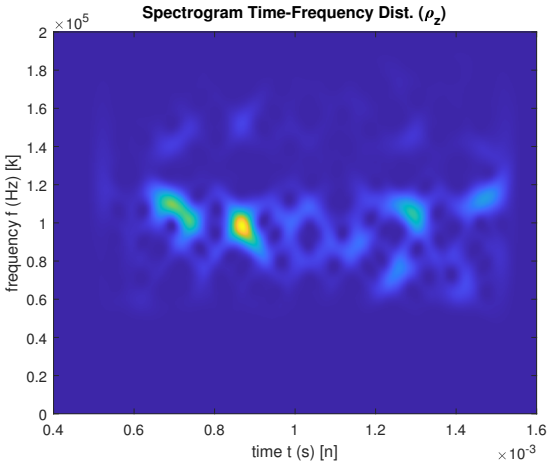


Figure 8.9: Spectrogram of tank transmit waveform centered at 85 kHz

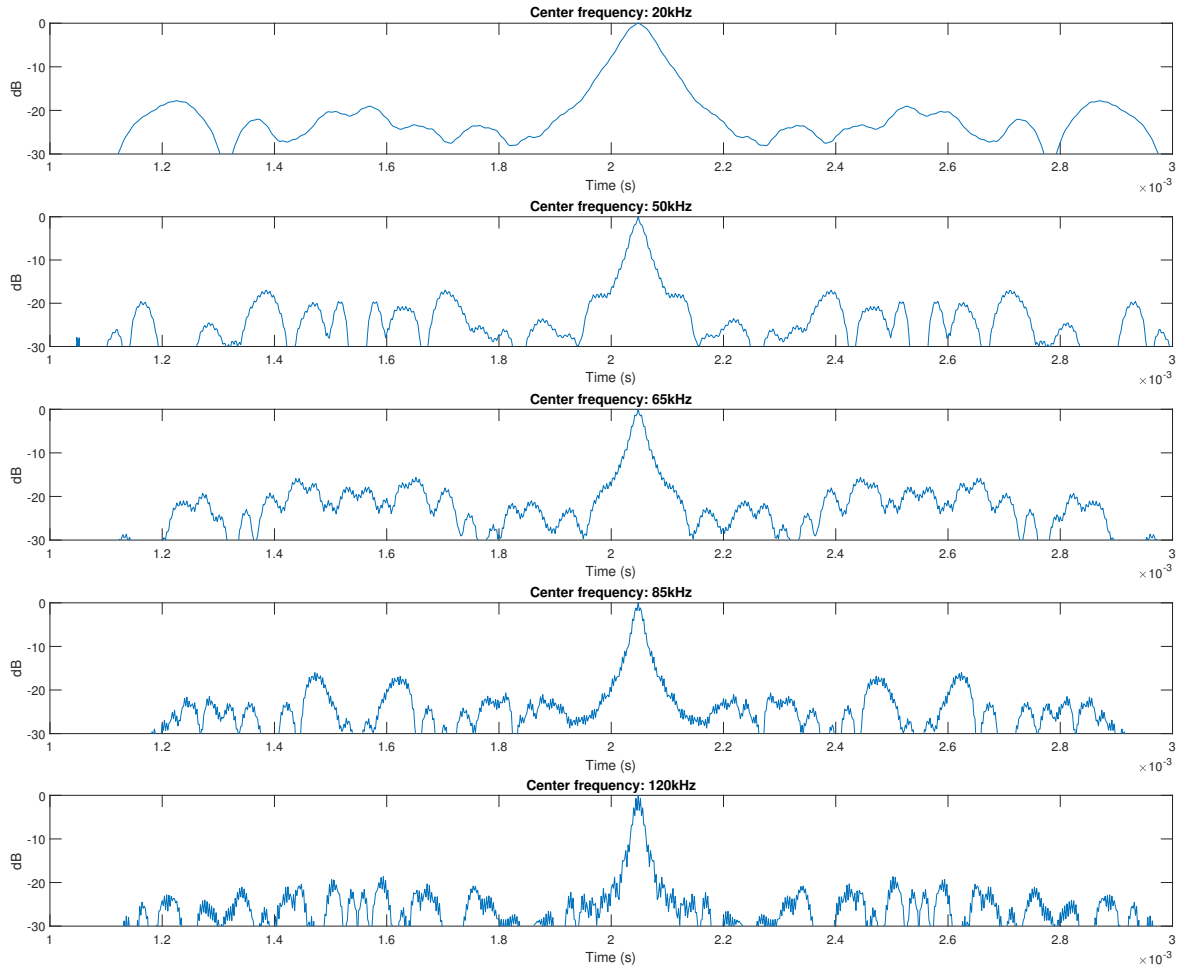


Figure 8.10: Tank data transmitted waveform autocorrelations in dB

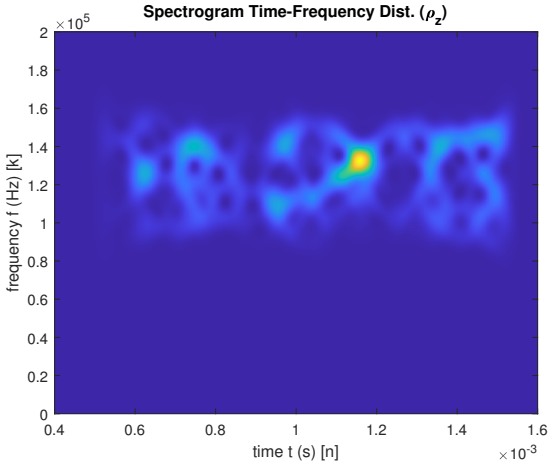


Figure 8.11: Spectrogram of tank transmit waveform centered at 120 kHz

## 8.2 Methodology

The purpose of investigating this data is to examine whether an acoustic reflector's material composition alone may be enough to differentiate it from a similarly-shaped reflector, whether the theory on elastic wave reradiation is consistent with experimental observation, and whether appropriate time-frequency representations are sufficient to enable such differentiation. Unlike the foregoing simulations, there is no *a priori* knowledge of the reflected and reradiated signals, so a determination of representation accuracy similar to that used with the simulation data previously is not possible. This additionally means that tuning of the distribution parameters cannot be done as previously. The choice of values based upon the simulation will be carried forward into the tank data processing—namely, $\sigma = 0.04$ for Choi-Williams, $\alpha = 1$ for Born-Jordan, and $a = 1$ for Zhao-Atlas-Marks. The latter is selected over $a = 0.35$ based on the need for better temporal separation between components and is further explained in Subsection 8.3.1. The assumptions for this approach are two: first, that choice of parameter is not overly sensitive and being close to an "optimized" value is sufficient; and second, that having the autocorrelation main lobe widths and the distribution kernel dimensions remain comparatively proportional for the tank data as they were in the simulation is enough to produce similar performance. Window sizes for this analysis will be on the order of the autocorrelation main lobe widths (see Figure 8.10). This means a width of 250 µs for the spectrogram and the proposed distribution and 125 µs for the Zhao-Atlas-Marks distribution.

## 8.3 Observations

To begin, a representative sonar echo from the data set is selected to provide a general sense of the performance of the different distributions. That echo will be shown in each of the five distributions for comparison. First, the time series is shown in Figure 8.12. Figures 8.13—8.17 show the corresponding TF distributions.

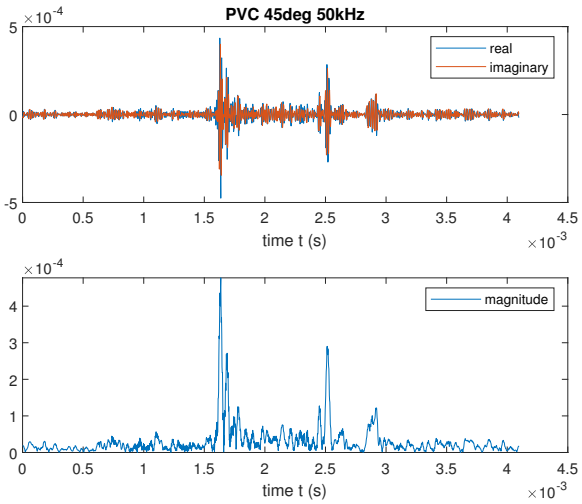


Figure 8.12: Time series, PVC, 45°, 50 kHz center frequency

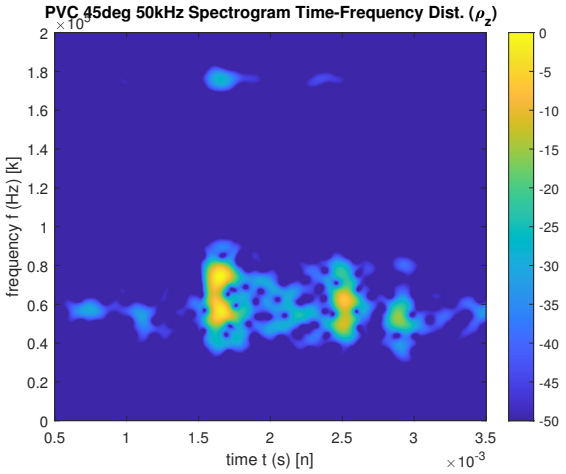


Figure 8.13: Spectrogram (dB), PVC, 45°, 50 kHz center frequency

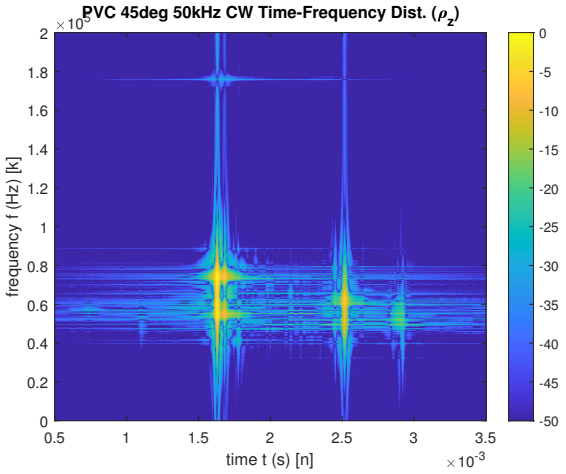


Figure 8.14: Choi-Williams TF dist. (dB), PVC, 45°, 50 kHz center frequency

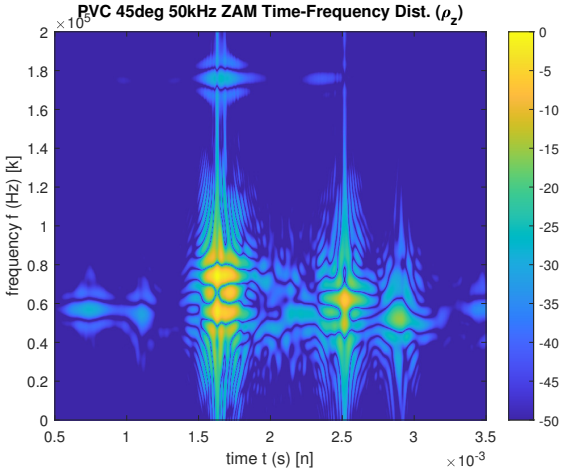


Figure 8.15: Zhao-Atlas-Marks TF dist. (dB), PVC, 45°, 50 kHz center frequency

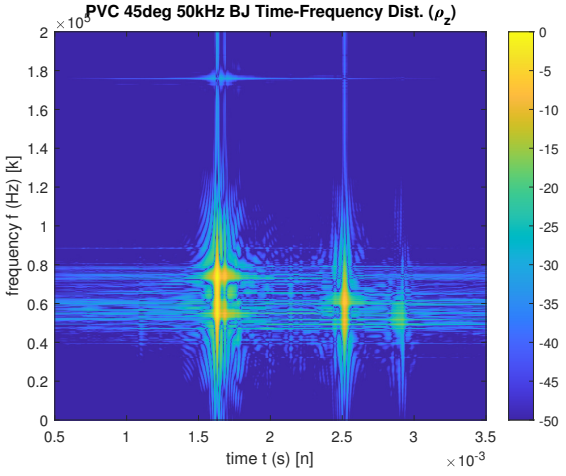


Figure 8.16: Born-Jordan TF dist. (dB), PVC, 45°, 50 kHz center frequency

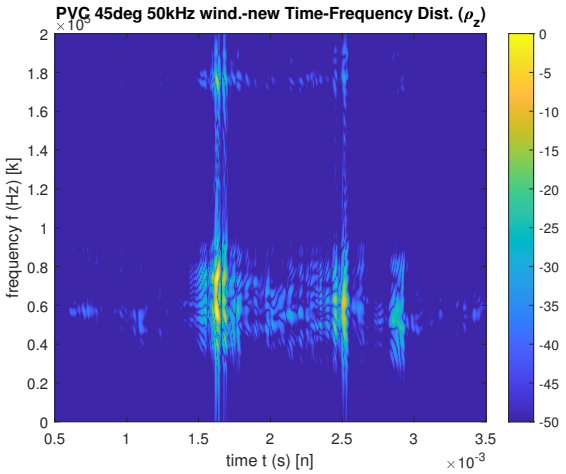


Figure 8.17: Proposed TF dist. (dB), PVC, 45°, 50 kHz center frequency

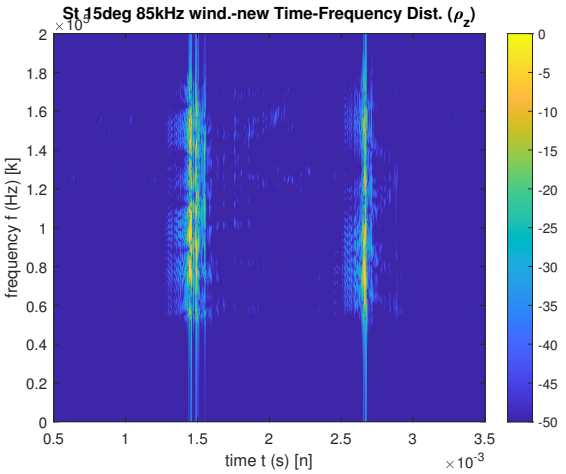


Figure 8.18: Proposed TF dist. (dB), steel, 15°, 85 kHz center frequency

The frequency content which appears in the upper frequencies outside the transmitted signal's bandwidth is related to the use of the deconvolution for pulse compression and to the discrete Hilbert transform used to form the complex analytic signal. The content can be reduced by increasing $\alpha$ such that the operation becomes closer to a matched filter (see Section 2.2), and using a matched filter nearly eliminates it. The remainder is due to the imperfect removal of the mirrored half of a purely real signal's spectrum in the formation of the analytic signal through the Hilbert transform (see Appendix A). Some of the transmitted waveforms are more likely to produce this effect, for instance, the waveform with 85 kHz center frequency. This extra-band content can simply be ignored, however; the advantage of suppressing much of the temporal sidelobe content through the use of the deconvolution is preferable.

Generally speaking, there are significant differences among the acoustic responses of the three materials, some of which are readily observable in the time domain. For incident angles of $\theta \leq 45°$, acoustic responses following the specular are much weaker for the PVC than for the steel or aluminum. Further, aluminum displays a thick wave of apparent EWR response for the intermediate incident angles. See the proposed distribution's representation of the three materials at 15° incidence and with the 85 kHz waveform in Figures 8.18—8.20.

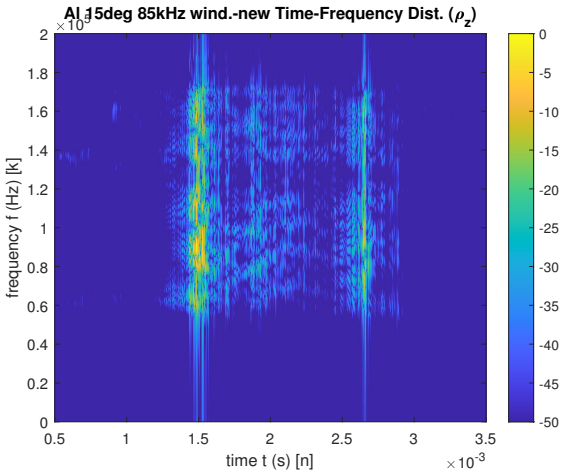


Figure 8.19: Proposed TF dist. (dB), aluminum, 15°, 85 kHz center frequency

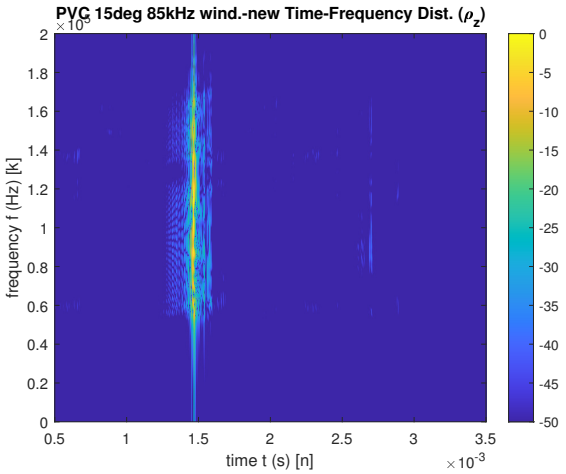


Figure 8.20: Proposed TF dist. (dB), PVC, 15°, 85 kHz center frequency

### 8.3.1 RMS-normalized distribution difference scores

As described in Section 6.2, a quantification of the material differentiation provided by the various TF distributions is sought. Figure 8.21 shows the roll-up of the difference score $D$, averaged across all incident angles and transmitted waveforms for each pairing of the three materials. Interestingly, the spectrogram performs best on this account, and by a considerable margin. The Born-Jordan and Choi-Williams distributions come next, and are nearly identical in this scoring, followed by the Zhao-Atlas-Marks with $a = 1$, the proposed distribution, and the Zhao-Atlas-Marks with $a = 0.35$. Universally across the distributions, aluminum and PVC are the easiest to distinguish, generally trailed by steel versus PVC, and then steel versus aluminum, which are the most difficult to differentiate. Based on the these results, the previous simulations, and initial examinations of the processing results from the collected data, the Zhao-Atlas-Marks with $a = 1$ will be primarily considered. Despite the increased spectral accuracy achieved by the smaller choice for $a$ ($w = 0.03$ is held constant for both choices), the gains do not outweigh the disadvantages of the large and high side-lobes.

A caveat to interpreting these values is that this metric may penalize high-resolution distributions. The calculation is a fairly direct normalized element-wise difference of two materials in a given distribution. If a distribution forms TF components which are

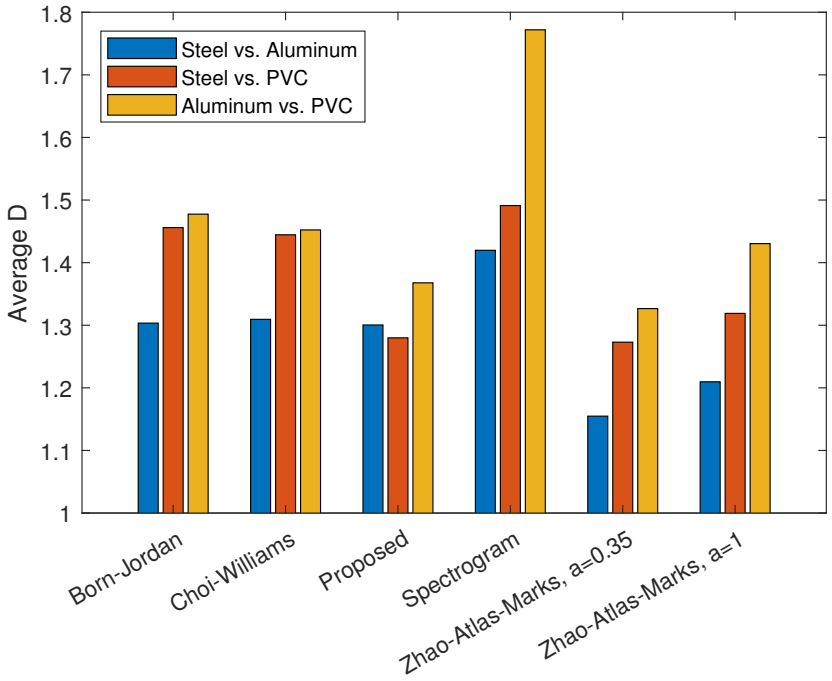


Figure 8.21: RMS-normalized distribution difference scores

large in the TF plane, and a competing distribution forms small components from the same signal, that may result in increased element-wise difference between two materials evaluated in that distribution, in spite of normalization. This is a possible explanation for the good performance of the spectrogram, which is the weakest of the five in terms of resolution. However, the Zhao-Atlas-Marks has a weaker resolution, but does not have particularly good difference scores. At the very least, scores within a given distribution are meaningful, and it is a useful confirmation that PVC is measured as the most outlying material.

### 8.3.2 Identifying the cylinder ends

An initial important reference point for analyzing the time-frequency response of these cylinders is the specular reflection, which, for the end of the cylinder nearest to the hydrophone, is easy to identify as the chronologically first (and loudest) component. Since the endcaps overhang the cylinder ends, however, it introduces an additional specular component returning from the corner created by the furthest endcap (see Figure 8.22).

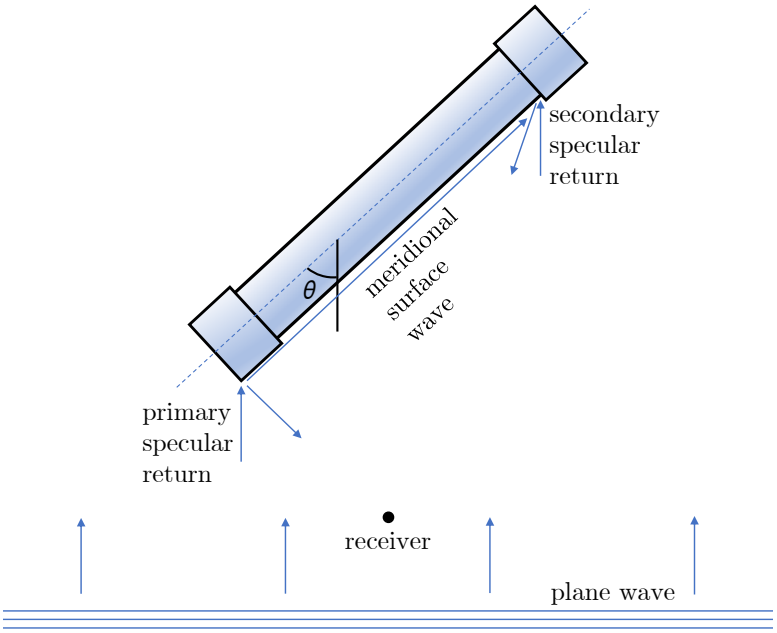


Figure 8.22: Ray geometry of tank data primary acoustic paths

The approximate arrival times of these components can be determined from a geometry calculation to find the difference in acoustic path length. For many of the recorded returns, the pattern of the strong specular component followed by a secondary distinct component (which, as will be discussed, is likely a combination of a specular return from the far endcap and reradiation of a meridional $a_0$ wave) is clearly observed. As the cylinder's supporting apparatus is rotated through increasing incident angles $\theta$ toward broadside, these two components indeed converge in time, and thus range, in proportion to the cosine of the angle $\theta$. This pattern can be observed in Figures 8.23—8.28, which contain the spectrograms of the steel cylinder with the 120 kHz waveform. Notice the return from the further endcap is relatively obscured at end-on incidence, which is expected, and after rotation, it comes into the "view" of the sonar and produces a stronger return. This return meets the initial specular return as the incidence angle reaches 90°.

As similar as the geometries of the cylinders are, it is apparent from the provided photographs that they are not identical. One difference that impacts the analysis of the data in this case is the shape of the endcap. For the aluminum and steel cylinders, they are generally flat, whereas the PVC endcap is more rounded. The impact of this is that,

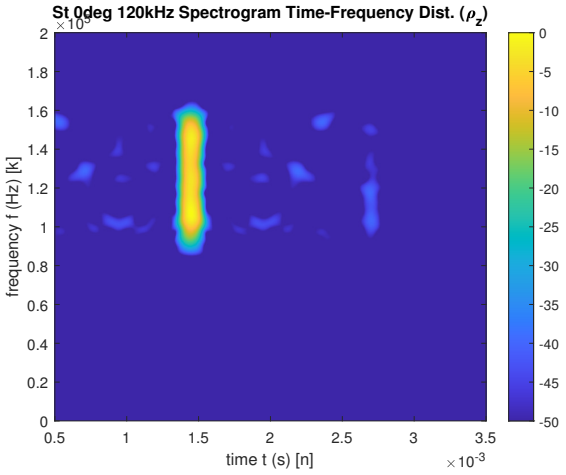


Figure 8.23: Spectrogram (dB), steel, 0°, 120 kHz center frequency

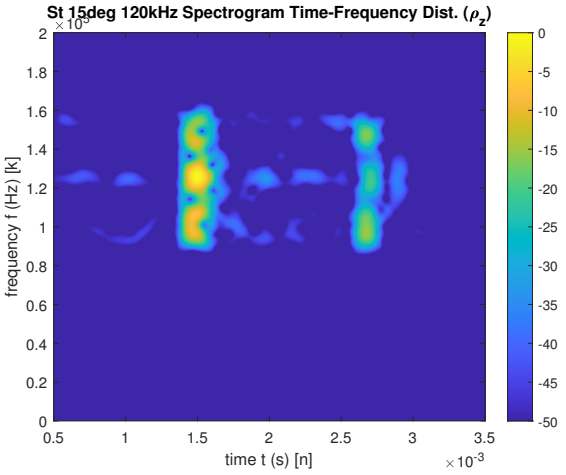


Figure 8.24: Spectrogram (dB), steel, 15°, 120 kHz center frequency

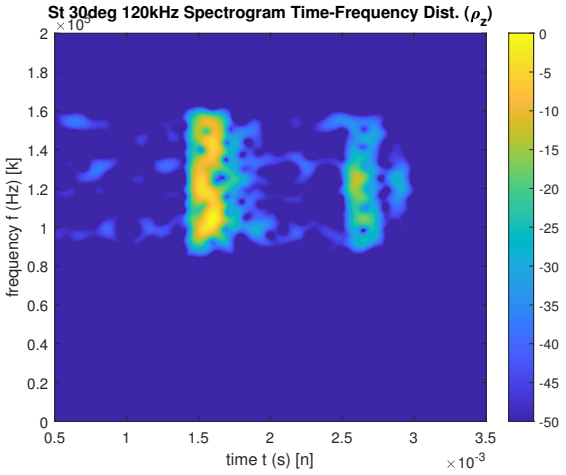


Figure 8.25: Spectrogram (dB), steel, 30°, 120 kHz center frequency

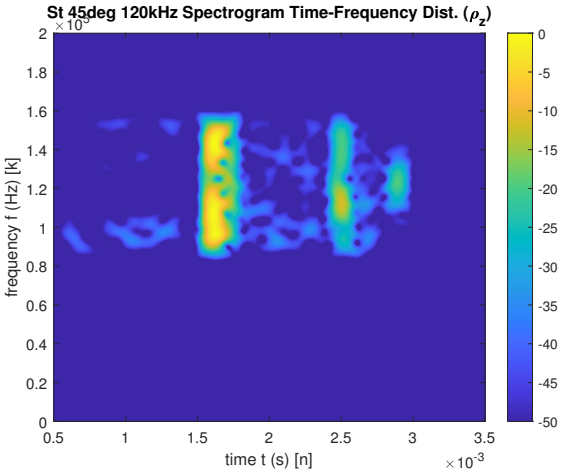


Figure 8.26: Spectrogram (dB), steel, 45°, 120 kHz center frequency

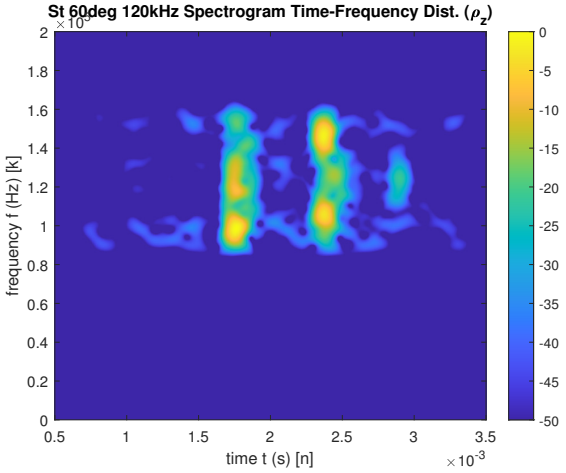


Figure 8.27: Spectrogram (dB), steel, 60°, 120 kHz center frequency

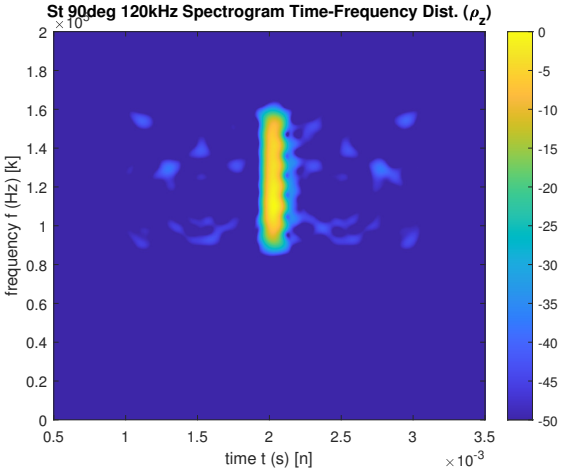


Figure 8.28: Spectrogram (dB), steel, 90°, 120 kHz center frequency

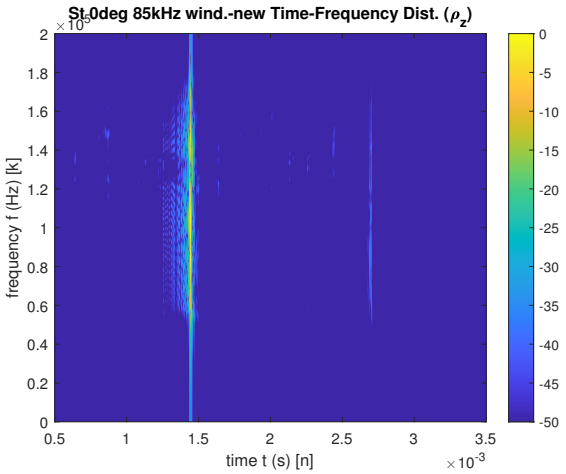


Figure 8.29: Proposed TF dist. (dB), steel, 0°, 85 kHz center frequency

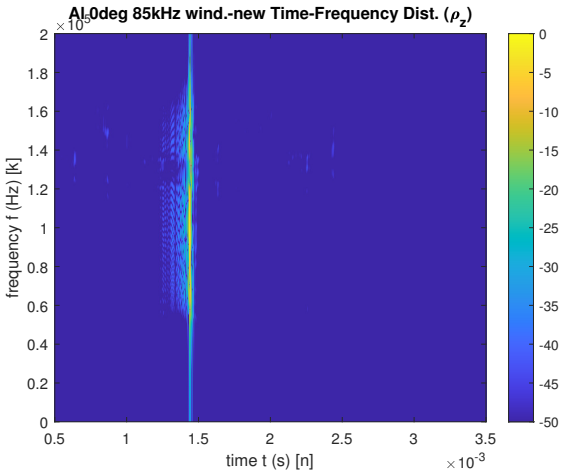


Figure 8.30: Proposed TF dist. (dB), aluminum, 0°, 85 kHz center frequency

in the end-on incidence situation, the specular return of the near end is slightly spread in time, since the incident plane wave is not arriving at the entire surface of the endcap at the same time. Compare the three materials under identical acoustic stimulation by the 85 kHz waveform at $\theta = 0°$ represented by the proposed distribution in Figures 8.29—8.31.

Additionally, these figures show a component visible at the intermediate incident angles at $t \approx 3$ ms which is not as straightforward to attribute. Curiously, it is not dependent upon incident angle for its arrival time, as other EWR components are observed to be [31]. While not clearly visible at $\theta = 0°$ or $\theta = 90°$, it remains quite fixed in time across the other angles. It is also chiefly present only for the steel and PVC cylinders—not for aluminum. Additionally, it does not respond at the full bandwidth of the transmitted waveform, preferring instead to respond primarily in regions around 125 kHz, 50 kHz, and 20 kHz. The fact that its arrival time does not vary with incident angle suggests that this may be an artifact of the support apparatus or the geometry of the cylinder in the tank itself. Nevertheless, it exposes the importance of the spectral accuracy metric developed for the simulation portion of this work. High bandwidth waveforms are known to provide better discrimination and classification information in both sonar and radar, and having a time-frequency distribution which faithfully describes the spectral content across the duration of the return and with high temporal resolution is critical. Figures

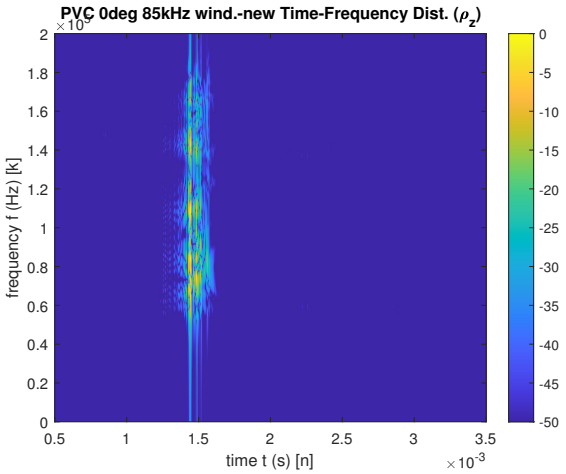


Figure 8.31: Proposed TF dist. (dB), PVC, 0°, 85 kHz center frequency

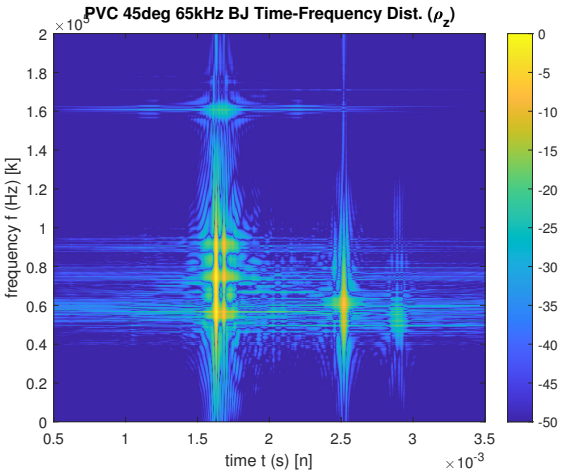


Figure 8.32: Born-Jordan TF dist. (dB), PVC, 45°, 65 kHz center frequency

8.32 and 8.33, reveal this final component's absence in the aluminum cylinder and its lack of wideband support.

### 8.3.3 Broadside incidence

Examination of the broadside incidence ($\theta = 90°$) offers a strong point of concurrence with the acoustic literature. For both the steel and aluminum cylinders there are appearances of the $a_0$ and $a_{0-}$ Lamb waves (see Morse [31]). They are notably absent from the PVC returns—a good sign for potential discrimination. First, consider the $a_0$. It is a wideband peak following closely upon the specular return. Comparing Figures 8.34-8.36, note that this appears with the steel and aluminum cylinders at $t \approx 2.1\,\text{ms}$, but this feature is missing for the PVC. The same is true with the $a_{0-}$. See the narrowband response fading over time out to $t \approx 2.7\,\text{ms}$ in Figures 8.37 and 8.38, importantly in a lower portion of the full, explored bandwidth, which is consistent with Morse's observation. Each repetition is the result of a subsequent circumnavigation of the cylinder. This occurs in a lower portion of the band because of the lengthy traversal of the shell surface—possibly with multiple laps. This results in greater attenuation of the higher frequencies, so they are less likely to make the journey. Again, it is absent from the PVC response in Figure 8.39.

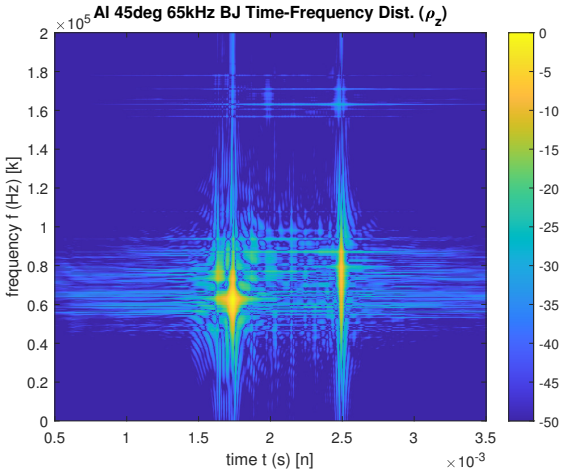


Figure 8.33: Born-Jordan TF dist. (dB), aluminum, 45°, 65 kHz center frequency

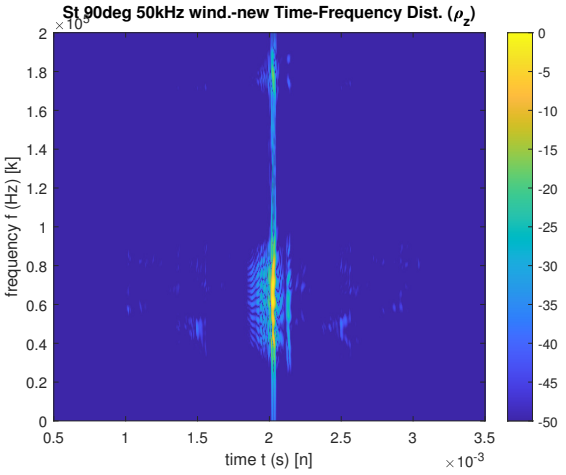


Figure 8.34: Proposed TF dist. (dB), steel, 90°, 50 kHz center frequency

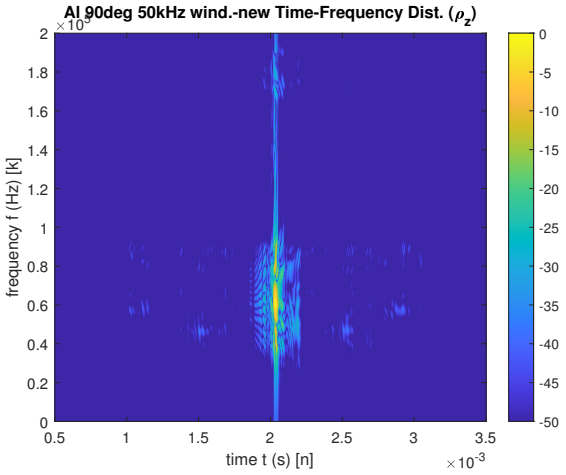


Figure 8.35: Proposed TF dist. (dB), aluminum, 90°, 50 kHz center frequency

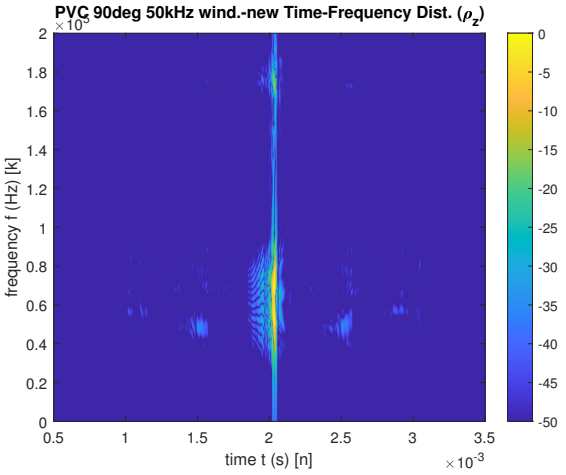


Figure 8.36: Proposed TF dist. (dB), PVC, 90°, 50 kHz center frequency

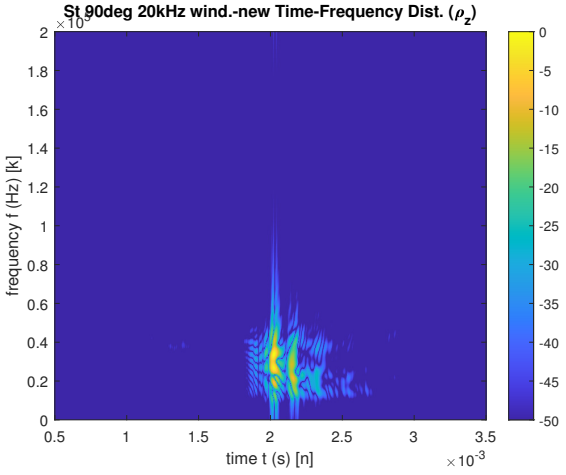


Figure 8.37: Proposed TF dist. (dB), steel, 90°, 20 kHz center frequency

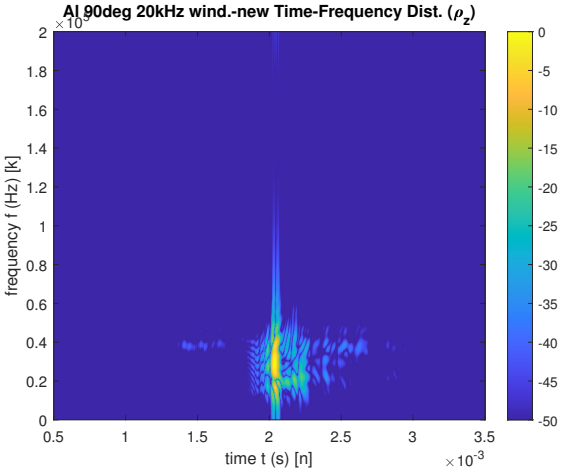


Figure 8.38: Proposed TF dist. (dB), aluminum, 90°, 20 kHz center frequency

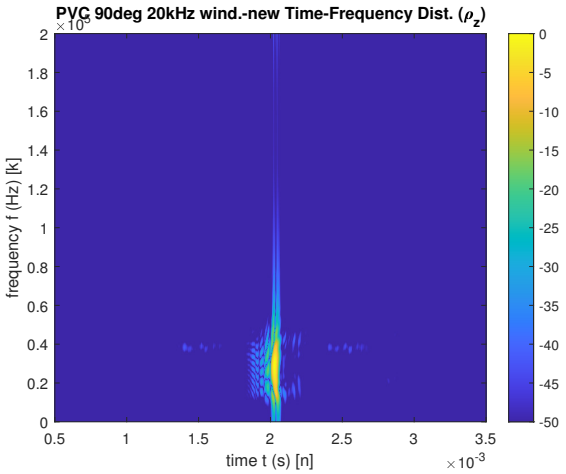


Figure 8.39: Proposed TF dist. (dB), PVC, 90°, 20 kHz center frequency

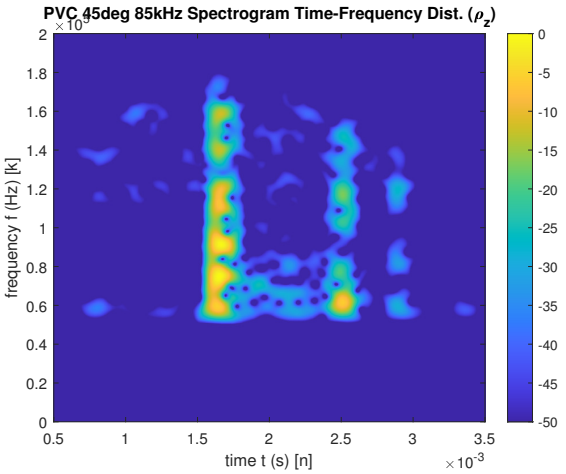


Figure 8.40: Spectrogram (dB), PVC, 45°, 85 kHz center frequency

### 8.3.4 Meridional $a_0$

The literature describes the contribution of the meridional ray, which arrives concurrently with a specular return from the more distant end of a tilted (not end-on or broadside) cylindrical shell [32]. It also predicts that the frequency of this component decreases as the incidence angle approaches end-on. In the case of the current data set, this is potentially a difficult feature to identify, since the endcap creates a strong specular return which is difficult to disentangle. This is why the effect may possibly be observed in the PVC, as its specular far-end returns are weak in comparison to those of the steel and aluminum. Additionally, the meridional effect is traced across a very wide band in the literature, which may well exceed the bandwidth used in the present data collection. Nevertheless, it offers a potential discriminating feature which is identifiable in only one of the three targets. See the shifting component move from $t \approx 2.5\,\text{ms}$ and 100 kHz—120 kHz in Figure 8.40 through 80 kHz—100 kHz in Figure 8.41 to 80 kHz—90 kHz in Figure 8.42.

## 8.4 Time-frequency distributions

### 8.4.1 Spectrogram

The straightforward spectrogram, here, as in many other applications, does not fail to be a decent option. The most noticeable difference from the other distributions under

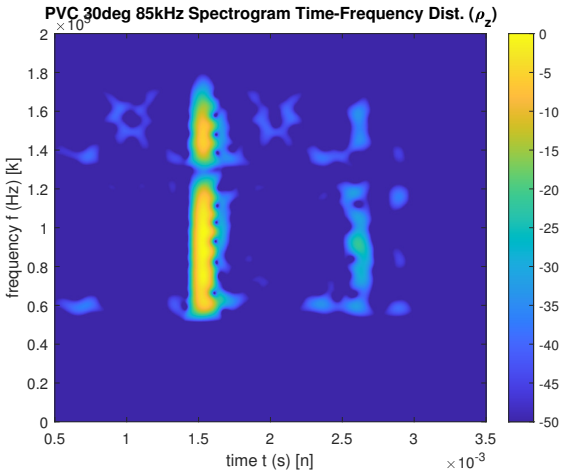


Figure 8.41: Spectrogram (dB), PVC, 30°, 85 kHz center frequency

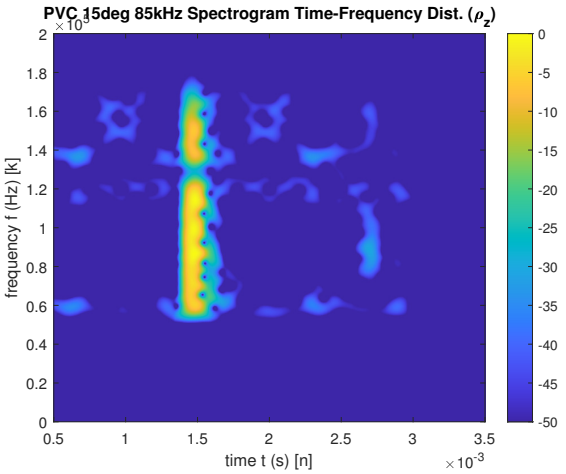


Figure 8.42: Spectrogram (dB), PVC, 15°, 85 kHz center frequency

consideration is the lack of time-frequency resolution in the spectrogram. There are two echo peaks closely spaced in time at $t \approx 1.6$ ms which are visible and resolvable in Figure 8.14. Such a differentiation is much more difficult with the spectrogram in Figure 8.13. This could be counteracted to some extent by reducing the window size, but the simulations demonstrated that there is not much room for reduction without significant costs to the spectral accuracy. Nevertheless, the ability to cut through noise and generate a quantitative difference between the materials is noteworthy.

### 8.4.2 Choi-Williams and Born-Jordan distributions

The Choi-Williams and Born-Jordan distributions will be considered together as they produce highly similar representations of the tank data. This is merely a continuation of the similarities revealed in the simulation experiments in all respects—separation scores, spectral accuracy, multiple EWR handling, and SNR. The primary difference appears to be that the Born-Jordan TF distribution sidelobes are somewhat broader and exhibit more rippling than those of the Choi-Williams. Such differences, however, are really only visible at around 30 dB below the representation peak, and are relatively minor. Even so, this is sufficient to recommend the Born-Jordan over the Choi-Williams, since the latter has no apparent advantage. Compare Figures 8.43 and 8.44, which showcase the differences.

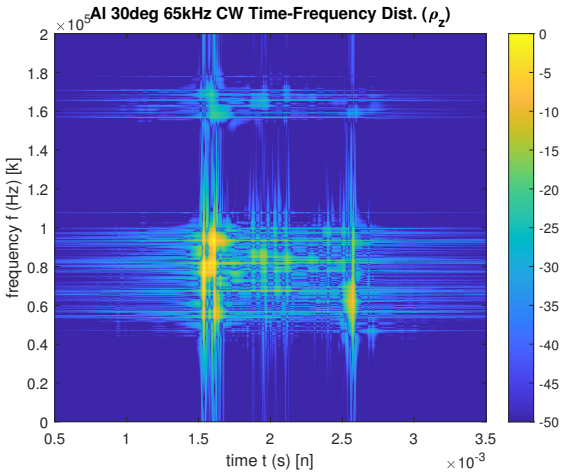


Figure 8.43: Choi-Williams TF dist. (dB), aluminum, 30°, 65 kHz center frequency

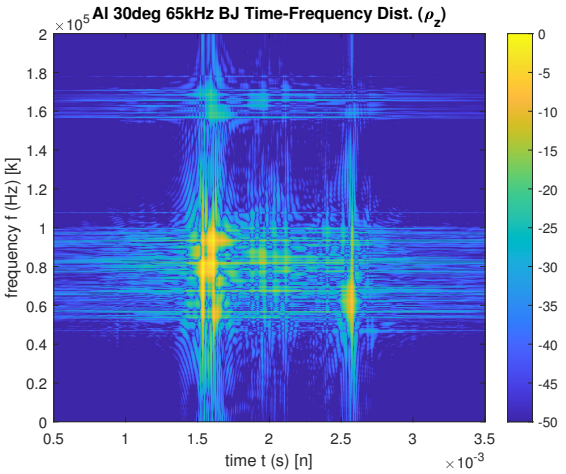


Figure 8.44: Born-Jordan TF dist. (dB), aluminum, 30°, 65 kHz center frequency

### 8.4.3 Zhao-Atlas-Marks distribution

As discussed above, the sidelobe reduction gained by keeping $a$ at 1 rather than 0.35 appears to be important for this EWR application. The resolution is necessary to compete with the other distributions under consideration; the resolution, however, still seems lacking. The fact that the choice of $a = 1$ is likely to reduce spectral accuracy does little to recommend it over the alternatives, even if it does gain some ground on the normalized difference scores. This is perhaps not surprising, as the ZAM is a special case of the Born-Jordan, as discussed earlier. Since analysis of the Born-Jordan did not lead to that special case for EWR, it is unlikely that restraining the Born-Jordan to be the ZAM is going to result in better performance.

### 8.4.4 Windowed proposed distribution

The proposed distribution produces a fine resolution along the time axis and a more delicate sidelobe pattern. There do not seem any major shortfalls in the representations produced out of this data set, but the modest performance with regard to SNR and the normalized difference scores must be noted. An interesting opportunity to observe a previously noted distribution property appears with the 120 kHz waveform and the aluminum cylinder in Figure 8.45. Notice that in the nearly single-component signal, the

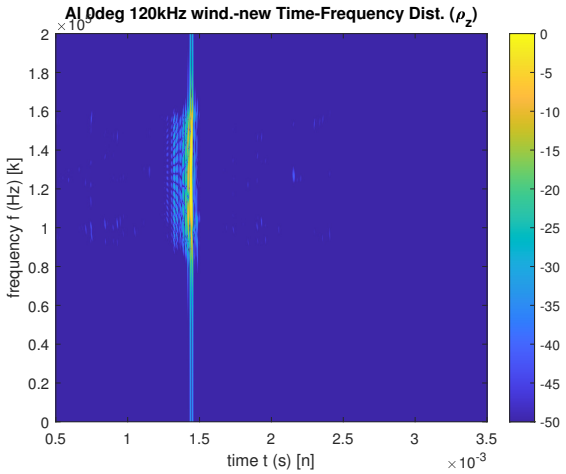


Figure 8.45: Proposed TF dist. (dB), aluminum, 0°, 120 kHz center frequency

cross-term artifacts extend only to the left of the specular return. This helps protect the EWR components from cross-term interference.

## 8.5 Conclusions

The first result is a simple verification of the acoustic literature that the material properties of a sonar target influence the nature of the elastic surface waves excited on it. Two types (three, if the meridional is actually observed here) of waves described in the acoustic literature are observed in the data set under consideration, and they indeed vary across the different object materials, supporting the claim that this type of sonar discrimination is possible. These experiments also demonstrate that a particular TF distribution can perform better than other candidates at making different materials "look" different across a range of frequencies and aspect angles when by design the primary variable is material. Although EWR is a function of both geometry and material, controlling for geometry helps ensure that observed differences are indeed the result of variations in the reradiation of elastic surface waves.

For the processing of this tank data, this investigation supports the choice both of the Born-Jordan and the proposed distributions, and the main driver of the choice between those two is the amount of noise. SNR is the biggest weakness of the proposed distribution, and although it performs well for this data, there is very little noise to speak

of. In a more realistic sonar environment, the Born-Jordan is likely to be preferred. The strength of the proposed distribution is in its reduced sidelobes. Both distributions, however, acceptably represent the time-frequency features of interest in this data set.

A final note is that when using any of these distributions, one must be aware of the inherent artifact patterns. They are different for each distribution and must not be confused with legitimate spectral content. The Choi-Williams and Born-Jordan produce a cross-hatched texture. The spectrogram is pock-marked in a dense time-frequency scene. The proposed distribution tends to produce a series of vertical filaments, and the Zhao-Atlas-Marks has its characteristic lobed structure. For this reason, the examination of the data using a variety of distributions is enlightening; components that are common to all are almost certain to be legitimate.

# Chapter 9

## Innovation and Relevance

Research has been conducted on the acoustics of elastic waves in spherical and cylindrical solids and shells underwater. These efforts suggest that classification advantages may be had in sonar signal processing, and the potential benefits have not been thoroughly explored as yet. Two major modern sonar applications, that of anti-submarine warfare and that of naval mine countermeasures, involve the detection and classification of man-made shells—often in roughly cylindrical and spherical shapes (though with complex internal structures). These shells differ markedly in their abilities to support, and therefore reradiate, elastic waves from naturally-occurring oceanic false alarms like rocks. Interestingly, more than simply discriminating against rocks in favor of man-made shells, this classification method could be used to differentiate metals (provided sufficient difference in elastic moduli). Two shells of the same thickness, one of aluminum and one of stainless steel, may well be differentiable based on elastic wave reradiation. Further, such an ability is not limited to military use. Humanitarian efforts to dispose of unexploded naval ordnance would be enhanced by better sonar discrimination. Thousands of naval mines remain in the Baltic Sea, for instance, from World Wars I and II. There is also need for more effective discovery of wreckage on the sea floor, and acoustic concepts in this dissertation might aid in searching for oil and natural gas beneath the sea floor. In short, knowledge of the oceans is still quite limited, and a sonar sensitive to elastic wave reradiation would make them more transparent.

While there has been some investigation of elastic responses for these sonar applications, what has received little attention, and what is undertaken in this dissertation,

is an examination of the various quadratic time-frequency signal processing methods in light of the physical phenomena to determine the best approaches. The research aim has been to provide theoretical, practical, and quantifiable rationales for the methods preferable in this application, supported by in-water test data. Theoretical justification was also provided to reinforce confidence in the results. Additionally, given the extensive time-frequency investigation necessary to this work, it was appropriate to develop a new time-frequency representation, tailored especially to the sonar elastic response problem, an innovation which may well see use outside its original purpose.

A major novelty is the confluence of information from three significant realms: the study of elastic acoustic phenomena, the time-frequency signal processing theory, and the effort to solve the practical sonar discrimination problem. The references provided in this dissertation deal with one or at most two of these subjects at a time. Considerable further convergence of these lines of work will be necessary to bring maturity and practical efficacy to the technology.

# Chapter 10

## Concluding remarks and future work

There are two primary questions answered by this work:

1. Can objects of differing materials be discriminated using the signal content in sonar returns?

2. Which time-frequency representations best facilitate this discrimination?

A major line of investigation centers on whether EWR-based discrimination can be effectively realized in practical sonar situations. The undersea environment is a notoriously fickle medium for remote sensing, and the signal components required to perform this type of analysis can be subtle. The further complication is the fact that practical subjects of sonar interrogation are not canonical shapes. Generally they are shells, which is promising for the presence of elastic waves, but they sport complex internal structures. Thus, identifying elastic waves of a particular type in what is certain to be a confused web of echoes from a complicated structure will not at all be easy. That notwithstanding, the acoustics literature—both in theory and in controlled experimentation—and the experimental data reviewed above support the claim that such discrimination is possible; numerous overt differences exist among the different materials, even if they are not all easily attributable to a particular acoustic phenomenon. Future data collections should consider other ways of truncating the cylinders which are more uniform across the materials and should target particular EWR components with a bandwidth which helps ensure their observation based on the acoustic theory.

As described above, the TF representation comparison narrows down to the Born-Jordan and the proposed distributions—the former to be preferable under noisy conditions. First, the simulations and acoustic theory provided grounds for ruling out a number of distributions as unsuited to the EWR problem. From there, application of the remaining contenders to in-water EWR sonar data quantitatively and qualitatively supported paring down the number to two. An interesting finding is the aptitude which the proposed distribution (and, for that matter, its family of similar distributions) has for accurately representing the spectrum of a short, pulse-type waveform. These two quadratic TF distributions (at least) perform well at the types of tasks necessary to the discrimination of sonar targets based on EWR.

This is quite early in the technology development process. Specific and reliable discrimination features will need to be identified before an algorithmic approach can be properly applied. This will necessitate further controlled experimentation and, if possible, experimentation at the scale (in both sonar range and frequency) of the EWR application in view. Computational complexity will become relevant. None of these is trivial, but the groundwork laid here underpins further inquiry.

*S. D. G.*

References

[1] S. D. Anderson, K. G. Sabra, M. E. Zakharia, and J. Sessarego, "Time-frequency analysis of the bistatic acoustic scattering from a spherical elastic shell," *J. Acoust. Soc. Amer.*, vol. 131, pp. 164-173, 2012.

[2] F. Auger, O. Lemoine, P. Gonçalvès, and P. Flandrin, *The Time-Frequency Toolbox*, Jan. 1996. Accessed on: Jan. 2, 2020. [Online]. Available: http://tftb.nongnu.org/

[3] B. Barkat and B. Boashash, "A high-resolution quadratic time-frequency distribution for multicomponent signals analysis," *IEEE Trans. Signal Process.*, vol. 49, no. 10, pp. 2232-2239, Oct. 2001.

[4] F. J. Blonigen and P. L. Marston, "Leaky helical flexural wave backscattering contributions from tilted cylindrical shells in water: Observations and modeling," *J. Acoust. Soc. Amer.*, vol. 112, pp. 528-536, 2002.

[5] F. J. Blonigen and P. L. Marston, "Leaky helical flexural wave scattering contributions from tilted cylindrical shells: Ray theory and wave-vector anisotropy," *J. Acoust. Soc. Amer.*, vol. 110, pp. 1764-1769, 2001.

[6] B. Boashash, Ed., *Time Frequency Signal Analysis and Processing: A Comprehensive Review*. San Diego: Elsevier, 2005.

[7] B. Boashash and S. Ouelha, "An improved design of high-resolution quadratic time-frequency distributions for the analysis of nonstationary multicomponent signals using directional compact kernels," *IEEE Trans. Signal Process.*, vol. 65 no. 10, pp. 2701-2713, May 2017.

[8] M. Born and P. Jordan, "Zur Quartenmechanik," *Zeitschrift für Physik*, vol. 34, pp. 858-888, 1925.

[9] M. Bruneau, *Fundamentals of Acoustics*. London: ISTE, 2006.

[10] H.-I. Choi and W. J. Williams, "Improved time-frequency representation of multi-component signals using exponential kernels," *IEEE Trans. Acoustics, Speech, and Signal Process.*, vol. 37, no. 6, pp. 862-871, Jun. 1989.

[11] L. Cohen, "Time-frequency distributions—A review," *Proc. IEEE*, vol. 77, no. 7, pp. 941-981, Jul. 1989.

[12] J. M. Conoir, P. Rembert, O. Lenoir, and J. L. Izbicki, "Relation between surface helical waves and elastic cylinder resonances," *J. Acoust. Soc. Amer.*, vol. 93, pp. 1300-1307, 1993.

[13] A. L. España, K. L. Williams, D. S. Plotnick, and P. L. Marston, "Acoustic scattering from a water-filled cylindrical shell: Measurements, modeling, and interpretation," *J. Acoust. Soc. Amer.*, vol. 136, pp. 109-121, 2014.

[14] D. Gabor, "Theory of communication," *J. Inst. Elec. Engs.*, vol. 93(III), pp. 429-457, Nov. 1946.

[15] K. Gipson and P. L. Marston, "Backscattering enhancements due to reflection of meridional leaky Rayleigh waves at the blunt truncation of a tilted solid cylinder in water: Observations and theory," *J. Acoust. Soc. Amer.*, vol. 106, pp. 1673-1680, 1999.

[16] R. C. Gonzalez and R. E. Woods, *Digital Image Processing*. Upper Saddle River, NJ: Pearson Education, Inc., 2008.

[17] A. M. Gunderson, A. L. España, and P. L. Marston, "Spectral analysis of bistatic scattering from underwater elastic cylinders and spheres," *J. Acoust. Soc. Amer.*, vol. 142, pp. 110-115, 2017.

[18] L. Haumesser, A. Baillard, D. Décultot, and G. Maze, "Behavior of the first guided wave on finite cylindrical shells of various lengths: Experimental investigation," *J. Acoust. Soc. Amer.*, vol. 109, pp. 583-590, 2001.

[19] J. M. Ho, "Monostatic and bistatic ray acoustic scattering by submerged elastic spherical shells," *J. Acoust. Soc. Amer.*, vol. 95, pp. 1264-1273, 1994.

[20] Z. M. Hussain and B. Boashash, "Adaptive instantaneous frequency estimation of multi-component FM signals," *Proc. IEEE Internat. Conf. Acoustics, Speech, and Signal Process.*, pp. 657-660, Istanbul, Jun. 2000.

[21] G. Kaduchak and P. L. Marston, "Backscattering of chirped bursts by a thin spherical shell near the coincidence frequency," *J. Acoust. Soc. Amer.*, vol. 93, pp. 2700-2706, 1993.

[22] G. Kaduchak and P. L. Marston, "Observation of the midfrequency enhancement of tone bursts backscattered by a thin spherical shell in water near the coincidence frequency," *J. Acoust. Soc. Amer.*, vol. 93, pp. 224-230, 1993.

[23] F. Léon, F. Lecroq, D. Décultot, and G. Maze, "Scattering of an obliquely incident acoustic wave by an infinite hollow cylindrical shell," *J. Acoust. Soc. Amer.*, vol. 91, pp. 1388-1397, 1992.

[24] M. J. Levin, "Instantaneous spectra and ambiguity functions," *IEEE Trans. Information Theory*, vol. 10, no. 1, pp. 95-97, Jan. 1964.

[25] W. Li, G. R. Liu, and V. K. Varadan, "Estimation of the radius and thickness of a thin spherical shell in water using the midfrequency enhancement of a short tone burst response," *J. Acoust. Soc. Amer.*, vol. 118, pp. 2147-2153, 2005.

[26] P. L. Marston, "Approximate meridional leaky ray amplitudes for tilted cylinders: End-backscattering enhancements and comparisons with exact theory for infinite solid cylinders," *J. Acoust. Soc. Amer.*, vol. 102, pp. 358-369, 1997.

[27] P. L. Marston and S. F. Morse, "Time-frequency analysis of transient high-frequency dispersive guided waves on tilted cylindrical shells: Review," *Proc. Mtgs. Acoust.*, vol. 19, 055073, 2013.

[28] P. L. Marston and N. H. Sun, "Backscattering near the coincidence frequency of a thin cylindrical shell: Surface wave properties from elasticity theory and an approximate ray synthesis," *J. Acoust. Soc. Amer.*, vol. 97, pp. 777-783, 1995.

[29] P. L. Marston and N. H. Sun, "Resonance and interference scattering near the coincidence frequency of a thin spherical shell: An approximate ray synthesis," *J. Acoust. Soc. Amer.*, vol. 92, pp. 3315-3319, 1993.

[30] O. Moreno, R. A. Games, and H. Taylor, "Sonar Sequences from Costas arrays and the best known sonar sequences with up to 100 symbols," *IEEE Trans. Information Theory*, vol. 39, no. 6, pp. 1985-1987, Nov. 1985.

[31] S. F. Morse and P. L. Marston, "Backscattering of transients by tilted truncated cylindrical shells: Time-frequency identification of ray contributions from measurements," *J. Acoust. Soc. Amer.*, vol. 111, pp. 1289-1294, 2002.

[32] S. F. Morse and P. L. Marston, "Meridional ray contributions to scattering by tilted cylindrical shells above the coincidence frequency: Ray theory and computations," *J. Acoust. Soc. Amer.*, vol. 106, pp. 2595-2600, 1999.

[33] S. F. Morse, P. L. Marston, and G. Kaduchak, "High-frequency backscattering enhancements by thick finite cylindrical shells in water at oblique incidence: Experiments, interpretation, and calculations," *J. Acoust. Soc. Amer.*, vol. 103, pp. 785-794, 1998.

[34] C. H. Page, "Instantaneous power spectra," *J. Applied Physics*, vol. 23, no. 1, pp. 103-106, Jan. 1952.

[35] S. Pei and J. Ding, "Relations between Gabor transforms and fractional Fourier transforms and their applications for signal processing," *IEEE Trans. Signal Process.*, vol. 55, no. 10, pp. 4839-4850, Oct. 2007.

[36] A. W. Rihaczek, "Signal energy distribution in time and frequency," *IEEE Trans. Information Theory*, vol. 14, no. 3, pp. 369-374, May 1968.

[37] G. S. Sammelmann, D. H. Trivett, and R. H. Hackman, "The acoustic scattering by a submerged, spherical shell. I: The bifurcation of the dispersion curve for the spherical antisymmetric Lamb wave," *J. Acoust. Soc. Amer.*, vol. 85, pp. 114-124, 1989.

[38] Z. Seddighi, M. R. Ahmadzadeh, and M. R. Taban, "Quantitative analysis of SNR in bilinear time frequency domain," *Signal, Image and Video Process.*, vol. 14, pp. 1583-1590, May 2020.

[39] M. Talmant, H. Überall, R. D. Miller, M. F. Werby, and J. W. Dickey, "Lamb waves and fluid-borne waves on water-loaded, air-filled thin spherical shells," *J. Acoust. Soc. Amer.*, vol. 86, pp. 278-289, 1989.

[40] N. Touraine, L. Haumesser, D. Décultot, G. Maze, A. Klauson, and J. Metsaveer, "Analysis of the acoustic scattering at variable incidences from an extra thin cylindrical shell bounded by hemispherical endcaps," *J. Acoust. Soc. Amer.*, vol. 108, pp. 2187-2196, 2000.

[41] E. Wigner, "On the quantum correction for thermodynamic equilibrium," *Phys. Rev.*, vol. 40, pp. 749-759, Jun. 1932.

[42] J. Ville, "Théorie et applications de la notion de signal analytique," *Cables et Transmissions* (in French), vol. 2A, no. 1, pp. 61-74, 1948 (Transl.: I. Selin, "Theory and application of the notion of complex signal," Rand Corp. Rep. T-92, Santa Monica, CA, USA, Aug. 1958).

[43] L. G. Zhang, N. H. Sun, and P. L. Marston, "Midfrequency enhancement of the backscattering of tone bursts by thin spherical shells," *J. Acoust. Soc. Amer.*, vol. 91, pp. 1862-1874, 1992.

[44] Y. Zhao, L. E. Atlas, and R. J. Marks, "The use of cone-shaped kernels for generalized time-frequency representations of nonstationary signals," *IEEE Trans. Acoustics, Speech, and Signal Process.*, vol. 38, no. 7, pp. 1084-1091, Jul. 1990.

Appendices

# Appendix A

## The discrete Hilbert transform

Oftentimes in waveform design a complex signal $z(t)$ is produced which is known as the analytic signal [6]. The Hilbert transform,

$$\mathcal{H}\{s(t)\} = s(t) * \frac{1}{\pi t}, \tag{A.1}$$

relates the real and imaginary parts of this signal, such that

$$z(t) = s(t) + j\mathcal{H}\{s(t)\}. \tag{A.2}$$

A purely real version of the signal may be required, however, if it is to be physically generated. This is most naturally done by using the real portion of the complex signal and dispensing with the imaginary. In modern practice, such a signal is almost certain to be discrete, so care must taken in leaving aside the imaginary part. The imaginary is said to be in quadrature to the real, or at a $\pi/2$ phase offset for each sample. Naturally this provides pertinent frequency information in signal analysis, as the frequency spectra of complex signals are "one-sided" and of real signals, symmetrical. Regarding only the real part of such a complex signal increases the frequency ambiguity and results in aliasing if the sampling rate is sufficiently low.

# Appendix B

## On the product of waveform bandwidth and pulse duration

A brief demonstration of the idea that the product of waveform bandwidth $f_{\mathrm{BW}}$ and pulse duration $T$, rather than either independently, determines the width of the main lobe in matched filter output.

First, consider a linear frequency-modulated transmit waveform given by

$$x(t) = p_T(t)\left[e^{j\pi\frac{f_{\mathrm{BW}}}{T}t^2 + j2\pi f_s t}\right], \tag{B.1}$$

where $f_s$ is the starting frequency and $p_T(t)$ is the rectangular pulse function, equal to 1 for $-\frac{T}{2} \leq t \leq \frac{T}{2}$ and 0 elsewhere. To determine what influences the main lobe width in the matched filter, solve

$$\mathrm{MF}_x[x(t)] = x(t) * \overline{x(-t)}. \tag{B.2}$$

Instead of the typical convolution formulation

$$y(t) = \int_{-\infty}^{\infty} f(\tau)\, g(t-\tau)\, d\tau, \tag{B.3}$$

consider

$$\begin{aligned} y(t) &= \int_{-\infty}^{\infty} f(\tau)\, g(-(-t+\tau))\, d\tau & \text{(B.4)}\\ &= \int_{-\infty}^{\infty} f\left(\frac{t}{2}+\tau\right) g\left(-\left(-\frac{t}{2}+\tau\right)\right) d\tau & \text{(B.5)}\\ &= \int_{-\infty}^{\infty} f\left(\frac{t}{2}+\tau\right) g\left(\frac{t}{2}-\tau\right) d\tau, & \text{(B.6)} \end{aligned}$$

where the $t$ offset is distributed between the functions to help with the derivation. So,

$$\mathrm{MF}_x\left[x\left(t\right)\right] = \int_{-\infty}^{\infty} x\left(\frac{t}{2}+\tau\right)\overline{x\left(-\frac{t}{2}+\tau\right)}d\tau, \tag{B.7}$$

$$= e^{j2\pi f_s t}\int_{-\infty}^{\infty} p_T\left(\frac{t}{2}+\tau\right)p_T\left(-\frac{t}{2}+\tau\right)e^{j2\pi\frac{f_{\mathrm{BW}}}{T}t\tau}d\tau \tag{B.8}$$

through substitution and simplification. The pulse functions can be used to simplify the limits of integration, giving

$$\mathrm{MF}_x\left[x\left(t\right)\right] = \begin{cases} e^{j2\pi f_s t}\int_{\frac{|t|}{2}-\frac{T}{2}}^{-\frac{|t|}{2}+\frac{T}{2}} e^{j2\pi\frac{f_{\mathrm{BW}}}{T}t\tau}d\tau, & -T \le t \le T \\ 0, & \text{otherwise} \end{cases}. \tag{B.9}$$

After integration and the use of Euler's formula and trigonometric identities, the nonzero case becomes

$$\mathrm{MF}_x\left[x\left(t\right)\right] = e^{j2\pi f_s t}\frac{\sin\left(\pi\frac{f_{\mathrm{BW}}}{T}t\left(T-|t|\right)\right)}{\left(\pi\frac{f_{\mathrm{BW}}}{T}t\right)}, \quad -T \le t \le T. \tag{B.10}$$

The two zeros of this function closest to $t = 0$ will give the width of the main lobe. For that purpose, the sine term is relevant since the complex exponential has always a magnitude of one. The sine is zero when its argument is zero, but that, of course, is the peak of the main lobe due to $t$ in the denominator. Moving outward, the next zeros occur when the sine argument is $\pm\pi$. Now a general solution is desired, which is not dependent on $T$, so $\frac{t}{T}$ will be solved for instead, to demonstrate that the matched filter main lobe will have the same width relative to $T$ as long as the time-bandwidth product is constant. So assume $f_{\mathrm{BW}}T = c$, where $c$ is a constant. Now this admits that the main lobe width will change in absolute terms for a constant time-bandwidth product, but generally a sonar system's sampling rate will depend directly upon the transmit waveform bandwidth. So also assume a sampling rate $\sigma$ is determined by the bandwidth and a percentage factor $p_\sigma$,

$$\sigma = p_\sigma f_{\mathrm{BW}}. \tag{B.11}$$

So how many samples $N$ will occur in the period of $2T$ over which the matched filter is defined?

$$N = 2T\sigma = 2Tp_\sigma f_{\mathrm{BW}} = 2p_\sigma c, \tag{B.12}$$

so while the absolute duration of time spanning the width of the main lobe will change with varying time-bandwidth product, the number of samples spanning that main lobe will not, given the above assumptions.

Returning to the primary line of reasoning, it remains to be shown that the main lobe width will in fact remain constant for $\frac{t}{T}$. The argument then of the sine in Equation B.10 is $\pm\pi$ when

$$f_{\mathrm{BW}}\frac{t}{T}\left(T - |t|\right) = \pm 1. \tag{B.13}$$

This yields a set of four equations summarized by

$$f_{\mathrm{BW}}\frac{t}{T}\left(T \pm t\right) = \pm 1, \tag{B.14}$$

which are valid for different $t$, but the form of the equations is what is important here. Assuming the constant time-bandwidth product, this can become

$$\pm c\left(\frac{t}{T}\right)^2 - c\left(\frac{t}{T}\right) \pm 1 = 0. \tag{B.15}$$

Solving for $\frac{t}{T}$ with the quadratic formula, it is seen that the solutions depend only on the time-bandwidth product, and variation in the absolute time duration of the main lobe is accounted for by variation in the sampling rate, resulting in the matched filter output looking effectively the same when the time-bandwidth product is kept constant.